Deep Learning–Based Data-Driven Analysis of Complex Plasmas in a Direct Current Discharge

Niklas Joseph Dormagen

Gießen 2026

Deep Learning–Based Data-Driven Analysis of Complex Plasmas in a Direct Current Discharge

Niklas Joseph Dormagen

A cumulative thesis submitted in fulfillment of the requirements for the degree of Dr. rer. nat.

Research conducted at
I. Institute of Physics, Justus–Liebig–University, Gießen
and
NanoP, Technische Hochschule Mittelhessen, Gießen

Gießen, 05.03.2026

Deep Learning–Based Data-Driven Analysis of Complex Plasmas in a Direct Current Discharge

Kumulative Dissertation von Niklas Dormagen, M.Sc.
Fachbereich 07: Mathematik und Informatik, Physik, Geographie

Justus-Liebig-Universität
I. Physikalisches Institut
Heinrich-Buff-Ring 16
35392 Gießen

Erstgutachter: Dr. Markus Thoma
Zweitgutachter: Dr. Mike Schwarz

Contents

List of Figures

List of Tables

Abbreviations

AIPEX ..... Artificial Intelligence for Plasma Experiments

PK-4 ..... Plasmakristall-4

ISS ..... International Space Station

fcc ..... face centered cubic

bcc ..... body centerred cubic

hcp ..... hexagonal closed packed

fco ..... face centered orthorhombic

bco ..... body centered orthorhombic

bct ..... body centered tetragonal

BOOP ..... bond orientational order parameters

CNA ..... common-neighborhood analysis

EM ..... Engineering Model

SRM ..... Science Reference Model

DC ..... direct current

RF ..... radio-frequency

DLR ..... German Aerospace Center

CCD ..... charge-coupled device

CMOS ..... complementary metal-oxide-semiconductor

ECC ..... Error Correction Code

RAM ..... Random Access Memory

CAN ..... Controller Area Network

ML ..... machine learning

ReLU ..... rectified linear unit

MSE ..... mean squared error

MLP ..... multilayer perceptron

CNN ..... Convolutional Neural Network

SOM ..... self-organizing map

MCS ..... Mixed Crystal Signature

MSM ..... Minkowski structure metric

SE(3) ..... special Euclidean group

CEGANN ..... Crystal Edge Graph Attention Neural Network

LLM ..... large language model

Physical Constants

Name	Symbol	Value	Unit
Boltzmann constant	k_B	1.380649×10^{-23}	$J\,K^{-1}$
elementary charge	e	$1.602\,176\,634 \times 10^{-19}$	C
vacuum electric permittivity	ε_0	$8.854\,187\,8188 \times 10^{-12}$	$F\,(m)^{-1}$
electron mass	m_e	$9.1093837139 \times 10^{-31}$	kg
Pi	π	$3.141\,592\,653\,589\,793$	—

Physical constants [1].

Abstract

Complex plasmas, which are composed of electrons, ions, neutral gas atoms and micrometer sized particles, provide a unique platform for studying fundamental physical phenomena. Because the interparticle distances are comparatively large, it is possible to resolve individual particles optically. This makes it possible to investigate processes such as crystallisation, phase transitions and collective excitations. One of the experimental platforms for studying complex plasmas is the Plasma Crystal Experiment 4 (PK-4), which operates under direct current (DC) conditions. It is used on Earth and in microgravity environments, like on the International Space Station (ISS) and during parabolic flights. To reach the full potential of complex plasmas, however, robust methods must be developed to detect, track, and classify microscopic particles. Traditional image processing techniques often reach their limits in this context, especially for large datasets or under experimentally induced image noise. Therefore, modern machine learning approaches and deep neural networks offer a promising way to optimize and automate the analysis of complex plasmas, where possible.

This dissertation presents a comprehensive framework for using deep learning methods to analyze complex plasmas in the PK-4 experiment. The work is organized into three main contributions. First, a compact U-Net architecture is developed for efficient and accurate particle detection and tracking in dense plasmas. Second, WignerNet, a PointNet based model, is introduced to enable the local classification of crystalline domains using three-dimensional, Voronoi-based representations. Third, an extended graph neural network approach is used to identify more complex structures. Combining these methods greatly improves the diagnosis of complex plasmas by enabling scalable analysis at the single-particle level. In this way, the dissertation contributes both methodologically and experimentally to a deeper understanding of the dynamics and self-organization of complex plasma systems.

Zusammenfassung

Komplexe Plasmen, bestehend aus Elektronen, Ionen, neutralen Gasatomen und mikrometergroßen Partikeln, bieten eine einzigartige Plattform zur Untersuchung grundlegender physikalischer Phänomene. Aufgrund der großen Teilchenabstände ist eine direkte optische Analyse einzelner Partikel möglich und damit die Untersuchung von Prozessen wie Kristallisation, Phasenübergängen und kollektive Anregungen. Eine der experimentellen Plattformen für Untersuchungen komplexer Plasmen ist das Plasmakristall-Experiment 4 (PK-4), das unter Gleichstrombedingungen (DC) betrieben wird und sowohl auf der Erde als auch in Mikrogravitation, etwa auf der Internationalen Raumstation ISS oder bei Parabelflügen, eingesetzt wird. Um das diagnostische Potenzial komplexer Plasmen voll ausschöpfen zu können, ist die Entwicklung robuster Methoden zur Erkennung, Verfolgung und Klassifikation mikroskopischer Partikel unerlässlich. Herkömmliche bildverarbeitende Verfahren stoßen hierbei oft an ihre Grenzen, insbesondere bei großen Datenmengen oder unter experimentell bedingtem Bildrauschen. Daher bieten moderne Verfahren des maschinellen Lernens und tiefe neuronale Netze einen vielversprechenden Ansatz, um die Analyse komplexer Plasmen zu optimieren und gegebenenfalls zu automatisieren.
Diese Arbeit stellt ein umfassendes Konzept zur Anwendung von Deep-Learning-Methoden auf die Analyse komplexer Plasmen im PK-4-Experiment vor. Die Arbeit gliedert sich in drei zentrale Beiträge. Erstens wird eine kompakte U-Net-Architektur zur effizienten und präzisen Partikellokalisierung in dichten Plasmen entwickelt. Zweitens wird mit WignerNet ein auf PointNet basierendes Modell vorgestellt, das auf Basis dreidimensionaler Voronoi-Darstellungen die lokale Klassifikation kristalliner Domänen erlaubt. Drittens wird ein weiterentwickelter Graph-Neural-Network-Ansatz eingesetzt, um komplexere Strukturen identifizieren zu können. Die Kombination dieser neuartigen Methoden stellt einen wesentlichen Fortschritt in der Diagnostik komplexer Plasmen dar und ermöglicht eine skalierbare Analyse auf Einzelteilchenebene. Damit leistet diese Arbeit sowohl methodisch als auch experimentell einen Beitrag zur tieferen Erforschung der Dynamik und Selbstorganisation komplexer Plasmasysteme.

Chapter 1

Introduction

By varying pressure and temperature as thermodynamic state variables, the familiar phases solid, liquid, and gas can be transformed into each other [2]. However, with a constant supply of energy, gases transition to a new state, known as the plasma state, once the average particle energy exceeds the ionization threshold. In this regime, the gas is energized to the degree that electrons are detached from their atomic shells, causing neutral atoms to become ionized.
A plasma is therefore a partially or fully ionized gas composed of freely moving electrons, ions, and neutral atoms. The degree of ionization x of a plasma is defined as follows:

$$x = \frac{n_i}{n_i + n_a} \tag{1.1}$$

where n_i denotes the ion density and n_a the density of neutral atoms. If $x \approx 1$, the plasma is referred to as a fully ionized or hot plasma, as seen, for example, in fusion experiments. However, for $x \ll 1$ the plasma is weakly ionized and is referred to as low-temperature plasma.
Approximately 99 % of the visible matter in the universe is in a plasma state, most notably in stars, which are enormous spheres of hot plasma [3]. Plasmas also appear in everyday life. For instance, fluorescent lamps contain low-temperature plasmas that are maintained by electric fields. These plasmas emit light due to excited gas atoms and ongoing recombination processes.
The systems investigated in this work belong to the class of low-temperature plasmas into which monodisperse, micrometer-sized particles are injected. Low-temperature plasmas are typically generated and stabilized in the laboratory by external electric fields. In this environment, electrons are accelerated until their kinetic energy exceeds the ionization energy of neutral particles. Through inelastic electron-neutral collisions, an avalanche-like ionization cascade is initiated. This cascade saturates once the production rate of charge carriers is balanced by the corresponding loss processes [2].

Because low-temperature plasmas are weakly ionized, their interactions with neutral atoms and the surface of the surrounding vessel are important. Collisions between ions and neutral atoms ensure that the thermal energy of the ions is in equilibrium with that of the neutral gas. For this reason, low-temperature plasmas typically exist at or near room temperature. However, losses at the plasma boundary are significant. Due to their higher mobility, electrons accumulate on the surface of the vessel and charge it negatively. Therefore, plasma can only be sustained through continuous ionization, which requires an external electric field to provide continuous energy input. Once the external energy input stops, electrons recombine with ions, and the plasma decays. Low-temperature plasmas are not in thermal equilibrium, as the electron temperature T_e is usually about 100 times higher than the ion temperature T_i. Most gases have ionization energies on the order of several electron volts, so a high electron temperature is necessary for ionization to occur.

Through their continuous interaction with the background plasma, the injected particles effectively constitute an additional plasma component [4]. This state is referred to as a complex or dusty plasma [5, 6, 7]. The particles charge negatively because of the more mobile electrons and because of their comparatively large mass and low kinetic temperature, form correlated structures. Initially, interest in dusty plasmas developed in the field of astrophysics. Natural dust is widespread throughout the universe. Substantial amounts of dust are found in interplanetary and interstellar clouds, as well as in comet tails [8, 9]. The complex morphology of planetary ring systems [10] and the particle transport processes observed within these rings [11] are important topics in the study of dusty plasmas. Dust also plays a significant role in magnetospheric and ionospheric physics.

Complex plasmas exhibit a wide range of fundamental dynamical processes, including crystal growth [12], melting and recrystallization [13, 14], local rearrangements [15, 16], turbulence [17], and acoustic wave phenomena [18, 19]. Variations in external parameters such as pressure, electric field strength, discharge type, or ion flow lead to transitions between disordered and ordered phases. Since the particles are observable in the optical range, collective processes and structural rearrangements can be tracked directly at the single-particle level. This makes complex plasmas a highly attractive model system for many-body physics [20].

To investigate these phenomena in greater detail, a variety of experimental setups have been developed over the past few decades to enable the study of complex plasmas under laboratory and microgravity conditions. The experiments for this dissertation were conducted using the Plasmakristall 4 experiment [21] (PK-4). This experiment builds on earlier setups, including Plasma Crystal 1, Plasma Crystal 2, PKE Nefedov [22], and Plasma Crystal 3 Plus [23]. The PK-1 and PK-2 systems were used to study complex plasmas in microgravity onboard the Russian space station *Mir*. The subsequent PKE Nefedov setup represented the first scientific experiment conducted onboard the International Space Station (ISS) from 2001 to 2005. Its successor, the PK-3 Plus, operated on the ISS from 2006 to 2013. The PK-4 experiment used in this study has been in operation onboard the ISS since 2014, supporting experiments on complex plasmas.

The formation of ordered structures in complex plasmas and the dynamics of their phase transitions are central topics of the analyses presented in this dissertation. These processes are governed by the effective interaction potential, which is determined not only by direct Coulomb forces but also by the collective responses of the background plasma, which significantly modify it. Debye screening is important because it defines the range of electrostatic interactions. The next section explains the theoretical principles of shielding and establishes the physical basis for the machine learning models developed in this study.

Screening and Collective Effects

When a test charge is introduced into a plasma, the free electrons and ions immediately respond to the local perturbation due to their high mobility. A cloud of opposite charge forms around the test charge and exponentially screens its electrostatic field [5]. The spatial range of this collective effect is characterized by the Debye length λ_D, which reflects the balance between thermal motion and the electrostatic ordering of charge carriers. The Debye length λ_D and the electrostatic potential $\phi(r)$ of a test charge Q can be derived from the following considerations. In the presence of an electrostatic potential $\phi(r)$, the electron density $n_e(r)$ is given by the Boltzmann distribution

$$n_e(r) = n_e \exp\left(\frac{e\,\phi(r)}{k_B T_e}\right), \tag{1.2}$$

where n_e denotes the unperturbed electron density far from the test charge, e is the elementary charge, k_B is the Boltzmann constant, and T_e is the electron temperature. The coordinate r denotes the radial distance from the test charge. Analogously, the ion density $n_i(r)$ at ion temperature T_i is described by

$$n_i(r) = n_i \exp\left(-\frac{e\,\phi(r)}{k_B T_i}\right), \tag{1.3}$$

where n_i is the unperturbed ion density.
The perturbation of the local charge density induced by the electrostatic potential $\phi(r)$ is given by

$$\rho(r) = -e\big[n_e(r) - n_e\big] + e\big[n_i(r) - n_i\big], \tag{1.4}$$

where $n_e(r)$ and $n_i(r)$ denote the position-dependent electron and ion densities, respectively, and n_e and n_i are their unperturbed background values far from the test charge.
For sufficiently large distances from the test charge, where the electrostatic energy is small compared to the thermal energy, i.e. $e\phi(r)/(k_B T_{e,i}) \ll 1$, the exponential terms in the density expressions can be simplified. Under this Debye–Hückel approximation, the charge density simplifies to

$$\rho(r) \approx -\frac{e^2 n_e}{k_B T_e}\,\phi(r) - \frac{e^2 n_i}{k_B T_i}\,\phi(r). \tag{1.5}$$

Substituting this expression into Poisson's equation,

$$\nabla^2\phi(r) = -\frac{\rho(r)}{\varepsilon_0}, \tag{1.6}$$

where ε_0 denotes the vacuum permittivity, yields the screened electrostatic potential of a test charge Q in a plasma,

$$\phi(r) = \frac{Q}{4\pi\varepsilon_0 r}\,\exp\!\left(-\frac{r}{\lambda_D}\right). \tag{1.7}$$

Here, r is the radial distance from the test charge, and λ_D denotes the Debye length, defined as

$$\lambda_D = \left(\frac{e^2 n_e}{\varepsilon_0 k_B T_e} + \frac{e^2 n_i}{\varepsilon_0 k_B T_i}\right)^{-1/2}. \tag{1.8}$$

If the region of interest is much larger than the Debye length, the plasma can be considered quasineutral. In a quasineutral plasma with single-charged ions, the approximation $n_i \approx n_e$ can be used. However, this approximation breaks down near the boundaries where the plasma interacts with vessel surfaces.

1.1 Complex Plasmas and Plasma Crystals

When micrometer-sized particles are injected into a low-temperature plasma, they become strongly negatively charged because of the higher mobility of electrons. Under appropriate plasma conditions, these particles can spontaneously organize into highly correlated structures, including string-like and crystalline phases. The differences in this self-organization arise from the particles' interactions and mobility. At high particle kinetic energies, the system behaves like a gas. As the system cools, the particle cloud reorganizes. As the kinetic temperature decreases, the system typically transitions from a gaseous phase to a liquid phase and, finally, to a crystalline phase. In the gaseous phase, the particles have high kinetic energy and are disordered. As the system cools, electrostatic interaction energy increasingly exceeds kinetic energy. This causes the system to become ordered and form crystalline structures.

Analyzing these structures is essential for characterizing complex plasmas. Numerous studies demonstrate that changes in the degree of microscopic order can significantly impact a material's mechanical and optical properties [24, 25]. Reconstructing the positions of particles and their correlations with neighboring particles allows one to identify the local order.

Due to the screening effects previously discussed, particles interact not through a pure Coulomb potential but rather through a screened Yukawa potential, which accounts for Debye screening:

$$\phi(r) = \frac{Z_d e}{4\pi\varepsilon_0 r}\,\exp\!\left(-\frac{r}{\lambda_D}\right), \tag{1.9}$$

where Z_d is the particle charge number, e is the elementary charge, ε_0 the vacuum permittivity, r is the interparticle distance, and λ_D is the Debye length.

A useful approximation for λ_D is

$$\lambda_D \approx \sqrt{\frac{\varepsilon_0 k_B T_i}{e^2 n_e}}, \tag{1.10}$$

provided that $T_e \gg T_i$ [5].
Since the particles form an additional plasma component, the quasineutrality condition becomes

$$n_e + Z_d n_d = n_i$$

[5], where Z_d is the particle charge number and n_d the spatial density of the particles. This relation is particularly relevant for Langmuir diagnostics, where ion density n_i can be measured directly [26].
Since the Yukawa interaction (1.9) only describes a repulsive force, the formation of ordered structures cannot be explained by this potential alone. For crystal formation, the dust cloud must also be compressed so that the particles are brought sufficiently close to each other. This compression usually occurs through electrostatic fields that surround the particles. Under laboratory conditions, gravity also leads to additional cloud compression.
The formation of plasma crystals therefore depends strongly on the strength of the electrostatic interactions and on the local particle density. A central measure of interaction strength is the Coulomb coupling parameter Γ:

$$\Gamma = \frac{Q^2}{4\pi\varepsilon_0 \, r_s \, k_B \, T_d}, \tag{1.11}$$

where $Q = Z_d e$ is the particle charge, r_s the mean interparticle distance, and T_d the particle temperature. Strong coupling occurs when $\Gamma \gg 1$.
The particle charge Z_d usually scales with the particle size and is on the order of $Z_d \approx 10^3 \, e$ per micrometer of particle radius [27]. The interparticle distance r_s is closely related to particle density and is often approximated by the Wigner–Seitz radius

$$r_s = \left(\frac{4}{3}\pi n_d\right)^{-1/3} \tag{1.12}$$

with n_d denoting the density of the particles. It is clear that the strength of the interaction increases with the density of the particles and thus with decreasing r_s.

The screening parameter κ quantifies the ratio between the interparticle distance r_s and the Debye length λ_D:

$$\kappa = \frac{r_s}{\lambda_D}. \tag{1.13}$$

Together with the Coulomb coupling parameter Γ, the screening parameter κ determines whether ordered phases can form. If Γ is sufficiently large compared to κ, the crystalline phase is the more stable state compared to the liquid phase.

In two dimensions, complex plasmas typically form hexagonal lattices [20], whereas in three dimensions isotropic crystal structures such as hexagonal close packed (hcp), face centered cubic (fcc), and body centered cubic (bcc) are commonly observed [16, 28]. However, under the influence of external factors, these structures may experience anisotropic distortions. Such effects are particularly relevant in direct current (DC) discharges. Because the plasma in the PK-4 experiment is generated by a DC discharge, these anisotropic effects are discussed in detail in the following chapter.

1.1.1 Ion Wake Effects

In DC plasmas, ions move predominantly along the electric field direction. Under each negatively charged particle, a region of positive space charge forms, commonly referred to as an ion wake. This region modifies the effective interaction potential in an anisotropic manner, as illustrated in Figure 1.1. When the external field is constant, the wake potential is asymmetric, resulting in an attractive force that is not reciprocal, which effectively violates Newton's third law [29]. However, if the ion stream is periodically reversed by an alternating electric field [30, 31], the time-averaged wake potential becomes symmetric and therefore reciprocal.

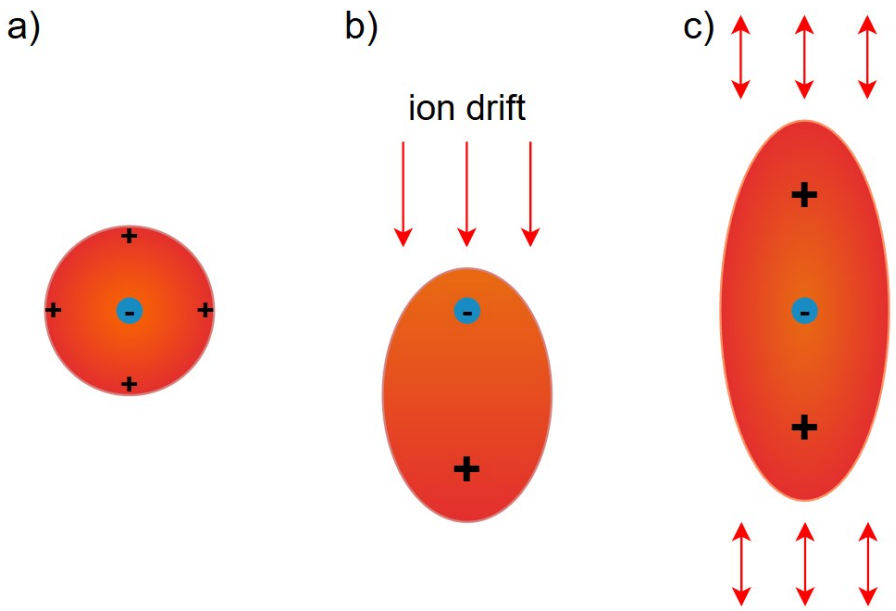

Figure 1.1: Particle potentials: a) Yukawa potential, b) effective potential in a direct current field, and c) potential in the polarity switching mode.

Ivlev et al. [31] showed that the effective wake potential can be expressed in terms of multipoles, with the dipole term providing the dominant asymmetric contribution. The resulting potential contains a screened repulsive component and an attractive component downstream of the ion flow:

$$\phi(r,\vartheta) \simeq \frac{Q}{4\pi\varepsilon_0}\left[\frac{e^{-r/\lambda_D}}{r} - 2\sqrt{\frac{2}{2\pi}}\,\frac{M_T\lambda_D^2}{r^3}\cos\vartheta - (2-\frac{\pi}{2})\,M_T^2\,\frac{\lambda_D^2}{r^3}\left(3\cos^2\vartheta - 1\right) + \cdots\right]. \tag{1.14}$$

Equation (1.14) represents a multipole expansion of the screened interaction potential in spherical coordinates, where dipole and quadrupole terms introduce anisotropic corrections to the isotropic Yukawa interaction. The angle between the direction of the ion drift and the position vector r is denoted by ϑ.

The thermal *Mach* number is defined as $M_T = u_i/v_T$, where u_i is the ion drift velocity and $v_T = \sqrt{k_B T_i/m_i}$ the thermal ion velocity.
The strength of the wake potential depends on the Debye length. The attractive quadrupole contribution scales as $\propto p^{-3} I^{-1}$ and is particularly strong at low ion currents I and low neutral gas pressures p [31]. Consequently, both the strength and the angular structure of the interaction potential are strongly controlled by the discharge parameters and the geometry of the ion drift. In DC operation, a stationary ion flow develops along the field direction. A stable ion focus forms behind each particle and generates a strongly anisotropic dipolar wake field [31]. This leads to nonreciprocal forces, which are characterized by the fact that the focusing area behind a particle exerts a stronger attractive force on the downstream particle than vice versa. The system is therefore non-Hamiltonian and tends to form particle chains aligned with the electric field.
When the electric field is periodically reversed, the structure of the effective potential changes. Because electrons, ions, and dust particles have significantly different masses, they respond differently to temporal variations of the electric field.
Because of their small mass, electrons respond almost instantaneously to temporal field variations. Their characteristic response time is determined by the electron plasma frequency ω_{pe}:

$$\omega_{\mathrm{pe}}^2 = \frac{n_e e^2}{m_e \varepsilon_0}. \tag{1.15}$$

Electrons with mass m_e can respond to perturbations with frequencies in the gigahertz range.
Ions respond more slowly due to their higher mass. The plasma-ion frequency ω_{pi} is

$$\omega_{\mathrm{pi}}^2 = \frac{n_i e^2}{m_i \varepsilon_0}, \tag{1.16}$$

and typically lies in the megahertz range.
Dust particles, being the heaviest charged species in complex plasmas, respond the slowest. Their plasma frequency ω_{pd} is

$$\omega_{\mathrm{pd}}^2 = \frac{n_d Z_d^2 e^2}{m_d \varepsilon_0}, \tag{1.17}$$

and is typically on the order of a few kilohertz.
In radio-frequency RF discharges operating at frequencies of several megahertz, ions respond too slowly to follow the rapid variations of the electric field. The time-averaged ion drift vanishes, causing the dipolar (cosine-like) contribution of the wake potential to average out over many cycles, and the effective interaction potential becomes symmetric and nearly isotropic.

The polarity switching mode of the PK-4 experiment creates a special intermediate regime. The switching frequency is between 100 and 1000 Hz and low enough for ions to follow the field. A dipolar wake potential forms during each alternation, with its orientation periodically reversing. Over many cycles the dipole contribution averages out, while the quadrupole contribution persists. Ivlev et al. [31] show that this produces an anisotropic but reciprocal potential as illustrated in Figure 1.1. The system is therefore Hamiltonian in this mode.
In polarity switching mode an anisotropic quadrupolar wake field remains that generally arranges the particles into chain-like structures along the electric field direction. Depending on gas pressure, switching frequency, and external forces, crystalline structures may also form. In addition to isotropic fcc, hcp, and bcc phases, anisotropic structures such as face centered orthorhombic (fco), body centered orthorhombic (bco), and body centered tetragonal (bct) appear [32, 33], as illustrated in Figure 1.2.

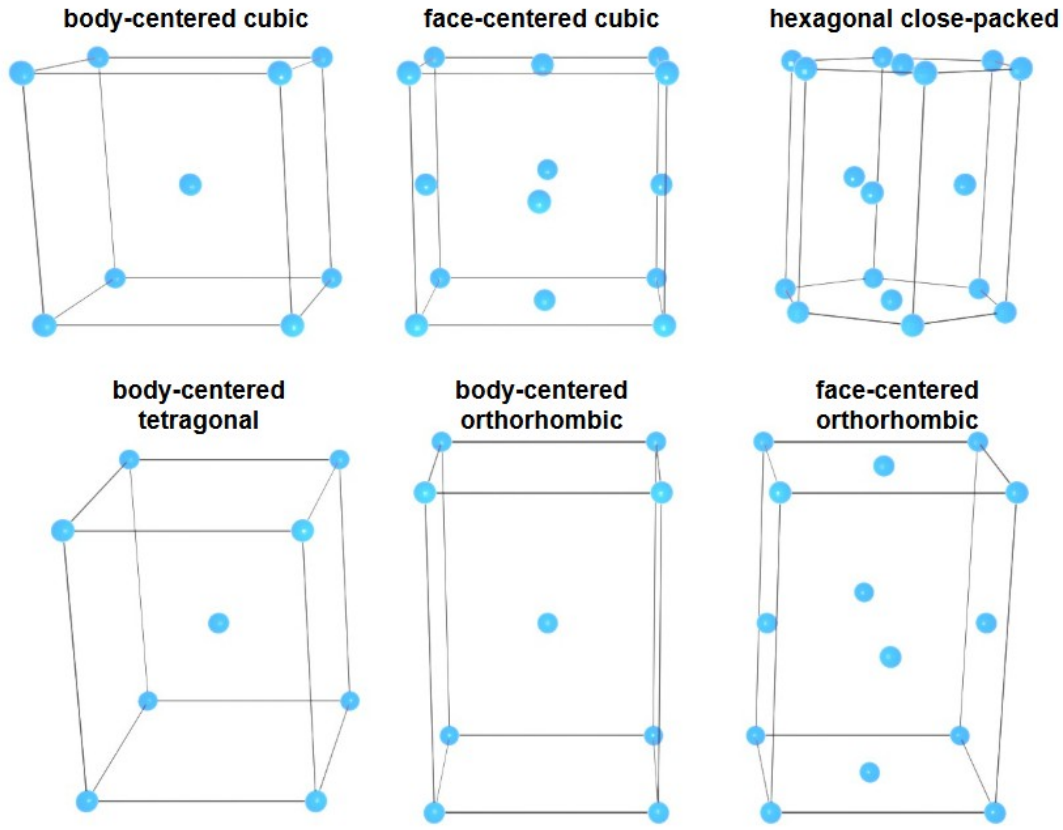

Figure 1.2: Three dimensional representations of the most important crystalline structures in complex plasmas. Blue spheres indicate particle positions within the corresponding unit cells, and black edges outline the geometric shapes of the cells.

A central challenge in analyzing such crystalline structures is that experimental datasets typically contain multiple phases simultaneously.

Isotropic and anisotropic crystal structures often coexist within the same particle cloud and exhibit different levels of noise and distortion depending on their spatial position.
A major reason is the gravitational compression present under laboratory conditions. The particle density varies significantly with height, which alters the screening parameter κ and shifts the locally preferred crystal structure [34]. Additional variations arise from spatially inhomogeneous plasma parameters. These variations are particularly pronounced in boundary regions. Additional sources of uncertainty arise from the experimental acquisition process itself. These include limited precision in three-dimensional reconstruction, errors in particle detection, and Brownian motion of the particles. These effects generate point clouds that are noisy, slightly displaced, or incomplete, making it difficult to identify local structures. To address these uncertainties, Publication I introduces a method for determining particle positions with high precision.
Several established methods exist for the structural analysis of three dimensional crystal systems. This includes bond orientational order parameters (BOOP) [35], pair and triple correlation functions [34, 36], common-neighborhood analysis (CNA) [37], and Minkowski-based measures [38]. While these methods provide valuable insights, they face limitations in multiphase systems, where they are often sensitive to noise, involve user-defined parameters, or lose accuracy near phase boundaries.
The work of Dietz et al. [28] offers a promising approach that combines several parameter-free geometric and topological descriptors into a unified signature that can be analyzed with classical machine learning techniques. Building on these developments, Publications II and III aim to advance structural identification in complex plasmas using modern deep learning methods. These approaches include point-cloud neural architectures such as PointNet and symmetry-equivariant models such as the SE(3) Transformer, which learn structural representations directly from three-dimensional particle coordinates. These models are robust to experimental disturbances and offer significantly better generalization capabilities than classical rule-based methods.
The following chapter describes the setup of the PK-4 experiment, which provides the datasets and the physical context for the analysis presented in this dissertation.

1.2 Plasmakristall 4 Experiment

The PK-4 experiment (see Figure 1.3), described in detail by Pustylnik et al. [21], has been installed in the European Columbus module of the ISS since 2014 and has been operational there since 2015. The Plasma and Space Physics Group at Justus Liebig University Giessen has access to two models of PK-4. The first is an Engineering Model (EM), modified for operation under microgravity conditions during parabolic flights. The second is the Science Reference Model (SRM) No. 1, which is identical in design to the flight model installed onboard the ISS. All investigations presented in this dissertation were conducted using the EM.

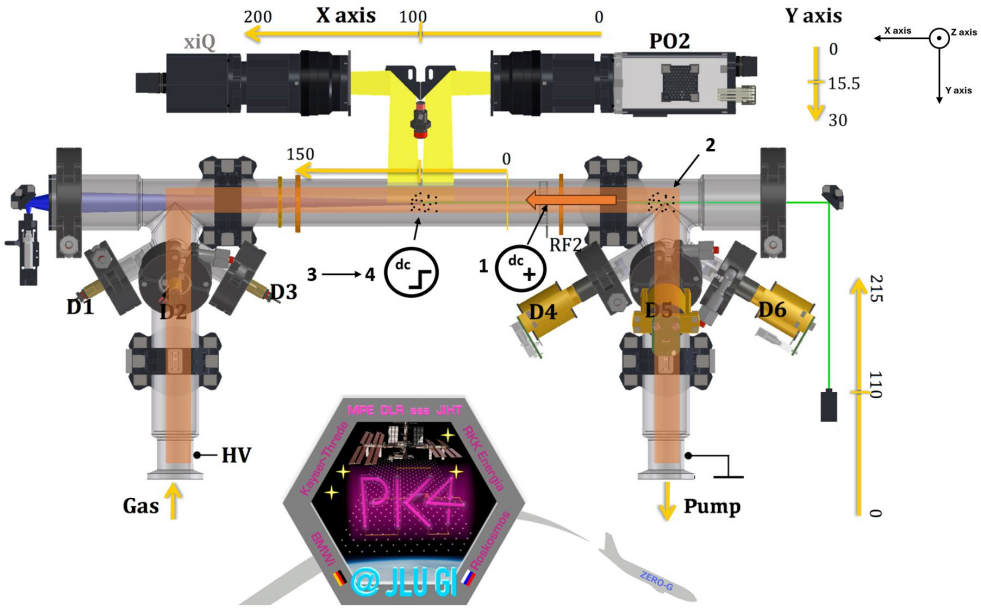

Figure 1.3: Sketch of the PK-4 experiment, provided by the Thoma research group of JLU Giessen. Shown are the ignition of the DC plasma (1), microparticle injection (2), the arrival of microparticles in the PO camera field of view (3), and trapping through polarity switching mode (4).

Plasma Chamber

The plasma chamber consists of a π-shaped glass tube with an inner diameter of 30 mm. It is composed of a 500 mm long main tube and two side tubes, each 180 mm in length. The central working region covers the middle 200 mm of the main tube and is designed to allow full optical access by the camera system.

The active and passive electrodes are located at the ends of the side tubes. A direct current discharge is generated between these electrodes. The active electrode simultaneously serves as the gas inlet and is electrically insulated by a porous ceramic element.

Gas and Vacuum System

The gas supply system allows operation with neon, argon, or an argon-oxygen mixture. The working pressure can be stabilized between 10 Pa and 250 Pa. The gas flow rate is adjustable between 0.1 and 10 sccm. A turbomolecular pump, backed by a mechanical forepump, achieves a base pressure below 2×10^{-5} mbar. Pressure control is provided by several piezoelectric pressure sensors and electronic controllers.

Microparticle Dispensers

Six dispensers are available for injecting microparticles into the plasma, arranged symmetrically on the side tubes of the plasma chamber. Three of the dispensers operate on a gas jet principle and inject particles using short gas pulses. The remaining dispensers employ an electromagnetic shaking mechanism. This mechanism is controlled by the parameters on time T_{on}, relaxation time T_{off}, and the number of shaking cycles N_{shakes}.
The dispensers contain monodisperse melamine formaldehyde particles with diameters between 1.3 and 10.6 μm. For experiments that require minimal disturbance, the shaker-type dispensers are preferred, since they generate essentially no additional gas flow compared to gas jet dispensers. In all experiments presented here, exclusively shaker-type dispensers were employed.

Plasma Generation

The main plasma source of PK-4 is a DC discharge driven by a bipolar high-voltage generator. This source provides currents from -3.1 to 3.1 mA and voltages up to 2.7 kV. The discharge can be operated either in stationary DC mode or in polarity switching mode. The duty cycle

$$\delta = \frac{t_1}{t_2} \tag{1.18}$$

defines the ratio of the duration of the positive polarity phase t_1 to the total period t_2. As already mentioned, the switching frequency can be set between 100 and 1000 Hz.
Due to their large mass and inertia, the particles cannot follow the rapid alternation of the electric field. They respond only to the time-averaged force. This makes it possible to keep the particles stable within the camera field of view or to move them in a controlled way by adjusting the duty cycle.
In addition to the DC discharge, an inductively coupled RF discharge is available. It is generated by two coils wound around the glass tube, one of which can be moved along the axis of the tube. The RF source operates at a frequency of 81.36 MHz and can deliver up to 5 W of power per channel. However, the RF discharge was not utilized in the experiments presented in this dissertation.

Optical Diagnostics

Two high-resolution camera systems are available for particle observation: a CCD camera (PO2, 1600×1200 *pixels*) and a CMOS camera (xiQ, 2048×2048 *pixels*). Both cameras are mounted on a precision translation stage, enabling movement in both the axial and radial directions. The xiQ camera was used for our studies due to its superior resolution.
Illumination is provided by a 532 nm laser that is shaped into a thin light sheet. This configuration enables two-dimensional imaging, which can be used to reconstruct two- or three-dimensional particle distributions.
The setup is also equipped with a Plasma Glow Observation System that generates three simultaneous views of the plasma chamber using a kaleidoscopic mirror arrangement. Two of these views are spectrally centered on characteristic neon emission lines and provide qualitative information about the spatial distribution of plasma emission. The third view is spectrally integrated and includes the scattered light of the illumination laser, which allows the global particle distribution to be visualized.

1.2.1 Onboard Data Processing and Autonomous Experiment Control

Since Earth's gravitational field has a direct influence on the behavior of the particles in the plasma, additional experiments were carried out under microgravity conditions as part of this work. Such conditions can be realized in several ways, including drop tower experiments [39], parabolic flights [40], sounding rocket missions [41], or experiments onboard the ISS. The microgravity data analyzed in this dissertation were obtained from parabolic flight experiments conducted during the German Aerospace Center (DLR) campaigns 42 [42] and 44 [43]. These campaigns were organized by DLR and carried out by Novespace [40].
Each campaign is composed of three flight days, with one flight per day and a total of 31 parabolas per flight. A single parabola consists of approximately 20 s of hypergravity ($\approx 2g$), followed by 22 s of microgravity ($\approx 0g$) and another 20 s of a hypergravity phase. The maneuvers take place at altitudes between 6000 and 8500 m.
The microgravity phase therefore defines the critical time window for data acquisition. Consequently, the experiments are required to be conducted within the aforementioned time window of 22 s.

Integration of an Onboard AI System

For the parabolic flights, the EM was extended by an NVIDIA Jetson AGX Orin Developer Kit module with the following key specifications:

Component	Specification
CUDA cores	2048 CUDA cores and 64 Tensor cores
Processor	12 core ARM Cortex A78AE
Memory	64 GB LPDDR5 RAM (204.8 GB/s bandwidth)
AI performance	up to 275 TOPS

Table 1.1: NVIDIA Jetson AGX Orin key specifications.

This computational capacity enables real-time onboard analysis of camera data. As a result, AI-based methods for detecting physically relevant events can already be applied during the parabolic flights, which is particularly important given the short duration of the microgravity phases.
In principle, this hardware is also well suited for experiments onboard the ISS and is therefore considered for the follow-up project COMPACT [44]. However, for such mission scenarios, operational reliability and fault tolerance must be carefully taken into account. It is important to note that the NVIDIA Jetson AGX Orin Developer Kit does not provide Error Correction Code (ECC) protection for its RAM. Memory bit flips, which may be induced by radiation effects, electrical noise, or environmental influences, can lead to silent data corruption and affect computing accuracy.
As part of a Master's thesis conducted within the AIPEX project, investigations were carried out to study the impact of memory bit flips on the accuracy and performance of neural networks. The results suggest that isolated memory errors can result in measurable degradation of inference accuracy or unstable network behavior. The Industrial variant of the Jetson AGX Orin module, in contrast, supports ECC-protected LPDDR5 memory, which significantly increases system robustness and reliability. For long-duration and radiation-exposed mission scenarios, such as experiments conducted on the ISS, the use of ECC-protected memory is therefore strongly recommended to ensure reliable onboard data processing.

Adaptive Experiment Control

The Jetson module is fully integrated into the PK-4 control system via the CAN bus and thus enables autonomous control in real time. Based on image data evaluated directly onboard, ordered structures can be detected automatically. Experimental parameters are then adapted dynamically to the current plasma state, for example, through continuous fine-tuning of the duty cycle. At the same time, the control logic is integrated in a manner that enables active stabilization of the particles within the camera field of view. Furthermore, an automated particle detection routine was implemented, allowing the deceleration of the particle cloud in a controlled manner and its subsequent capture within the observation region.

The structural complexity described above, combined with the large volume of experimental data generated in experiments at PK-4, renders purely rule-based or manually tuned analysis methods increasingly insufficient. To address these limitations, this work adopts modern machine learning techniques that can learn structural representations directly from data while remaining robust to noise and distortions. Therefore, the subsequent chapter presents the theoretical basis of machine learning and offers a systematic overview of the neural network architectures employed in this dissertation.

1.3 Theoretical Background of Machine Learning and the Network Architectures Used

Machine learning (ML) is a subfield of artificial intelligence that deals with developing algorithms that derive patterns and correlations from data without being explicitly programmed or manually parameterized. Classical ML methods typically rely on comparatively low-capacity model classes such as linear regression, decision trees, or support vector machines [45]. In contrast, deep learning is a specialized field that uses artificial neural networks with multiple hidden layers. This feature enables deep learning models to capture nonlinear, hierarchical, and abstract feature representations, representing a significant advance in machine learning capabilities [46]. This is especially useful when the underlying physical processes are complex, noisy, or difficult to analyze.
At its core, supervised learning aims to approximate a function $f(x)$ that maps elements of an input space X to corresponding outputs in a target space Y. A fundamental learning paradigm for constructing such a function is supervised learning. In this context, the training dataset consists of input data X_i and their associated labels Y_i. The model is trained to make predictions that correspond as closely as possible to Y_i. By optimizing the model on labeled examples, it learns to generalize the underlying patterns to previously unseen data. The model is configured to learn a representation of the underlying structure

$$f_\theta : X_i \mapsto Y_i, \tag{1.19}$$

by optimizing the parameters θ such that the predictions match the labeled targets as closely as possible [46]. Supervised learning is therefore particularly well suited to tasks such as classification, regression, or object detection, for which labeled training data are available.
In physics, ML and especially deep learning open up new possibilities for analyzing complex systems, identifying variable structures, and extracting latent patterns from experimental measurements. Review articles such as Mehta et al. [47], Tang et al. [48], and Carleo et al. [49] highlight the growing importance of data-driven methods in research areas ranging from statistical physics and quantum mechanics to strongly coupled plasmas.
In this work, deep learning methods are used to analyze image data and three dimensional particle distributions in complex plasmas and to extract structural information from them. The following sections therefore introduce the theoretical foundations of the network architectures that are used later in this dissertation: U-Net, PointNet, and the SE(3) Transformer. These models are designed to represent different classes of neural networks and target various data types, ranging from convolutional networks for image data and point cloud-based architectures to symmetry equivariant graph neural networks, which consistently incorporate spatial transformations.

Activation Functions

For neural networks to capture complex patterns and nonlinear relationships, they require activation functions. These are applied after each linear transformation and introduce nonlinearity; without them, a multilayer network would mathematically reduce to a single linear mapping.

One of the most widely used activation functions is the rectified linear unit (ReLU) [50]. For a given scalar input $x \in \mathbb{R}$, which denotes the pre-activation value of a neuron, the function is defined as

$$ReLU(x) = \max(0, x) = \frac{x + |x|}{2}. \tag{1.20}$$

ReLU passes the positive input values unchanged and sets the negative values to zero, which supports stable gradient flow. However, ReLU is not differentiable at the origin and produces piecewise-linear outputs, which can be undesirable in models that rely on smooth geometric or physical dependencies.
The softplus activation provides a smooth, fully differentiable approximation to ReLU and is often used when continuity and stable gradients are required [50]:

$$softplus(x) = \ln(1 + e^x). \tag{1.21}$$

Softplus avoids the abrupt cutoff of ReLU and yields smooth transitions even for small or negative inputs, which can be advantageous in geometry-aware architectures such as graph neural networks and equivariant models.
For binary classification tasks, the sigmoid function [46] is often used:

$$sigmoid(x) = \frac{1}{1 + e^{-x}}, \tag{1.22}$$

which maps any real value to the interval $(0, 1)$ and can therefore be interpreted as a probability. For multiclass problems, the softmax activation [51] is typically applied in the final layer:

$$softmax(x)_j = \frac{\exp(x_j)}{\sum_{k=1}^{K} \exp(x_k)}, \tag{1.23}$$

which converts the model outputs into a probability distribution over all K classes.

On this basis, a loss function is defined that measures the discrepancy between the model prediction $\hat{y}$ and the target y. For regression problems, the mean squared error (MSE) is commonly used:

$$MSE = \frac{1}{K}\sum_{i=1}^{K}(y_i - \hat{y}_i)^2. \tag{1.24}$$

The MSE quantifies the average squared deviation and penalizes large errors particularly strongly.
For classification tasks, the categorical cross entropy loss is typically employed:

$$CCE = -\sum_{i=1}^{K} y_i \cdot \log(\hat{y}_i), \tag{1.25}$$

with truth value y_i, predicted value $\hat{y}_i$ and the number of classes K. Since target labels are usually given in a one-hot encoding, cross entropy directly evaluates how much probability the softmax output assigns to the true class.
Model parameters are optimized using gradient based methods, in which the parameters are updated in the direction of the negative gradient of the loss function. Through the interaction of suitable activation functions and an appropriate loss function, neural networks can learn complex decision boundaries and generalize reliably.

Artificial Neural Networks

The supervised learning framework forms the basis for the use of modern deep learning models. Understanding the underlying network architectures is essential for physical applications such as the analysis of complex plasmas. This section outlines the key properties of artificial neural networks, which are the conceptual foundation for the rest of this chapter.
Neural networks consist of layers of artificial neurons that combine linear transformations with nonlinear activation functions. The classical example is the multilayer perceptron (MLP) [52], which forms the conceptual basis of many modern deep learning architectures [47]. An MLP consists of an input layer, several hidden layers, and an output layer (see Figure 1.4). Since each neuron is connected to all neurons in the next layer, such architectures are referred to as fully connected networks.
Despite its simple structure, the MLP is still widely used, for example as a classification head in more complex architectures such as PointNet or in various types of graph neural networks (GNNs) [53, 54]. The behavior of an artificial neuron can be described as a linear transformation of the inputs followed by a nonlinear activation. For the i-th layer, the activation $A^{(i)}$ is given by

$$A^{(i)} = g\left(W^{(i)}A^{(i-1)} + b^{(i)}\right), \tag{1.26}$$

where $W^{(i)}$ is the weight matrix, $b^{(i)}$ the bias vector, and g an activation function such as ReLU (or, in the output layer, softmax).

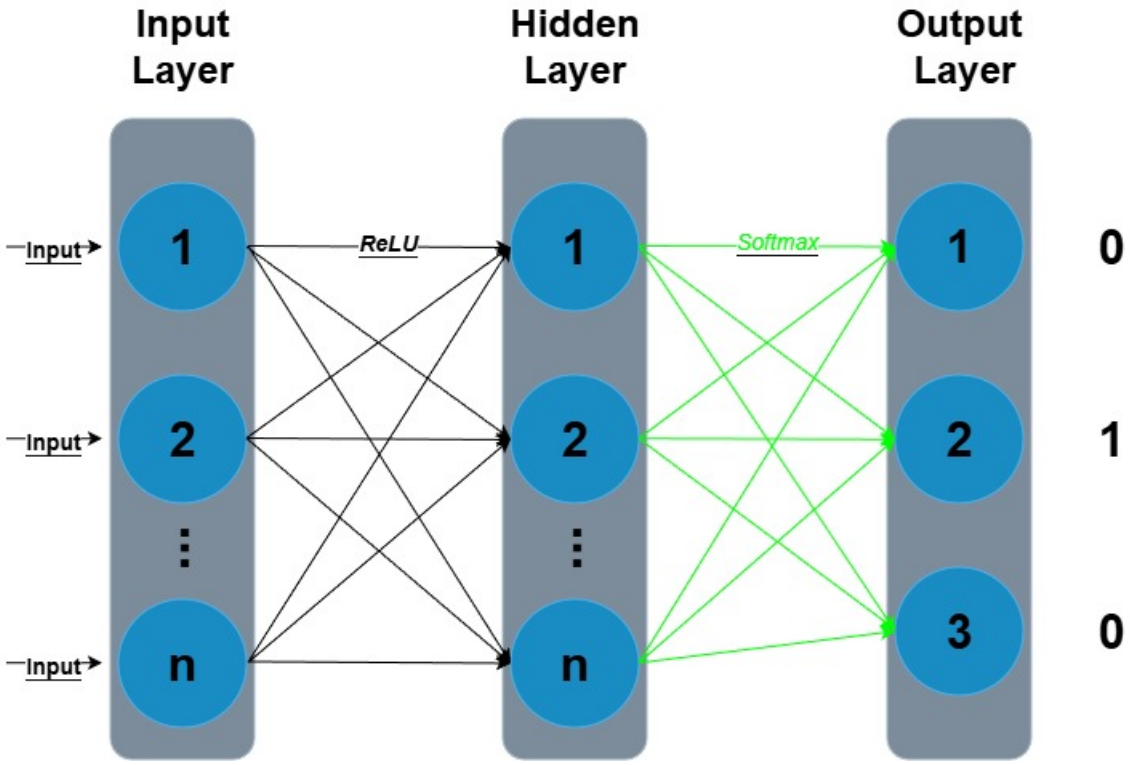

Figure 1.4: Schematic illustration of the MLP architecture with one-hot encoded output (neuron 2 is classified as active).

During training, the network parameters are optimized by gradient descent so that the model prediction $f_\theta(x)$ matches the target values as closely as possible. This is achieved using the backpropagation algorithm, which efficiently propagates the gradients of the loss function through all layers [55]. The universal approximation theorem states that even shallow networks can represent any continuous function in compact sets [56, 57]. Deep neural networks exploit this by using a hierarchical organization. Shallow layers capture local, low-level patterns, and deeper layers encode increasingly abstract, global structures. This property is particularly relevant to physical systems, which often have multiscale dependencies [49].

In the context of image data, this hierarchical processing is commonly realized by combining fully connected layers with convolutional and pooling operations. Classical convolutional neural networks (CNN) operate on regularly structured inputs such as images and derive translation-equivariant features through convolutional operations. A convolutional layer applies a small, trainable filter kernel across the input grid and computes locally weighted responses that emphasize characteristic spatial patterns, including edges, corners and textures [58, 59].

Mathematically, the discrete convolution of a two dimensional input I with a kernel k at spatial position (i, j) is given by

$$(k * I)(i, j) = \sum_m \sum_n I(i + m, j + n)\, k(m, n), \tag{1.27}$$

where the kernel size is $(2m+1) \times (2n+1)$. Because the same kernel is applied at all spatial positions, the resulting representation is equivariant to translations, meaning that a shifted input generates a correspondingly shifted feature map. This parameter sharing significantly reduces the number of trainable weights and enables convolutional architectures to learn spatial hierarchies in an efficient and data-driven manner.
To further condense information and enhance robustness against local perturbations, convolutional networks commonly incorporate pooling mechanisms. In max pooling, the output at location (i, j) is the maximum activation,

$$P_{i,j} = \max_{m,n} X_{i\cdot\hat{s}+m,\, j\cdot\hat{s}+n}, \tag{1.28}$$

where X denotes the input feature map, P is the result of the max-pooling operation, $\hat{s}$ is the stride, m and n specify the height and width of the pooling window, and $P_{i,j}$ represents the output at location (i, j) [46]. The stride $\hat{s}$ specifies how many pixels the filter or pooling window moves with each step, thereby determining how much the output is spatially reduced. Whereas average pooling aggregates the mean value within the same window by computing

$$P_{i,j} = \frac{1}{m\, n} \sum_m \sum_n X_{i\cdot\hat{s}+m,\, j\cdot\hat{s}+n}. \tag{1.29}$$

Max pooling is typically used for object detection tasks, as it highlights the strongest and most relevant features, while average pooling is used when a more uniform, information-preserving representation is required, such as for reconstruction or smoothing tasks [46]. Both operations reduce spatial resolution. They retain essential feature characteristics. This supports the formation of increasingly abstract representations.
These mechanisms form the computational basis of many successful image-processing architectures, including the U-Net model [60] introduced in the following section. However, CNNs are fundamentally based on the assumption of a regular grid structure and fixed local neighborhoods. This assumption is incompatible with the irregular geometry of three dimensional particle configurations in complex plasmas, where point clouds do not have a uniform sampling pattern or a canonical notion of neighborhood. As a consequence, CNNs cannot directly encode the geometric relationships present in such systems, which motivates the use of architectures specifically designed for non-Euclidean data, such as PointNet [53] and modern graph neural networks [54]. These models support the direct processing of unordered point sets and explicitly incorporate structural relationships between particles into the feature representation. They thus form a central methodological basis for the approaches developed in this work for the structural analysis of complex plasmas.

1.3.1 U-Net Architecture

The U-Net architecture [60] was originally developed for biomedical image segmentation and is specifically designed to combine semantic context with high spatial resolution. These properties make it particularly well suited for physical applications in which precise detection and separation of individual objects is necessary, such as the detection and localization of microparticles in complex plasmas. A key feature of the architecture is the use of skip connections, which transfer high-resolution spatial information from the encoder to the decoder. This enables precise segmentation, even of small or closely spaced particles.
The U-Net architecture follows a symmetric encoder-decoder design with a contracting path for feature extraction, a compressed latent space (bottleneck), and an expanding path for reconstructing the output image (see Figure 1.5).

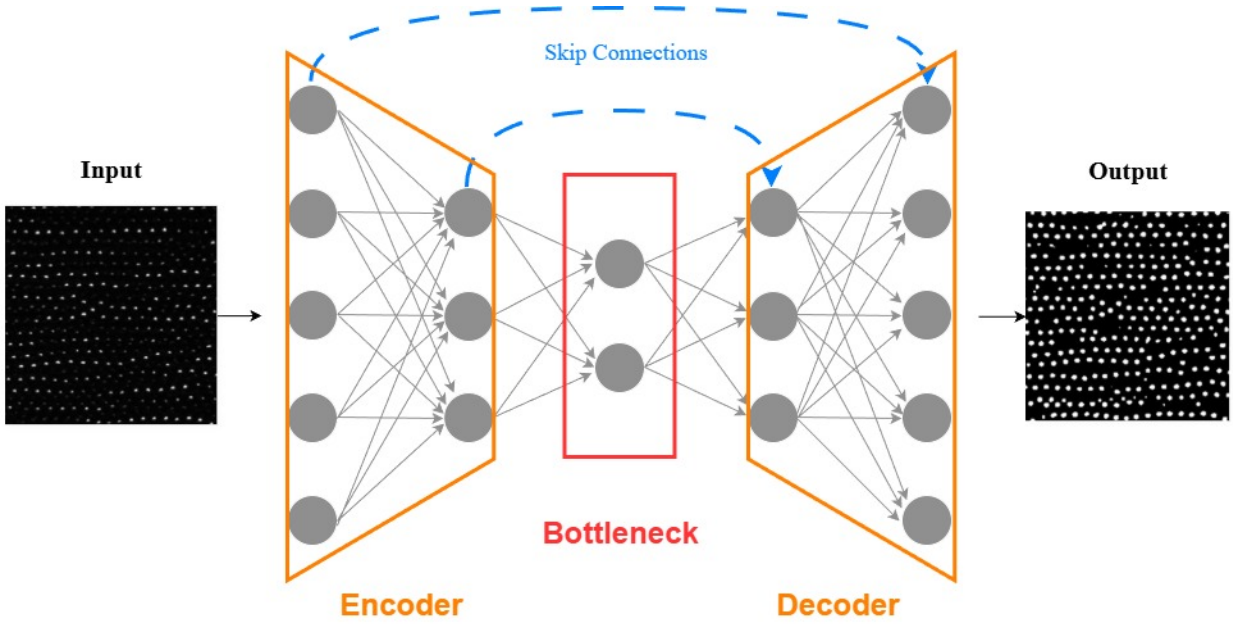

Figure 1.5: Schematic representation of the U-Net architecture with encoder, bottleneck, decoder and skip connections.

Encoder (Contracting Path) The encoder extracts relevant features through successive convolutional layers, nonlinear activation functions such as ReLU, and subsequent pooling operations. As a result, spatial resolution is reduced while the number of feature maps increases.

Bottleneck The latent space or bottleneck contains the deepest representation of the image. It provides a highly compressed representation in which global contextual information is concentrated. This representation serves as the starting point for the reconstruction process in the decoder.

Decoder (Expanding Path) The decoder reverses the compression introduced by the encoder progressively. This process involves upsampling and transposed convolutions. The characteristic skip connections concatenate the corresponding encoder feature maps with the decoder feature maps. In this way, both global and local information contribute to the segmentation, enabling pixel-accurate reconstruction.

Advantages and Application

U-Net combines local and global image information, efficiently reuses high-resolution features via skip connections, and can be adapted to different computational budgets by varying the network depth.
In Publication I [61] (see Chapter 2), U-Net was used for automated segmentation of microparticles in PK-4 image data. For each input image, the network produces a binary segmentation mask that assigns each pixel a probability of belonging to a particle. Particle positions are then obtained by computing the centroids of the brightest connected pixel regions. This allows reliable localization of particles even in strongly noisy or partially overlapping image regions.
For rapidly moving particles, this method offers clear advantages over classical thresholding or filtering approaches [62]. Localization is not based on single pixel intensities but on learned shape and context features, which makes detection significantly more robust under varying illumination conditions and overlapping structures. The resulting segmentation allows for the precise determination of particle trajectories and improves the stability of subsequent analyses.
The U-Net based segmentation developed in this study served as the foundation for many subsequent studies within the PK-4 experiment. The high accuracy of the reconstructed positions enabled detailed analyses of wave fronts, anisotropic structure formation, and electro-rheological effects [19]. In addition, an extended network variant was trained to reliably detect ordered chain-like structures [63].
To make the method usable in different hardware environments, we employed both full-size and compact U-Net variants. The full-size version provides maximum segmentation accuracy, while compact models with fewer parameters enable efficient processing in settings with limited resources, such as during parabolic flight campaigns. The particle positions extracted by U-Net serve as the quantitative input for all subsequent structural analyses.

1.3.2 Reconstruction of Three Dimensional Particle Positions

The particle positions detected by U-Net in individual camera images form the basis for the three dimensional reconstruction of the particle cloud. In the PK-4 data are acquired through a sequential scan along the y-axis. To achieve this, the camera and the illumination laser are mounted on a precision translation stage and moved together along the scan direction. In all experiments presented in this work, the scan was performed at a constant velocity of $5\,\mathrm{mm\,s^{-1}}$. As the stage moves, two dimensional images are recorded continuously at a fixed frame rate, which is typically 60 fps.
The camera observes the x–z plane orthogonally, such that each recorded image corresponds to a planar slice of the plasma volume. From the known scan velocity and frame rate, the distance between consecutive image planes can be determined, allowing the recorded images to be stacked with a well-defined spacing along the scan direction. By stacking these slices accordingly, a volumetric dataset is obtained that encodes the three dimensional intensity distribution of the particle cloud (see Figure 1.6).

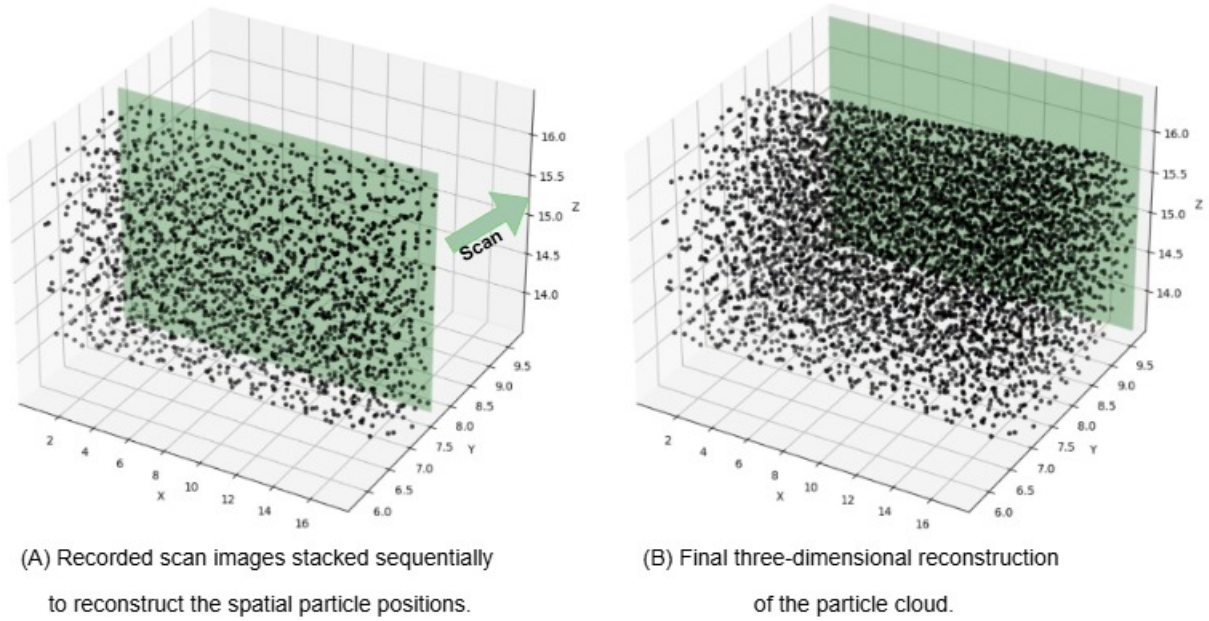

Figure 1.6: Schematic illustration of the scan along the y axis (A) and the resulting point cloud (B).

Within this reconstructed volume, the detected particles are consistently associated across images using an optimized self-organizing map (SOM) [64, 65]. The SOM assigns particles in successive images to their nearest neighbors and thus enables continuous tracking of individual particles across the entire scan. It should be noted that the particles captured within the camera field of view are not perfectly stationary during the scanning process.

Although the experimental conditions are adjusted to minimize particle motion and to confine the particle cloud as stably as possible, a residual drift of the cloud is always present. Experimental parameters are adjusted such that the residual motion is predominantly unidirectional, such that all particles drift coherently in the same direction during the scan. During the three dimensional reconstruction, this residual drift is accounted for by evaluating the mean displacement of the tracked particle positions over the scan. Individual trajectories are corrected by subtracting the average displacement. Final three-dimensional particle positions are obtained by averaging corrected positions along the scan direction. This procedure reduces reconstruction artifacts caused by residual motion and improves the spatial consistency of the reconstructed particle cloud. Conceptually, this approach is similar to tomographic reconstruction, in which information from individual slices is combined to create a three dimensional volume. Combining neural segmentation and volumetric reconstruction is a crucial intermediate step that transforms experimental raw data into a representation suitable for point cloud based methods, such as PointNet. On this basis, both local structural properties of individual particles and collective order parameters and symmetries within the particle cloud can be analyzed systematically.

1.3.3 PointNet and WignerNet

Based on reconstructed particle positions, PointNet [53] offers a solid architecture for learning from unordered point sets. Unlike image or grid data, point clouds do not lie on a regular structure. Rather, they form finite sets of points in three dimensional space without a natural ordering. Consequently, classical neural network architectures, such as convolutional or sequence models, cannot be applied directly to point clouds. Therefore, a suitable architecture must be permutation-invariant, meaning it produces the same output regardless of the input point ordering.
PointNet was designed specifically to process point clouds directly. The network initially treats each point independently of the others and applies an identical MLP to its coordinates, thereby producing locally defined feature vectors. Before this step, a learnable transformation network, or T-Net, transforms the point coordinates into a canonical reference frame. The T-Net learns a linear transformation of the point cloud to compensate for geometric variations such as rotations and translations. It outputs a matrix $T \in \mathbb{R}^{3\times3}$ that is optimized during training such that similar configurations are mapped to comparable regions in feature space regardless of their orientation. A regularization term of the form

$$\mathcal{L}_{\text{reg}} = \|I - TT^{\top}\|_F^2 \tag{1.30}$$

ensures that T remains close to an orthogonal matrix and does not introduce distortions. After normalization, the locally extracted point features are aggregated into a global representation via a symmetric pooling operation. This aggregation ensures permutation invariance and identifies the points that are most influential for specific feature dimensions. Qi et al. [53] show that these points form a so-called critical point set, a small subset of the point cloud that carries the essential geometric information. As long as these points are preserved, the global representation will remain highly robust in the presence of noise, outliers, and missing points. The global descriptor is then processed by a classical feedforward neural network, which performs the final classification.

Advantages and Application

Compared to alternative methods of processing three dimensional point data, PointNet offers several significant advantages. Voxel-based approaches discretize the point cloud on a regular grid, resulting in a loss of fine structural detail and rapidly increasing memory requirements with resolution. This poses a serious practical limitation for experimental datasets containing several thousand particles. Multi-view methods project the point cloud onto different image planes and enable the use of established convolutional networks. However, they are sensitive to perspective distortions and heavily depend on the choice of projections.
PointNet overcomes these limitations by operating directly on unordered point coordinates. This preserves the continuous geometric representation of the particle positions without discretization.

The combination of pointwise feature extraction, symmetric aggregation, and T-Net results in high robustness to the typical experimental uncertainties present in real plasma crystals. These properties make PointNet particularly well-suited for analyzing reconstructed point clouds from the PK-4.

Building on the PointNet architecture, Publication II [66] (see Chapter 3) introduces an adapted model called WignerNet. Although PointNet can be applied directly to the three dimensional particle positions of strongly coupled plasma systems, it quickly faces limitations in practical structure classification. The raw point positions of different crystal structures often differ only slightly. Therefore, even small measurement uncertainties or thermal fluctuations can significantly reduce discrimination. At the same time, multiple crystal structures must be reliably identified within a single particle cloud despite their occurrence at different noise levels and local distortions. Furthermore, PointNet requires sufficiently dense point sampling for stable classification, which the raw particle positions do not guarantee.

Therefore, robust identification requires a representation that uniquely and reliably encodes the local neighborhood of a particle without relying on manually tuned parameters. WignerNet addresses this requirement precisely. It derives structurally relevant geometric features from three dimensional positions, providing a much more discriminative basis for classification.

The structural basis of the method is the Wigner-Seitz cell, which is defined uniquely for each crystal structure and retains its essential geometric properties, even in the presence of strong noise. The classification performance of a PointNet-based model depends heavily on the number of points representing the underlying structure. The denser these points are distributed across the structure, the more precisely the model can capture structural differences. However, a complete sampling of the entire cell surface would require a very large number of points, which would substantially increase the computational cost.

To avoid this issue, a more efficient strategy was chosen. Only the edges of the Wigner-Seitz cell are sampled with a fixed number of support points, rather than sampling the entire surface. This compact representation preserves the cell's essential geometric features while enabling robust and efficient processing by the neural network.

First, the Wigner-Seitz cells are obtained through Delaunay triangulation of the point cloud. Subsequently, 1000 uniformly distributed support points are sampled along the edges of each cell. This process produces a standardized, comparable point cloud that serves as input for the network. Based on these point clouds, the model classifies the underlying crystal structure, for example fcc, bcc, or hcp (see Figure 1.7).

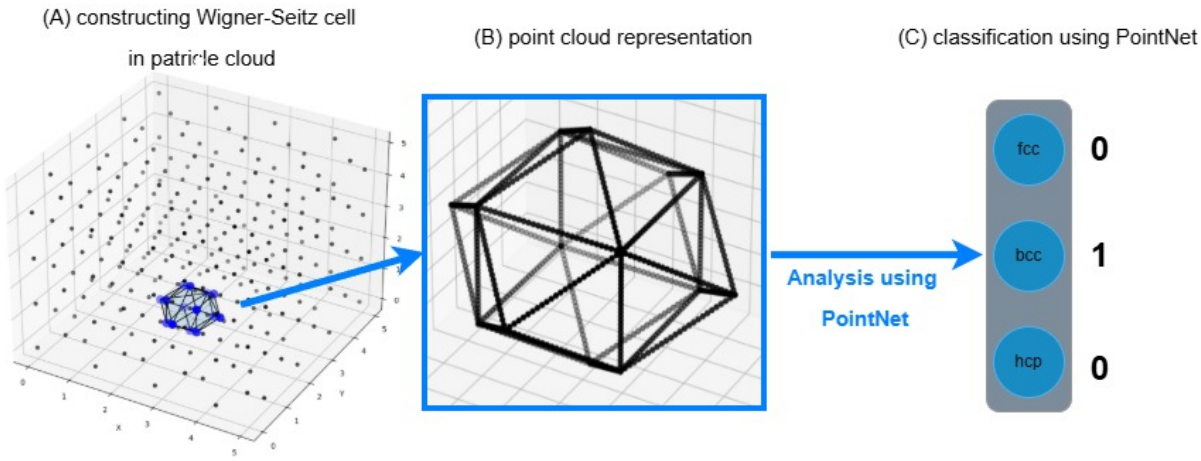

Figure 1.7: Schematic illustration of the WignerNet based analysis of a bcc structure.

In contrast to classical vector- or descriptor-based analysis methods, which rely on explicitly defined structural features and are often sensitive to noise, WignerNet operates directly on three dimensional position data. There is no need to define neighborhoods, symmetry axes, or geometric invariants manually. The network learns these relationships from the training data, which makes it more flexible and widely applicable.
Studies on synthetic and labeled datasets show that WignerNet identifies local crystal structures with high accuracy and remarkable robustness. The model has also been successfully applied to experimental PK-4 data, where it produces consistent structure classifications even under realistic, noisy conditions. WignerNet thus opens up new perspectives for studying phase transitions and ordering processes in complex plasmas.
When taking into account highly variable anisotropic structures with varying spatial orientations and cell geometries, PointNet reaches its conceptual limits. In particular, the simultaneous classification of isotropic and anisotropic phases under varying noise levels becomes increasingly unreliable, as PointNet lacks an explicit mechanism to encode physically meaningful variations in edge lengths and anisotropies.

1.3.4 SE(3) Transformer

A detailed analysis of anisotropic particle configurations requires a model that respects the geometric structure of physical space rather than learning it implicitly from data. Methods such as PointNet are permutation-invariant but do not encode how a three dimensional system transforms under rotations and translations. As a result, they must learn these transformations entirely from examples, which reduces sample efficiency and limits generalization to unseen orientations. The SE(3) Transformer [67, 68, 69] overcomes this limitation by enforcing strict equivariance with respect to the special Euclidean group SE(3). Its internal representations transform exactly as the input does when the entire system is rotated or translated, which is essential for analyzing plasma crystals whose orientations may vary freely in experiments.
Conceptually, the SE(3) Transformer extends the transformer architecture to spatial geometry. As in classical transformers, the model determines the relevance of interactions through an attention mechanism based on queries, keys, and values. Each particle is projected into these representations, where the query encodes what information a particle seeks, the key encodes what another particle provides, and the value encodes what information is ultimately transmitted. The scalar product $q_i^\top k_j$ measures the physical relevance of particle j for particle i. The pair-based attention weights for a given query q_i

$$\alpha_{ij} = \frac{\exp(q_i^\top k_{ij})}{\sum_{j'} \exp(q_i^\top k_{ij'})}, \tag{1.31}$$

can be interpreted as effective, dynamically learned interaction strengths [67]. The similarity between a query and a key therefore determines how strongly two particles interact. This produces a flexible and data-driven interaction pattern, allowing the model to capture both short-range and long-range correlations without requiring predefined neighborhoods.

Embedding Physical Symmetry: SE(3) Equivariance

To apply this principle to three dimensional point clouds, the SE(3) Transformer represents the system as a graph whose nodes store particle positions and features, while edges encode their geometric relations. Message passing is used to exchange information between particles. To ensure physical consistency, all internal operations must respect the symmetries of SE(3). When the point cloud is rotated or translated, queries, keys, values, and messages must transform in the mathematically correct way. This is achieved by representing features not as ordinary vectors but as tensor fields of different orders, which transform according to the irreducible representations of the rotation group SO(3) [70].
Scalars remain invariant, vectors rotate with the familiar three dimensional rotation matrix, and higher-order tensors transform according to more complex rules. These transformations are described by Wigner D matrices, which ensure that each tensor type behaves consistently under rotations and thus preserves the physical structure of the system.

These matrices represent a rotation in the irreducible representation of degree ℓ and have dimension $D_\ell = (2\ell + 1) \times (2\ell + 1)$. For $\ell = 0$, the representation reduces to the scalar 1, which means that scalar quantities are invariant. For $\ell = 1$, D_ℓ corresponds to the familiar three dimensional rotation matrix that describes the transformation of vectors. For higher values of ℓ, the dimension increases and encodes the transformation of more complex angular dependencies. This representation technique is central to modeling orientation correctly in three dimensional systems. It ensures that higher-order tensor fields transform consistently with the physical structure and is therefore essential for representing orientation dependent geometries. The filters used in message passing follow the construction principles of tensor field networks. They process the relative position between particles by separating it into a learned radial part and a fixed angular part expressed in a basis of spherical harmonics and Clebsch–Gordan matrices. This guarantees that the angular dependence of the filter satisfies the symmetry constraints of the rotation group. When tensor features of different orders interact, their combination is governed by Clebsch–Gordan coefficients, which specify how tensor fields may couple without violating equivariance. The SE(3) Transformer therefore integrates attention, message passing, and representation theory into a single architecture whose internal structure naturally aligns with the symmetries of physical space.

Advantages and Application

In Publication III [71] (see Chapter 4), a specialized form of a SE(3) Transformer is used as the local backbone of PlasmaCrystalNet. The SE(3) Transformer provides a theoretically robust and fully equivariant framework for processing three dimensional particle clouds. However, in the context of plasma crystals the local environment of a particle can be described by quantities that are rotationally and translationally invariant, such as distances, coordination statistics, and bond angles [28]. Because these descriptors already encode most of the relevant geometric information without requiring a complete tensorial treatment, the complete tensor algebra of SE(3) is often unnecessary.
For this reason, PlasmaCrystalNet uses the Crystal Edge Graph Attention Neural Network (CEGANN) [72], which is a practical special case of an SE(3) architecture.
CEGANN preserves the central idea of learning geometry-aware interactions but avoids the explicit use of irreducible representations, Wigner D matrices, or Clebsch–Gordan coefficients. Instead, it constructs an edge-centric graph in which distances and bond angles serve as the primary geometric descriptors. By construction, these quantities are invariant under rotations and translations. This enables the model to capture the essential structure of a crystal phase while maintaining computational efficiency. In this way, CEGANN naturally aligns with the symmetry principles underlying the SE(3) Transformer, but implements them in a simplified form that is well-suited to plasma crystal analysis.
CEGANN constructs an edge-centric graph in which local geometric information is encoded through distances and bond angles. Both pair distances and angle cosines are expanded in Gaussian bases, producing a continuous and smooth representation of local geometry. The angular features θ_{ijk} and the edge features e_{ij} are then processed through a hierarchical, attention-based message-passing scheme.

The angular convolution follows [72]:

$$\theta_{ijk}^{l+1} = \text{softplus}\Big(\theta_{ijk}^{l} + \alpha_{ijk} \cdot \Big(W_{ijk}^{f}\big(\theta_{ijk}^{l} \oplus e_{ij}^{l} \oplus e_{jk}^{l}\big) + b_{ijk}^{f}\Big)\Big), \tag{1.32}$$

where $\oplus$ denotes a feature concatenation operation. The quantities e_{ij}^{l} and e_{jk}^{l} represent the edge features of layer l associated with the particle pairs (i, j) and (j, k), respectively, while θ_{ijk}^{l} denotes the angular feature of the particle triplet (i, j, k) at layer l. The matrices W_{ijk}^{f} and W_{ijk}^{att} are trainable linear maps that operate on the concatenated feature vectors and compute message updates and attention scores, respectively. Their corresponding bias terms are denoted by b_{ijk}^{f} and b_{ijk}^{att}. The index l refers to the layer in the hierarchical message-passing architecture. The attention coefficient α_{ijk} determines how strongly the angular triplet (i, j, k) contributes to the message passed along edge (i, j)[72]. The angle based attention weights are defined as

$$\alpha_{ijk} = \text{softmax}\big(W_{ijk}^{\text{att}}\big(\theta_{ijk}^{l} \oplus e_{ij}^{l} \oplus e_{jk}^{l}\big) + b_{ijk}^{\text{att}}\big). \tag{1.33}$$

Analogously, each edge is updated in the edge-convolution layer[72]:

$$e_{ij}^{l+1} = \text{softplus}\left(e_{ij}^{l} + \sum_{k \in \mathcal{N}(i)} \text{softplus}\Big(\alpha_{ijk} \cdot \Big(W_{ijk}^{f}\big(\theta_{ijk}^{l} \oplus e_{ij}^{l} \oplus e_{jk}^{l}\big) + b_{ijk}^{f}\Big)\Big)\right). \tag{1.34}$$

A subsequent aggregation step constructs a node-specific representation from all edge- and angle-based messages[72]:

$$e_{i}^{l+1} = \sum_{j \in \mathcal{N}(i)} \text{softplus}(e_{ij}^{l}), \qquad \theta_{i}^{l+1} = \sum_{j \in \mathcal{N}(i)} \text{softplus}\left(\sum_{k \in \mathcal{N}(i)} \text{softplus}(\theta_{ijk}^{l})\right), \tag{1.35}$$

and their concatenation forms the final local feature vector Z_i [72]:

$$Z_i = e_{i}^{l+1} \oplus \theta_{i}^{l+1} \tag{1.36}$$

Thus, CEGANN preserves the functional core of a SE(3) transformer while replacing explicit group-theoretic equivalence with strictly rotation- and translation-invariant input descriptors. This is particularly suitable for the physical arrangement of plasma crystals, as the characteristic distortions, lattice defects, and anisotropies are precisely encoded in the distance and angle statistics of the Wigner-Seitz cells.
As a complement to this local representation, PlasmaCrystalNet includes a global structural signature derived from a Voronoi-based geometric analysis. This signature characterizes the local environment of each particle through quantities that are intrinsically invariant under rotations and translations, including Minkowski structural metrics, anisotropy parameters, and coordination numbers.

To compute this signature, the local Voronoi cell of each particle is first determined [16]. The total surface area A of the cell is given by the sum of the areas of all facets f:

$$A = \sum_{f \in F(i)} A(f). \tag{1.37}$$

Based on this, the Minkowski structure metric (MSM) is calculated following Mickel et al. [28, 38]:

$$q_{lm}^{'} = \sum_{f \in F(i)} \frac{A(f)}{A} Y_{lm}(\theta_f, \phi_f), \qquad q_l^{'} = \sqrt{\frac{4\pi}{2l+1} \sum_{m=-l}^{l} |q_{lm}^{'}|^2}. \tag{1.38}$$

The parameter q_l' is a second-order rotational invariant and is evaluated for $l = 4, 6$, since these bond-orientational invariants introduced by Steinhardt et al. [35] are particularly sensitive to different types of local order. In addition, the third-order rotational invariant w_l' is computed [73]:

$$w_l'(i) = \sum_{\substack{m_1,m_2,m_3 \\ m_1+m_2+m_3=0}} \begin{pmatrix} l & l & l \\ m_1 & m_2 & m_3 \end{pmatrix} \frac{q'_{lm_1}(i)\, q'_{lm_2}(i)\, q'_{lm_3}(i)}{\left(q_l'(i)\right)^3}, \tag{1.39}$$

where the bracket denotes the Wigner $3j$ symbols.
Another component of the signature consists of the six eigenvalues

$$\zeta_1, \ldots, \zeta_6, \tag{1.40}$$

of a fourth-order Minkowski tensor that quantifies anisotropy and shape asymmetry of the Voronoi cell [74]. Additionally, the number of nearest neighbors N is included as a further invariant descriptor. These descriptors capture both isotropic phases (fcc, bcc, hcp) and anisotropic phases (bco, bct, fco), and they remain robust even in the presence of distortions, wakes, and measurement noise. Combined with the local geometry-aware representation learned by CEGANN, the resulting architecture constitutes a powerful and reliable classification framework for complex plasma experiments.

1.4 Scientific Context and Scope of this dissertation

This dissertation presents research combining complex plasma physics and modern data-driven analysis methods. Complex plasmas provide a unique experimental environment in which strongly coupled many-body systems can be studied on the kinetic level, with individual microparticles being directly observable. This characteristic enables detailed investigations of collective ordering phenomena as well as single-particle dynamics under controlled laboratory and microgravity conditions.
A central challenge in the analysis of complex plasmas lies in the reliable extraction of physically meaningful information from large and often noisy image datasets. Experimental constraints such as low signal-to-noise ratios, non-uniform illumination, particle motion during data acquisition, and limited observation times require robust and automated analysis techniques. The goal of this dissertation is therefore to develop, validate, and apply advanced machine learning methods that enable precise, reproducible, and scalable analysis of complex plasma experiments in PK-4.
The scientific contributions of this dissertation focus on three complementary aspects: the precise detection of microparticles, the local classification of crystalline structures in complex plasmas, and the time-resolved identification of isotropic and anisotropic structures under dynamic plasma conditions. Each of these aspects is addressed in one of the publications that form the core of this work.

1.4.1 Publication I

The first study [61], presented in Chapter 2, addresses the challenge of reliable multi particle tracking in images of dense complex plasmas. A precise and robust determination of particle positions is fundamental for all subsequent analyses such as structural classification and the investigation of particle dynamics. Under realistic experimental conditions in the PK-4 experiment, high particle densities, overlapping intensity profiles, varying signal-to-noise ratios, and background fluctuations significantly limit the performance of classical image processing approaches. In particular, the previously used method *trackpy* [62] requires careful manual tuning of several parameters to achieve acceptable detection results. These parameters depend strongly on the experimental conditions and image quality and must be adjusted whenever the experimental conditions change. This dependence renders the method unsuitable for highly dynamic and time-critical environments such as parabolic flight experiments [42, 43]. The aim of this work was therefore to develop a particle detection method that operates robustly without manual parameter adjustment and that can be efficiently deployed under constrained experimental conditions. In this context, convolutional neural networks and specifically the U-Net architecture [60] proved to be well suited, as they allow pixel wise segmentation while preserving spatial accuracy. By training the network exclusively on synthetic data that realistically reproduce the optical properties of the PK-4 experiment, including particle appearance, density, and noise characteristics, the method can be optimally tailored to the experimental configuration without relying on time intensive manual annotation of experimental data.

To ensure applicability in resource limited environments, the classical U-Net architecture was systematically simplified by reducing its depth and number of parameters while maintaining high localization accuracy. Several compact U-Net variants were evaluated and benchmarked against established methods. The final architecture achieves a favorable balance between detection performance and computational efficiency and was further optimized for deployment on embedded hardware platforms such as the NVIDIA Jetson board used during parabolic flights.
The results demonstrate that compact U-Net architectures can achieve particle localization accuracies comparable to full size networks while significantly reducing computational complexity. This makes the approach particularly suitable for real time or near real time analysis in parabolic flight experiments. Overall, the presented method substantially contributes to automating the PK-4 experiment by significantly reducing manual intervention and analysis effort. The method establishes a robust and scalable foundation for automated particle detection and tracking, forming the methodological basis for subsequent structural and dynamical analyses presented in this dissertation.

1.4.2 Publication II

The second study [66], presented in Chapter 3, focuses on the local classification of crystalline structures in complex plasmas using a PointNet [53] based deep learning approach. Building on the particle positions obtained with the U-Net based detection method introduced in the first study, the three dimensional particle positions are reconstructed by stacking consecutive images recorded during a controlled scan of the plasma volume and correlating individual particle tracks across these images. This procedure enables the reconstruction of the full three dimensional particle cloud, which forms the basis for structural analysis. Under suitable plasma conditions, microparticles can self organize into ordered crystalline arrangements such as face centered cubic, body centered cubic, or hexagonal close packed lattices. Reliably identifying these structures in experimental data is essential to understanding the crystallization process, phase behavior, and spatial ordering phenomena in complex plasmas. A well established approach for this task was previously proposed by Dietz et al. [28], who combined several structural descriptors into a fixed feature vector and performed classification using a multilayer perceptron. While this method proved to be comparatively accurate and robust, it relies on handcrafted features and predefined metrics derived from the local particle environment. Given the significant advances in deep learning methods in recent years, the aim of this work was to develop a new approach that avoids the explicit construction of feature vectors and instead operates directly on the three dimensional geometric information of the local particle environment. For this purpose, a point cloud based neural network architecture was required that can naturally process unstructured three dimensional data while remaining invariant with respect to translation, rotation, and scaling. The PointNet [53] architecture fulfills these requirements and was therefore identified as a suitable basis for the proposed method.
In this work, a neural network termed *WignerNet* was developed to classify local crystal structures directly from three dimensional reconstructions of Wigner-Seitz cells.

Instead of relying on order parameters or symmetry detection, the network processes the raw point cloud representation of the local particle environment. This design makes the method robust against noise and uncertainties in particle positions, both of which are unavoidable in experimental data. To ensure generalization and invariance, the model was trained exclusively on artificially generated datasets with controlled noise levels, random rotations, and random scalings.
After validation on synthetic data, the trained network was applied to experimental data obtained from the PK-4 experiment. The results demonstrate that the PointNet based approach achieves high classification accuracy across a wide range of noise conditions and outperforms conventional methods in terms of robustness. This work establishes a scalable and flexible framework for automated structural classification in complex plasmas. It provides a key methodological building block for the comprehensive analysis of three dimensional ordering phenomena.

1.4.3 Publication III

The third study [71], presented in Chapter 4, extends the structural classification of plasma crystals by employing an advanced SE(3)-equivariant [68, 72] graph neural network. While previous studies focused primarily on isotropic crystal structures such as face centered cubic, body centered cubic, and hexagonal close packed lattices, this work explicitly targets the identification of additional anisotropic structures, including face centered orthorhombic, body centered orthorhombic, and body centered tetragonal phases. The inclusion of these structures is motivated by theoretical considerations [29] and earlier experimental observations by Takahashi et al. [32], which indicates that such anisotropic crystal symmetries can form in cylindrical DC discharges as in the PK-4 experiment.
Building on the three dimensional particle reconstructions introduced in the preceding studies, this work further investigates the temporal evolution of crystalline structures under controlled laboratory conditions and extends the analysis to experiments conducted under microgravity during parabolic flight campaigns. Unlike earlier approaches that primarily addressed static or locally resolved structures, this study focuses on the identification of crystalline phases in dynamically evolving plasma environments, where external parameters strongly influence structural order. The proposed method combines SE(3)-equivariant message passing on Voronoi based neighborhood graphs with global, invariant structural descriptors derived from the geometry of Wigner-Seitz cells. The equivariance of the network with respect to three dimensional rotations and translations ensures that classification results are independent of the orientation and absolute position of the particle cloud, which is essential for the analysis of experimental plasma data. In contrast to point cloud based approaches, the graph representation allows for a more direct and efficient encoding of local neighborhood relations and anisotropic distortions of the lattice. The network was trained exclusively on synthetic datasets covering a broad range of noise levels and lattice deformations and was subsequently validated using experimental data from PK-4 under both laboratory and microgravity conditions.

The results demonstrate that the model can accurately classify a wide spectrum of crystalline symmetries, including isotropic and anisotropic structures. The model significantly outperforms previous machine learning approaches in noisy and dynamic environments. Time-resolved analyses indicate that crystal formation and stability depend strongly on external control parameters, such as gas pressure and polarity switching frequency. Crystalline phases are observed less frequently in microgravity and are often replaced by anisotropic or chain-like arrangements. This highlights the critical role of particle confinement and compression.
Overall, this study demonstrates the effectiveness of symmetry-aware graph neural networks in analyzing complex, time-dependent, many-particle systems. The study expands the range of detectable crystal structures in complex plasmas and offers a robust framework for investigating phase behavior and structural transitions under laboratory and microgravity conditions.

1.4.4 Summary

The three architectures presented in this chapter reflect a systematic methodological progression from pixel-level detection (U-Net), to local geometric classification of reconstructed point clouds (WignerNet), and finally to symmetry-aware graph representations capable of capturing anisotropic and isotropic phases (PlasmaCrystalNet). Table 1.2 summarizes their essential properties.

Architecture	**Data Type**	**Key Property**	**Role in This Work**
U-Net	2D images	Local feature extraction and pixel-level segmentation	Detection and localization of particles in PK-4 recordings
WignerNet	3D point clouds	Permutation-invariant processing and direct structural descriptors	Classification of local crystal structures via Wigner–Seitz cells
PlasmaCrystalNet	Graphs + global signature	Rotational and translational invariance; consistent local and global geometric features	Robust structural analysis under realistic PK-4 conditions, including anisotropic phases

Table 1.2: Compact overview of the model architectures used in this work.

Combined, these models illustrate a conceptual transition from image-based to structure-based representations. They show how modern deep learning architectures are increasingly integrating physical invariants directly into their model design, enabling reliable analysis even under complex experimental conditions.

Chapter 2

Publication I: Multi-Particle Tracking in Complex Plasmas Using a Simplified and Compact U-Net

Author Contributions

Niklas Dormagen

Conceptualization (lead)
Software (lead)
Data curation (lead), Investigation (lead), Validation (lead) and Visualization (lead)
Writing – original draft and revision

Max Klein

Data curation (supporting) and Software (supporting)
Writing – review and editing (supporting)

Andreas S. Schmitz

Data curation (supporting)
Writing – review and editing (supporting)

Markus H. Thoma and Mike Schwarz

Funding acquisition (lead)
Project administration (lead)
Writing – review and editing (supporting)

Journal of *Imaging*

MDPI

Article

Multi-Particle Tracking in Complex Plasmas Using a Simplified and Compact U-Net

Niklas Dormagen [1,2,*], Max Klein [1,2], Andreas S. Schmitz [2], Markus H. Thoma [2] and Mike Schwarz [1]

[1] NanoP, TH Mittelhessen University of Applied Sciences, D 35392 Giessen, Germany; max.klein@ei.thm.de (M.K.); mike.schwarz@ei.thm.de (M.S.)
[2] I. Physikalisches Institut, Justus Liebig Universitat Giessen, D 35392 Giessen, Germany; andreas.s.schmitz@physik.uni-giessen.de (A.S.S.)
* Correspondence: niklas.dormagen@nanop.thm.de

Abstract: Detecting micron-sized particles is an essential task for the analysis of complex plasmas because a large part of the analysis is based on the initially detected positions of the particles. Accordingly, high accuracy in particle detection is desirable. Previous studies have shown that machine learning algorithms have made great progress and outperformed classical approaches. This work presents an approach for tracking micron-sized particles in a dense cloud of particles in a dusty plasma at Plasmakristall-Experiment 4 using a U-Net. The U-net is a convolutional network architecture for the fast and precise segmentation of images that was developed at the Computer Science Department of the University of Freiburg. The U-Net architecture, with its intricate design and skip connections, has been a powerhouse in achieving precise object delineation. However, as experiments are to be conducted in resource-constrained environments, such as parabolic flights, preferably with real-time applications, there is growing interest in exploring less complex U-net architectures that balance efficiency and effectiveness. We compare the full-size neural network, three optimized neural networks, the well-known StarDist and trackpy, in terms of accuracy in artificial data analysis. Finally, we determine which of the compact U-net architectures provides the best balance between efficiency and effectiveness. We also apply the full-size neural network and the the most effective compact network to the data of the PK-4 experiment. The experimental data were generated under laboratory conditions.

Keywords: dusty plasma; image analysis; neural networks; U-Net; paricle tracking

Citation: Dormagen, N.; Klein, M.; Schmitz, A.S.; Thoma, M.H.; Schwarz, M. Multi-Particle Tracking in Complex Plasmas Using a Simplified and Compact U-Net. *J. Imaging* **2024**, *10*, 40. https://doi.org/10.3390/jimaging10020040

Academic Editor: Raimondo Schettini

Received: 25 October 2023
Revised: 12 January 2024
Accepted: 15 January 2024
Published: 31 January 2024

1. Introduction

Fundamentally, plasmas are ionized gases where electrons can move freely within the gas [1]. The density of positive and negative charge carriers in plasmas is approximately equal. When particles are introduced into a low-temperature and low-pressure discharge plasma, it is termed as a dusty or complex plasma. These plasmas, in addition to electrons, ions, and neutral gas atoms, also include micron-sized particles [1]. The high mobility of electrons in low-temperature plasma leads to the negative charging of micro-particles. They collect charged plasma particles. The structures and dynamics of large micro-particle systems, containing up to 10^6 particles, can be easily observed with laser illumination due to the significant interparticle distance, typically exceeding 100 µm [1,2]. This creates a dilute and transparent particle system that can be effectively analyzed using cameras. The PK-4 experiment ("Plasmakristallexperiment 4") is designed specifically to investigate complex plasma in a DC discharge that occurs in an elongated glass tube. A detailed description of PK-4 can be found in the reference [3]. This work is an extension of previous work [4] originally reported in the 30th International Conference on Mixed Design of Integrated Circuits and Systems—MIXDES 2023. To analyze particle behavior in the plasma, their positions must first be determined. Since each image contains several particles, the method should be able to track multiple particles in one image.

Approaches to particle detection ranged from local-maxima finding to linear filtering, linear and nonlinear model fitting, and centroid estimation schemes [5]. In the previously employed method, image preparation involves utilizing a bandpass and a threshold value. The selection of an optimal threshold is crucial for images containing features (particles) and background (noise) in image processing [6]. An optimal threshold is crucial, as emphasized in studies like Sezgin and Sankur [7]. Given the fundamental focus of Mohr et al. (2019)'s work on complex plasmas [6], we chose to employ Otsu's method [8] as a thresholding technique in line with their research. While other thresholding techniques are available (for an overview, see, e.g., Sezgin and Sankur [7]), our choice aligns with the approach and findings of D. Mohr et al. (2019) [6]. Their findings demonstrated that most alternative techniques often result in inaccurate binarizations. Background pixels are mistakenly identified as signals and set to white. For more details, refer to D. Mohr et al. (2019) [6]). If a particle spans multiple pixels in an image, we can determine its position with sub-pixel accuracy by calculating the weighted average position of these pixels [9]. The point determined in this manner is termed the center of mass, representing the position of a particle. The method was developed based on the open-source library "trackpy" [9]. Recently, data-driven alternatives employing deep learning have significantly enhanced quantitative digital microscopy, offering the potential for accurate and rapid image analysis. Midtvedt et al. (2021) [10] have developed a dedicated tool for particle localization, tracking, and characterization, extending to cell counting and classification. In another study, Midtvedt et al. (2022) [11] concentrated on object recognition in the realm of digital microscopy, where machine learning has made substantial progress in overcoming the limitations of classical approaches. Notably, the U-net architecture was employed. Furthermore, Huang et al. (2019) [12] have successfully applied machine learning approaches to image-based analyses of complex plasmas. These insights are intended for enhancing particle localization in complex plasmas. This work focuses on a multi-particle tracking approach using a U-net. The U-net is a convolutional network architecture designed for rapid and precise image segmentation, developed at the Computer Science Department of the University of Freiburg [13]. However, as experiments are slated for resource-constrained environments, such as parabolic flights, with a preference for real-time applications, there is a growing interest in exploring less complex U-net architectures that strike a balance between efficiency and effectiveness. Considering the limited resources, the U-net [4] presented in previous work is now slated for optimization. The primary strategy is to reduce the depth of the U-net to optimize the architecture, considering FLOPS and MACCs. A smaller number of layers results in fewer parameters and, consequently, a reduced computational load. We will design three different compact architectures. Subsequently, we will determine which of the compact U-net architectures provides the best balance between efficiency and effectiveness. Next, we will compare the full-size neural network, the optimized neural network, a well-known neural network called StarDist [14], and trackpy [9] in terms of accuracy in analyzing artificial data. StarDist is a neural network architecture designed for image segmentation tasks, particularly applied to instances where objects exhibit star-shaped structures. Developed by Schmidt et al. in 2018 [14], StarDist employs a U-net-based architecture and is trained specifically for object detection in microscopy images. It utilizes a polygonal representation of object shapes, making it well-suited for applications like cell nucleus segmentation [14]. For these analyses to be meaningful, the methods should accurately detect particle positions. We also apply the two U-net architectures to experimental data.

2. Experiment

The Plasmakristall 4 experiment is characterized by the fact that the plasma is ignited by a direct current discharge. This makes it possible to study complex plasmas in different plasma environments [3].

A model of PK-4 has been on the International Space Station since late 2014. The details are described in ref. [3]. We will briefly outline the important components. The plasma chamber is an elongated U-shaped glass tube with a total length of 86 cm and a diameter of 3 cm. Two cameras are available for the observation of the micron-sized particles, which can be moved in longitudinal and in radial direction of the plasma chamber (x- and y-direction in Figure 1). At the ends of the glass tube, the high-voltage electrodes are mounted. The high-voltage power supply operates in DC or AC mode (polarity switching) with a frequency up to 5 kHz. The DC current can be adjusted between 0.5 and 3 mA. The electric field strength of the longitudinal DC field in the positive column of the discharge was measured using Langmuir probes on the ground, in the absence of micro-particles, to be about 2 V/cm, nearly independent of the DC current [3]. The gas, usually neon or argon with pressures between 10 and 200 Pa, is filled in by gas flow up to 10 sccm through the cylindrical electrode and can be pumped out through the other cylindrical electrode by a turbo molecular pump [2]. After igniting the plasma, the micro-particles are injected from the dispensers through ports at the side legs of the glass tube. The Particle Observation laser is used to illuminate the particles whose scattered light can be detected by the cameras. The laser emits green light with a wavelength of 532 nm and has an output power of up to 240 mW [3]. The light from the laser is fanned out to illuminate a plane perpendicular to the z-direction [3]. The scattered light from the micro-particles is recorded by a CCD camera (2 Megapixel, 35 frames per second [fps] at full resolution) and a CMOS camera with a larger field of view and a higher frame rate and resolution (xiQ MQ042MG-CM, 4 Megapixel, 90 fps at full resolution, 1 pixel corresponds to 11.4 µm) [2]. They can scan the tube 20 cm in the horizontal direction as well as 3 cm perpendicular to it. The DC mode can be used to trap and stop the micro-particles (Figure 2).

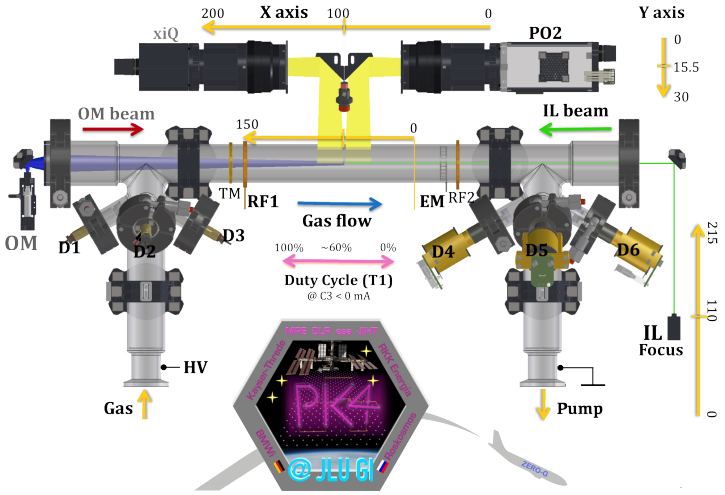

Figure 1. Schematic of the PK-4 plasma chamber provided by the Thoma research group of the JLU Gießen.

To study the particles in microgravity, experiments can be performed either on board the ISS or during parabolic flights. The I. Physikalisches Institut of the Justus-Liebig-Universität (JLU) in Gießen focuses on laboratory investigations of complex plasmas and plans/tests experiments for the ISS using the PK-4 experiment. For this purpose, the JLU has an identical model known as the Science Reference Model (SRM). This is used to plan experiments and largely automate processes. In addition, experiments are also performed with a parabolic flight model of the PK-4 in parabolic flight. This is almost identical to the SRM, but can be modified for more advanced experiments, which is not possible with the SRM. For example, other particle types can be used, or components such as cameras can be modernized. Various parabolic flight experiments have been conducted in the past with the support of the German Aerospace Center (DLR).

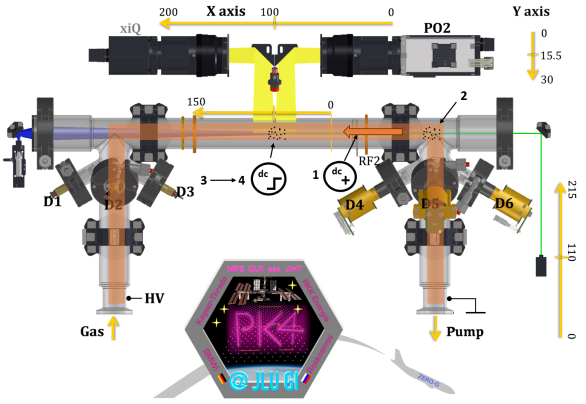

Figure 2. Schematic representation of DC trapping procedure. Steps: 1—ignition of the DC plasma, 2—microparticle injection, 3—microparticles arrival into the PO camera field of view, and 4—the discharge in the polarity-switching mode. The graphic was created based on the work of Pustylnik et al. [3].

For the parabolic flights, the aircraft A310 ZERO-G of the company Novespace is used. Microgravity with a duration of about 22 s per parabola will be realized on three flight days in 31 parabolas each. The parabolic flight model consists of two racks (Figure 3a), one containing an integrated base plate (Figure 3b), another one containing the computers for experiment control and recording. The integrated base plate was used as the engineering model for the ISS project and is to a large content identical with the one of the flight model [2]. The micron-sized particles were injected into the plasma at the beginning of the microgravity phase of a parabola, which then move into the field of view of the cameras. Once the particles arrive into the field of view, the DC discharge is switched to the polarity-switching mode with a duty cycle of $\delta = 0.5$ [3]. After this, the micro-particles experience zero net force and are trapped [3]. Once the particles are trapped, they will be observed and photographed by the cameras. In order to perform further analyses on the plasma, the positions of the particles in the plasma have to be determined from the images. Conventional methods were used for this purpose in previous investigations. In the following, a machine learning approach will be investigated, which could potentially replace the conventional method in future investigations.

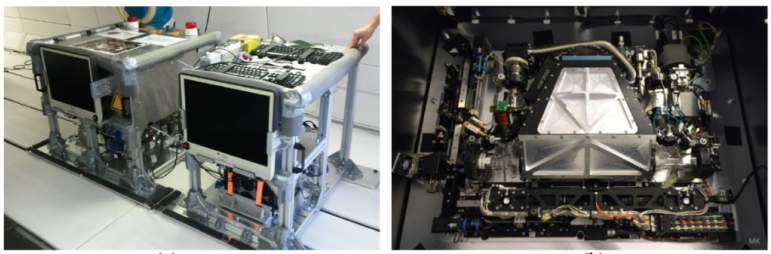

(a) (b)

Figure 3. (**a**) The PK-4 parabolic flight experiment unit in the aircraft A310 Zero-G. (**b**) The integrated base plate accommodated in the left rack [2].

3. U-Net Architecture

Developed by Olaf Ronneberger, Philipp Fischer, and Thomas Brox in 2015 [13], the U-Net represents a special neural network, which is primarily designed for image segmentation tasks. It excels at partitioning an image into multiple segments or regions of interest, making it particularly suitable for tasks where precise delineation of objects or structures in images is required, such as medical image segmentation or semantic segmentation in computer vision. The U-Net architecture has a U-shaped structure with a contracting path (encoder) and an expansive path (decoder) (see Figure 4). It incorporates

skip connections that preserve spatial information and allow the network to perform accurate segmentation. It has a specific focus on spatial preservation and the precise localization of objects.

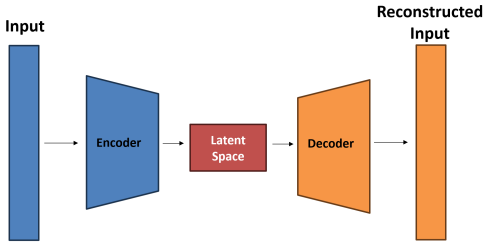

Figure 4. Schematic representation of an U-Net architecture.

The encoder is the initial part of the U-Net. It takes the input data and maps it to a lower-dimensional representation, the so called latent space. The encoder accomplishes this through a series of layers, where each layer performs mathematical transformations on the input data. These transformations pack the information step by step into a more compressed format. The U-Net's latent space is often called the "middle layer" or "bottleneck". While it does capture abstract representations of the input image, its primary purpose is to facilitate segmentation rather than feature extraction or dimensionality reduction. The expansive path, also known as the decoder, aims to generate a high-resolution segmentation map from the feature representations obtained in the contracting path. Unlike traditional CNN architectures, the U-Net employs a series of up-convolutions (transposed convolutions or deconvolutions) to upsample the feature maps. Moreover, the expansive path incorporates skip connections that concatenate feature maps from the contracting path. These skip connections enable the U-Net to preserve fine-grained spatial information and are essential for accurate segmentation. The U-Net's output is segmentation masks, where each bright pixel in the mask can be assigned to a particle position.

3.1. Simplifying the Architecture

The traditional U-Net architecture, celebrated for its outstanding accuracy and fine-grained segmentation through contracting and expansive paths connected by skip connections, is depicted in Figure 5. This U-Net comprises numerous layers, encompassing a total of 389,521 parameters. However, this intricate structure poses a computational challenge, especially in resource-constrained settings like parabolic flights. Consequently, there is an increasing demand for models that can provide precise results without sacrificing speed or resource efficiency. Less complex U-Net architectures aim to fulfill this demand by simplifying the original design while preserving essential features for effective segmentation.

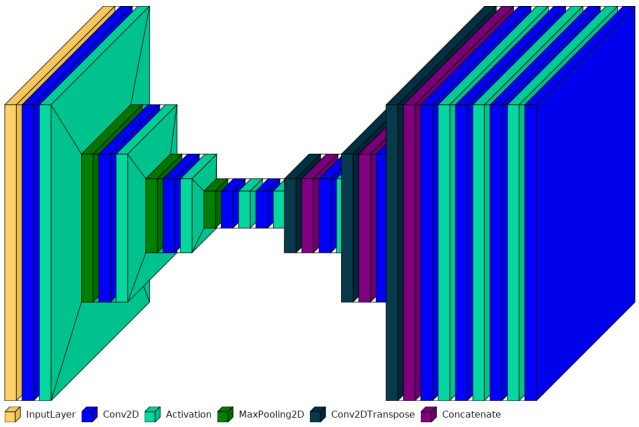

Figure 5. Structure of the U-Net architecture.

The key approach involves diminishing the depth of the U-Net. A reduced number of layers leads to fewer parameters, thereby decreasing computational demands. This modification proves especially beneficial for tasks where a shallower architecture remains capable of capturing essential features. Using lightweight convolutional blocks serves to substantially streamline the model's complexity while preserving satisfactory segmentation quality. Diligent reduction in the number of skip connections contributes to simplifying the architecture. However, this adjustment should be executed with caution to guarantee the retention of pertinent contextual information. In accordance with this strategy, three distinct architectures were devised.

3.1.1. Simplified U-Net 0

The contracting path is comprised of two convolutional layers, followes by a max-pooling layer. The initial convolutional layer has 16 filters and utilizes the ReLU activation function, with padding set to 'same' to preserve spatial dimensions. The second convolutional layer mirrors the first, effectively doubling the number of feature maps. Max-pooling layers, with a pool size of 2×2, halve the spatial dimensions. The bottleneck involves two convolutional layers, each with 32 filters, followed by the ReLU activation function. This step condenses information into a latent representation. On the expansive path, the feature maps undergo upsampling and are concatenated with feature maps from the contracting path. In contrast to the original architecture, we replaced transposition operations (Conv2DTranspose, see Figure 5) with upsampling operations (UpSampling2D, see Figure A1) to enhance the network's efficiency. Transposition operations combine trainable upsampling and convolution, providing flexibility but potentially incurring higher computational costs. On the other hand, upsampling operations perform fixed upsampling without trainable parameters, making them more efficient albeit less adaptable.

Following each upsampling layer, two convolutional layers with 16 filters and ReLU activation are applied. Concatenation merges the upsampled feature maps with the corresponding feature maps from the contracting path. This skip connection is instrumental in enabling the network to recover spatial details. Consequently, we managed to reduce the architecture to a size of 25,633 parameters (see Figure A1).

3.1.2. Simplified U-Net 1

In our case, the task is relatively straightforward, requiring the model to capture a more limited range of complex features. Therefore, we make use of the simplified U-Net 0 architecture once again, maintaining a constant number of eight filters for each layer. The ReLU activation function is used for each layer, and padding is set to 'same' to preserve spatial dimensions. Following each convolutional layer, an identical convolutional layer is added, effectively doubling the number of feature maps. Max-pooling layers with a pool size of 2×2 reduce the spatial dimensions by half. The bottleneck consists of two convolutional layers with eight filters each, followed by ReLU activation functions. The expansive path involves upsampling the feature maps and concatenating them with feature maps from the contracting path. After each upsampling layer, two convolutional layers with eight filters and ReLU activation are applied. Concatenation combines the upsampled feature maps with the corresponding feature maps from the contracting path. This network, designed in this manner, consists of 6481 parameters (see Figure A2).

3.1.3. Simplified U-Net 2

The next network is designed with increased depth. In analogy to the simplified U-Net 1, the number of filters remains constant. The contracting path comprises three convolutional segments, each followed by a max-pooling layer with a pool size of 2×2. Each convolutional segment consists of two identical convolution layers with eight filters activated by the ReLU activation function. Padding is set to 'same'. The bottleneck comprises two convolutional layers with eight filters each, followed by ReLU activation functions, compressing the information into a latent representation. The expansive path

consists of three upsampling segments, each comprising an upsampling layer followed by two identical convolutional layers. Concatenation combines the upsampled feature maps with the corresponding feature maps from the contracting path. The network designed in this way consists of 9409 parameters (see Figures 6 and A3).

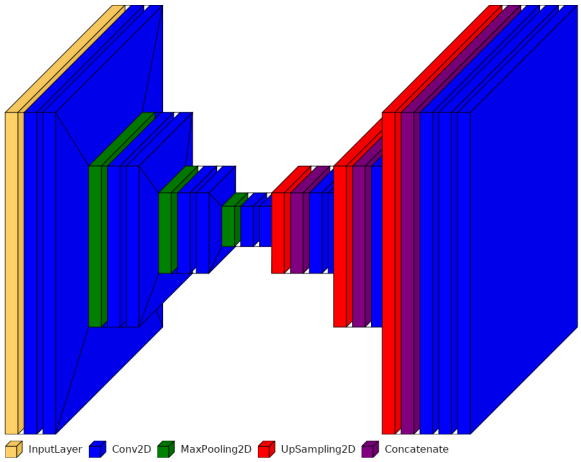

Figure 6. Structure of the simplified and more compact U-Net architecture.

4. Network Training Details

The U-Nets can undergo training to classify predetermined patterns using labeled training data, a process known as supervised learning. However, in the case of experimentally collected data on complex plasmas, which may consist of multiple phases, applying labels to train the networks is impractical. Therefore, the networks need to be trained with artificial data. During training, the predictions of each input are compared with their labels, and the weights are readjusted accordingly. With each iteration of this process, the accuracy of the neural network improves. An often encountered challenge is the phenomenon known as "overfitting". In a specific example, a U-Net model is trained to transform the input into a binarized representation. In this representation, each pixel within 4.5 pixels of a particle in the input is set to 1, while every other pixel is set to 0. According to [15], the network is compiled using binary cross-entropy. Cross entropy is a mathematical concept used to measure the dissimilarity or "distance" between two probability distributions, often representing predicted and true data. In this context, it assesses how well the model's predictions align with the true labels. Binary cross entropy is a specific form of cross entropy designed for binary classification tasks, where there are only two possible outcomes, typically denoted as classes 1 and 0.

Replicating the optical properties of the PK-4 experiment, the appearance of a particle is simulated using the open source package "deeptrack" [10]. The training set consists of synthetic images with dimensions of 512 $\times$ 512 pixels. Each image includes a minimum of 40 and a maximum of 350 particles. The particles are simulated as point scatterers, and their positions in the camera plane adhere to a normal distribution. The standard deviation for this distribution is set to 5 pixel units along the axis normal to the camera plane. Each particle is imaged using a fluorescence microscope with numerical aperture NA between 0.6 and 0.8 and illuminating laser wavelength of 532 nm. The noise is simulated as poisson noise with an signal to noise ratio in the range of 5 to a maximum of 200. Here, the range of noise is in line with the well-known Rose criterion (Rose [16] (p. 97)), which states that a signal-to-noise ratio of at least 5 is required for reliable detection [6].

Poisson noise is a basic form of uncertainty associated with the measurement of light, inherent to the quantized nature of light and the independence of photon detections. To enhance the training of the U-Net architecture, data augmentation is a powerful technique. Applying various transformations to the existing training dataset, data augmentation is used to create additional synthetic training examples. These transformations maintain the

semantic content of the data while introducing diversity through variations in factors like rotation, scaling, translation, and noise. The key idea is to expose the model to a broader range of input variations, making it more robust and better at generalizing to unseen data. The image is finally normalized by rescaling it to be contained between two random numbers within (0, 1).

During training, we employ learning rate scheduling. In deep learning, using a fixed learning rate can result in divergence or slow convergence. Learning rate scheduling enables the adjustment of the learning rate throughout the training process. We initiate training with an initial learning rate of 0.001 and decrease it to 0.0001 after the first 5 epochs. This approach is designed to facilitate faster convergence in the initial training phases with a higher learning rate, while a lower learning rate later on aids in fine-tuning and stabilizing the model's performance, bringing it closer to the optimal solution. The validation set consists of 100 images. After 100 epochs, the network achieves approximately 98% accuracy in analyzing test data.

5. Results on Artificial Data

To compare the U-Net architectures with trackpy and StarDist, we generated artificial data with a signal-to-noise ratio ranging from 5 to 200 (see Figure 7). Initially, we assess the analysis time required by the methods. We compare the time needed for datasets of various sizes, which include 256 × 256 images. Additionally, we evaluate the analysis time for images of different dimensions, such as 64 × 64, 128 × 128, 256 × 256, 512 × 512, and 1024 × 1024 pixels. It turned out that the analysis based on StarDist takes about ten times longer than using the other methods. To keep the graph clear, StarDist is not listed in Figure 8.

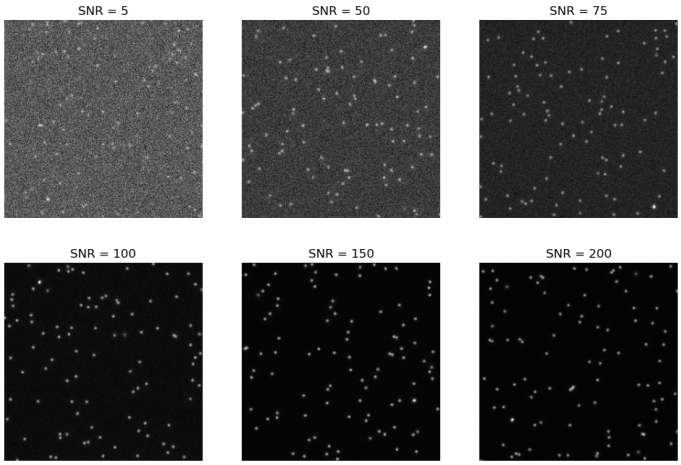

Figure 7. Extract of the train data. Artificial 512 × 512 pixel images, with different signal to noise ratios.

Examining Figure 8, it becomes evident that the larger the dataset, the more distinct the differences in analysis times. The simplified U-Net architectures consistently exhibit the shortest analysis times, with **simplified U-Net 1** and **simplified U-Net 2** standing out. On average, analyses based on these architectures take almost half the time compared to other methods. When considering the image format, trackpy demonstrates faster performance for small images, while the U-Net architectures become more efficient as the image format increases. This suggests that operations directly applied to the image are faster for small formats, while creating masks and subsequent detection become more efficient for larger images. The computational complexity of the architectures directly influences their running speed, commonly measured by the floating-point operand FLOPs [17]. To compare the U-Net architectures, the FLOPs indicator is utilized (refer to Figure 9). FLOPs are calculated for each layer, such as convolution layers, following a specific formula:

$$FLOPs = 2HW(C_{in}K^2 + 1)C_{Out}, \quad (1)$$

where H = height, W = width, C_{in} = number of channels of the input feature map, K = kernel size and C_{Out} = number of output channels [17].

The FLOPs do not depend directly on the number of parameters. Networks with the same number of parameters can have a different number of FLOPs due to different network depth or width.

In addition, we compare the architectures using the improved indicator multiply-accumulate operations (MACCs) (see Figure 9). For a conv layer with kernel size K, the number of MACCs is:

$$MACC = K^2 \cdot C_{in} \cdot H_{Out} \cdot W_{Out} \cdot C_{Out}, \tag{2}$$

where K = kernel size, C_{in} = number of channels of the input feature map, H_{Out} = height of the output, W_{Out} = width of the output and C_{Out} = number of output channels [17].

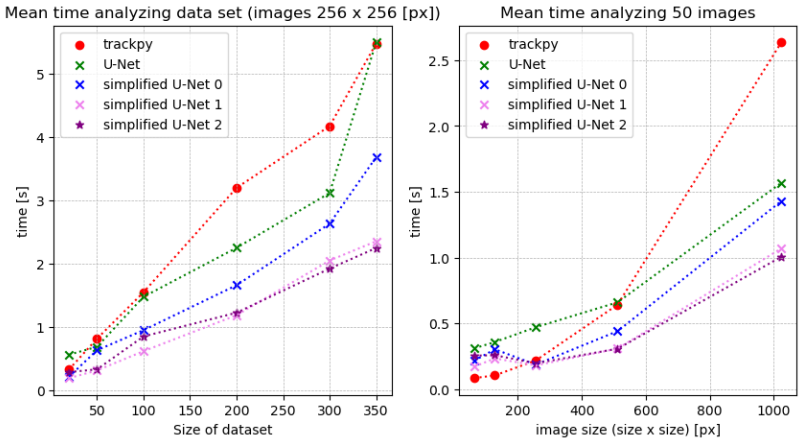

Figure 8. Time analyzing data sets of different sizes or image sizes at given noise level of 100.

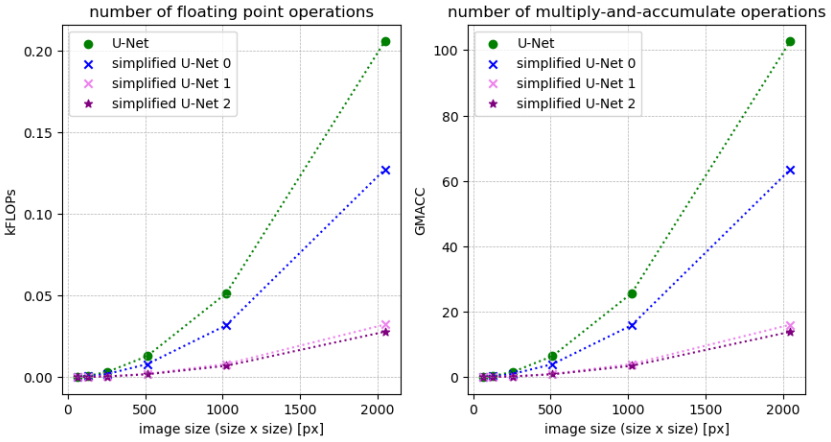

Figure 9. Statistical indicators for computational complexity.

Observing Figure 9, the simplified U-Net 1 and 2 stand out prominently. In direct comparison, these architectures remain remarkably compact, even with large input images. For images sized 2048 × 2048 pixels, the number of FLOPs is approximately one-fifth of the FLOPs of the full-size U-Net. Similarly, the number of MACCs is only one-tenth of the MACCs of the original U-Net. Consequently, these architectures are significantly less complex than the full-size model. Beyond the compactness of the architectures, their accuracy is pivotal in the analysis. Therefore, the average percentage of correctly detected particles at a given noise level is compared, considering the number N of incorrectly

detected particles. Predicted particles are considered correct only if their deviation from the actual position is within 5% of the particle diameter.

Figure 10 shows that trackpy [9] detects more particles at higher noise levels compared to neural networks. However, assessing the mean number N of incorrectly detected particles reveals the method's relative inaccuracy and tendency to detect particles somewhat randomly. In strong noise conditions, the full-size **U-Net** performs well, with few misdetected particles, identifying approximately 87% of the sought particles. The simplified U-Net architectures are less accurate in significant noise. Specifically, simplified U-Net 2 behaves similarly to trackpy, with an increase in misclassifications as image noise rises. Starting from a signal-to-noise ratio greater than 50, the **simplified U-Net 0** detects particles as reliably as the full-size U-Net, with fewer false detections as noise decreases. For all methods, fewer particles are falsely detected as the noise decreases. While the number of false detections for the **simplified U-Net 1**, starting from a signal-to-noise ratio of 50, is almost identical to the number for the full-size **U-Net**, the count of correctly detected particles is slightly lower than that for the full-size **U-Net** and the **simplified U-Net 0**. Performance differences may stem from the varying complexity of these model architectures, enabling more complex ones to robustly segment and detect particles compared to simpler architectures. Notably, the **simplified U-Net 2** demonstrates commendable results, suggesting an optimal balance between efficiency and effectiveness. This is particularly relevant as data from parabolic flight campaigns typically have a signal-to-noise ratio of around 100. In contrast, the StarDist [14] model seems less suitable for detecting particles in a complex plasma. Despite having the fewest misclassifications, it only detects around half of the sought-after particles, even with a high signal-to-noise ratio (SNR). Trackpy, on the other hand, exhibits a lower percentage of correctly detected particles as noise decreases compared to the U-Net architectures, although its mean misdetected particles count is significantly lower. The observed performance differences could be attributed to the varying adaptability of the methods to changing conditions, particularly in terms of subpixel accuracy. The potential improvement in accuracy for trackpy might be achieved through adaptation to changing conditions. On the other hand, neural networks appear to work more independently in this regard, despite exhibiting a higher count of misclassified particles, especially with lower noise levels.

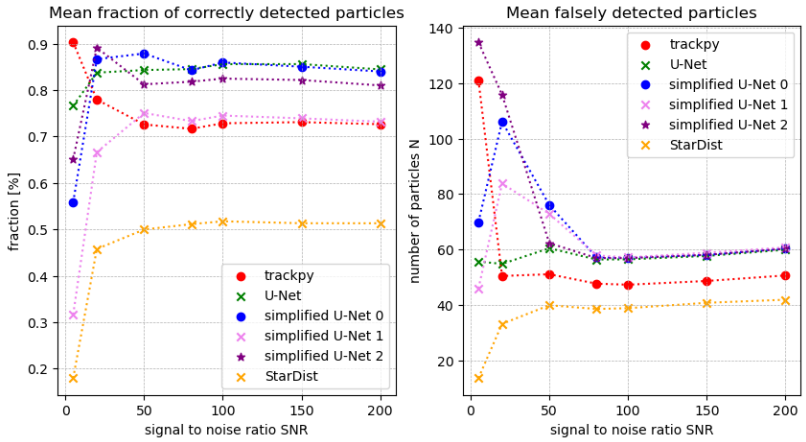

Figure 10. Prediction of the methods at a given noise level, taking into account misclassifications.

To enhance the accuracy of neural networks, more extensive training with a diverse set of training data, including variations in signal-to-noise ratio and background noise, could be beneficial. This approach may lead to improved generalization and robustness of the networks across different conditions. An illustrative comparison of predictions between the full-size U-Net and the simplified U-Net 2 is presented in Figure 11. The visualization clearly demonstrates that certain particles are detected by the U-Net but missed by the

simplified U-Net 2, and vice versa. However, with a few exceptions, it can be concluded that the two networks generally yield quite similar results.

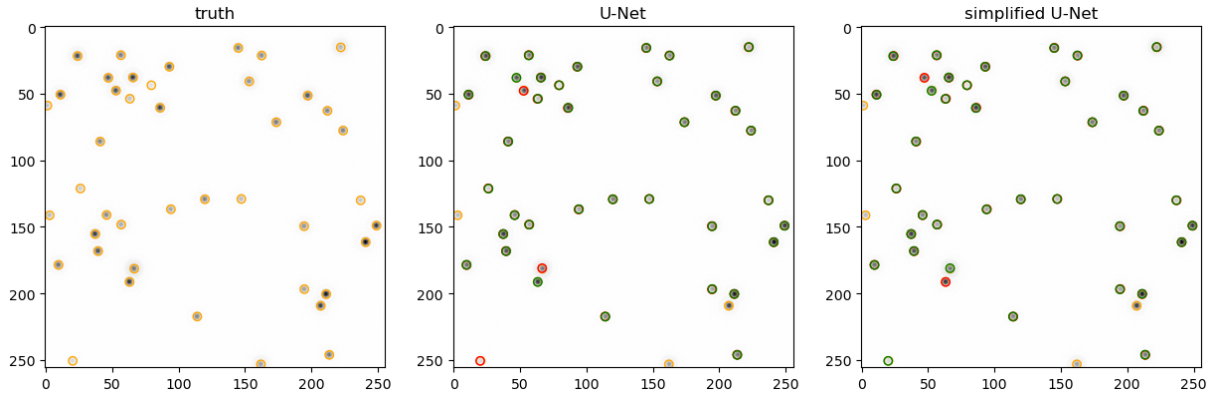

Figure 11. Prediction of both U-net architectures for an extract of the artificial data, where the particles marked in green were detected correctly, and the particles marked in orange were not detected. The particles marked in red show the difference between the two networks. The image shown above has been cropped and inverted for illustration.

6. Using the Trained Network on Experimental Data

The image data of the particles were recorded during a parabolic flight campaign by Justus Liebig University in the A310 ZERO-G aircraft of Novespace (for more details see Section 2).

As this is a measurement, there are no truth data available that can be used to verify the results. The experimental data are comparatively less noisy with respect to Poisson noise. Accordingly, the simplified U-Net should also produce resilient and solid results. A look at Figure 12 shows that the images taken during parabolic flight campaigns contain a large amount of position data, which further emphasizes the need for the most efficient architecture possible. At first glance, it seems that the two U-Net architectures provide approximately similar results. On the one hand, the simplified network detects 91% of the particles that the fullsize network also detects. On the other hand, 19% of the particles detected by the simplified network are not detected by the full-size net. On closer inspection, it is noticeable that both neural networks seem to detect particles in places where apparently none should be found (see Figure 13). These ghost particles seem to occur mainly in the edge region. This may lead to inaccurate and inconclusive analyses afterwards. This problem can probably be solved with more extensive training data, which are more similar to the parabolic flight data.

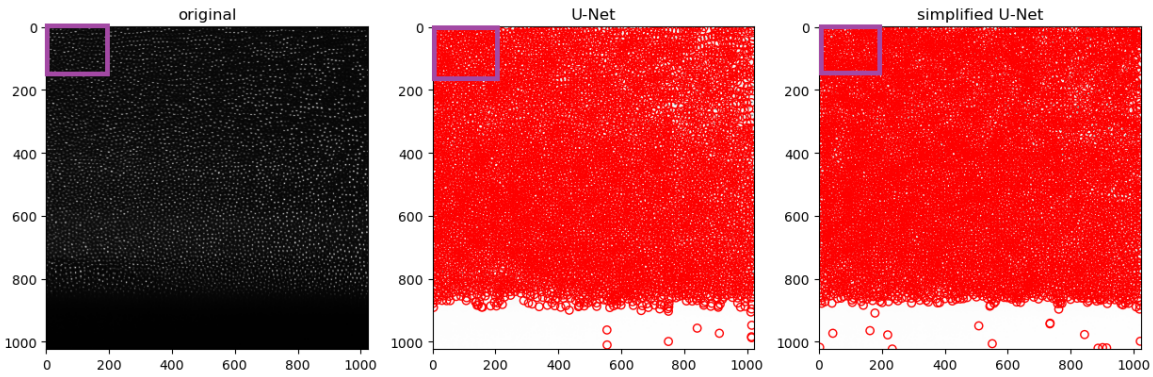

Figure 12. Prediction of both U-Nets for an extract of the experimental data. The image shown above should be cropped for illustration (purple rectangle).

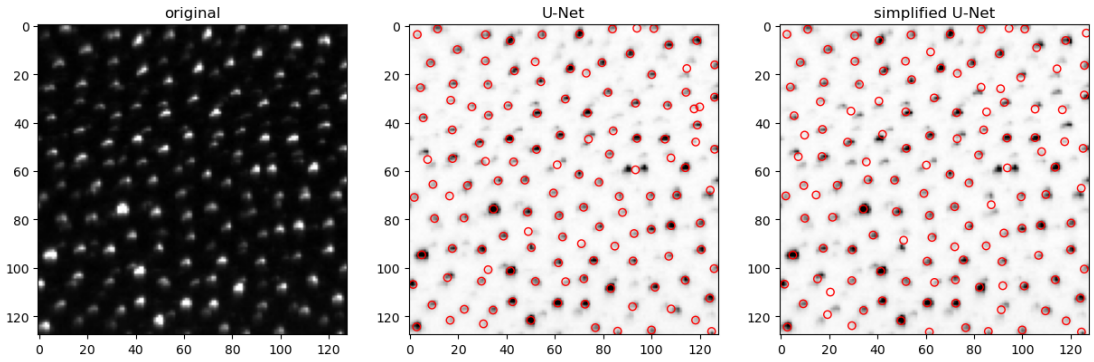

Figure 13. Prediction of both U-Nets for an extract of the experimental data. The image shown above has been cropped for illustration.

7. Conclusions

We presented an efficient and compact U-Net version for detecting multiple particles in complex plasmas. The results also demonstrated that the compact neural network is relatively accurate, especially in low-noise data. Furthermore, the compact network exhibits relatively fast performance with large datasets or larger-format images. It is worth emphasizing that the compact U-Net is suitable for small single-board computers with limited resources due to its low runtime and memory requirements. Accordingly, there are possible applications for future parabolic flight campaigns to perform initial analyses during flight. Compared directly to U-Net architectures, trackpy appears to be constrained by the system's complexity. The method must be repeatedly adapted to the different noise levels in order to achieve reliable results. Essentially, the method's parameters are crucial for the analysis accuracy, making them a potential source of error. Accordingly, the settings are a potentially large source of error. On the one hand, the development with deep learning has shown that these limitations can be largely overcome. A major advantage of the machine learning approach for particle tracking is that simulated data can often be used to train the networks. In addition, no presettings have to be made. Thus, the trained networks can be used universally. However, the networks detected ghost particles in the experimental data, potentially leading to inaccurate follow-up analyses. This issue should be considered in future developments, and efforts should be made to correct the error.

In view of further developments, the network could be evolved, corresponding to recent studies [11,15,18], to trace the particles and reconstruct their three-dimensional positions or analyze potential string formations [19].

Author Contributions: Conceptualization, N.D. and M.K.; methodology, N.D.; software, N.D.; validation, N.D.; formal analysis, N.D.; investigation, N.D. and M.K.; data curation, N.D., A.S.S. and M.H.T.; writing—original draft preparation, N.D.; writing—review and editing, N.D., M.K., A.S.S., M.H.T. and M.S.; visualization, N.D.; supervision, N.D.; project administration, M.H.T. and M.S.; funding acquisition, M.H.T. and M.S. All authors have read and agreed to the published version of the manuscript.

Funding: This project was funded by the German Federal Ministry of Economic Affairs and Climate Action under contract No. 50WK2270B.

Data Availability Statement: The data presented in this study are available on request from the author.

Acknowledgments: This work is supported by the German Aerospace Agency (DLR). We thank the German Aerospace Society for providing powerful PCs in accordance with the funding decision, which facilitated the studies.

Conflicts of Interest: The funders had no role in the design of the study; in the collection, analyses, or interpretation of data; in the writing of the manuscript; or in the decision to publish the results.

Appendix A

Layer (type)	Output Shape	Param #	Connected to
input_2 (InputLayer)	[(None, None, None, 1)]	0	[]
conv2d_11 (Conv2D)	(None, None, None, 16)	160	['input_2[0][0]']
conv2d_12 (Conv2D)	(None, None, None, 16)	2320	['conv2d_11[0][0]']
max_pooling2d_3 (MaxPooling2D)	(None, None, None, 16)	0	['conv2d_12[0][0]']
conv2d_13 (Conv2D)	(None, None, None, 32)	4640	['max_pooling2d_3[0][0]']
conv2d_14 (Conv2D)	(None, None, None, 32)	9248	['conv2d_13[0][0]']
up_sampling2d (UpSampling2D)	(None, None, None, 32)	0	['conv2d_14[0][0]']
concatenate_3 (Concatenate)	(None, None, None, 48)	0	['up_sampling2d[0][0]', 'conv2d_12[0][0]']
conv2d_15 (Conv2D)	(None, None, None, 16)	6928	['concatenate_3[0][0]']
conv2d_16 (Conv2D)	(None, None, None, 16)	2320	['conv2d_15[0][0]']
conv2d_17 (Conv2D)	(None, None, None, 1)	17	['conv2d_16[0][0]']

Total params: 25633
Trainable params: 25633
Non-trainable params: 0

Figure A1. Structure of the simplified and more compact U-Net 0 architecture.

Layer (type)	Output Shape	Param #	Connected to
input_3 (InputLayer)	[(None, None, None, 1)]	0	[]
conv2d_18 (Conv2D)	(None, None, None, 8)	80	['input_3[0][0]']
conv2d_19 (Conv2D)	(None, None, None, 8)	584	['conv2d_18[0][0]']
max_pooling2d_4 (MaxPooling2D)	(None, None, None, 8)	0	['conv2d_19[0][0]']
conv2d_20 (Conv2D)	(None, None, None, 16)	1168	['max_pooling2d_4[0][0]']
conv2d_21 (Conv2D)	(None, None, None, 16)	2320	['conv2d_20[0][0]']
up_sampling2d_1 (UpSampling2D)	(None, None, None, 16)	0	['conv2d_21[0][0]']
concatenate_4 (Concatenate)	(None, None, None, 24)	0	['up_sampling2d_1[0][0]', 'conv2d_19[0][0]']
conv2d_22 (Conv2D)	(None, None, None, 8)	1736	['concatenate_4[0][0]']
conv2d_23 (Conv2D)	(None, None, None, 8)	584	['conv2d_22[0][0]']
conv2d_24 (Conv2D)	(None, None, None, 1)	9	['conv2d_23[0][0]']

Total params: 6481
Trainable params: 6481
Non-trainable params: 0

Figure A2. Structure of the simplified and more compact U-Net 1 architecture.

Layer (type)	Output Shape	Param #	Connected to
input_3 (InputLayer)	[(None, None, None, 1)]	0	[]
conv2d_14 (Conv2D)	(None, None, None, 8)	80	['input_3[0][0]']
conv2d_15 (Conv2D)	(None, None, None, 8)	584	['conv2d_14[0][0]']
max_pooling2d_2 (MaxPooling2D)	(None, None, None, 8)	0	['conv2d_15[0][0]']
conv2d_16 (Conv2D)	(None, None, None, 8)	584	['max_pooling2d_2[0][0]']
conv2d_17 (Conv2D)	(None, None, None, 8)	584	['conv2d_16[0][0]']
max_pooling2d_3 (MaxPooling2D)	(None, None, None, 8)	0	['conv2d_17[0][0]']
conv2d_18 (Conv2D)	(None, None, None, 8)	584	['max_pooling2d_3[0][0]']
conv2d_19 (Conv2D)	(None, None, None, 8)	584	['conv2d_18[0][0]']
max_pooling2d_4 (MaxPooling2D)	(None, None, None, 8)	0	['conv2d_19[0][0]']
conv2d_20 (Conv2D)	(None, None, None, 8)	584	['max_pooling2d_4[0][0]']
conv2d_21 (Conv2D)	(None, None, None, 8)	584	['conv2d_20[0][0]']
up_sampling2d_2 (UpSampling2D)	(None, None, None, 8)	0	['conv2d_21[0][0]']
concatenate_2 (Concatenate)	(None, None, None, 16)	0	['up_sampling2d_2[0][0]', 'conv2d_19[0][0]']
conv2d_22 (Conv2D)	(None, None, None, 8)	1160	['concatenate_2[0][0]']
conv2d_23 (Conv2D)	(None, None, None, 8)	584	['conv2d_22[0][0]']
up_sampling2d_3 (UpSampling2D)	(None, None, None, 8)	0	['conv2d_23[0][0]']
concatenate_3 (Concatenate)	(None, None, None, 16)	0	['up_sampling2d_3[0][0]', 'conv2d_17[0][0]']
conv2d_24 (Conv2D)	(None, None, None, 8)	1160	['concatenate_3[0][0]']
conv2d_25 (Conv2D)	(None, None, None, 8)	584	['conv2d_24[0][0]']
up_sampling2d_4 (UpSampling2D)	(None, None, None, 8)	0	['conv2d_25[0][0]']
concatenate_4 (Concatenate)	(None, None, None, 16)	0	['up_sampling2d_4[0][0]', 'conv2d_15[0][0]']
conv2d_26 (Conv2D)	(None, None, None, 8)	1160	['concatenate_4[0][0]']
conv2d_27 (Conv2D)	(None, None, None, 8)	584	['conv2d_26[0][0]']
conv2d_28 (Conv2D)	(None, None, None, 1)	9	['conv2d_27[0][0]']

Total params:9409
Trainable params:9409
Non-trainable params: 0

Figure A3. Structure of the simplified and more compact U-Net 2 architecture.

References

1. Stroth, U. *Plasmaphysik: Phänomene, Grundlagen und Anwendungen*, 2nd ed.; Springer: Berlin/Heidelberg, Germany, 2017.
2. Dietz, C.; Budak, J.; Kamprich, T.; Kretschmer, M.; Thoma, M.H. Phase transition in electrorheological plasmas. *Contrib. Plasma Phys.* **2021**, *61*, e202100079. [CrossRef]
3. Pustylnik, M.Y.; Fink, M.A.; Nosenko, V.; Antonova, T.; Hagl, T.; Thomas, H.M.; Zobnin, A.V.; Lipaev, A.M.; Usachev, A.D.; Molotkov, V.I.; et al. Plasmakristall-4: New complex (dusty) plasma laboratory on board the International Space Station. *Rev. Sci. Instrum.* **2016**, *87*, 093505. [CrossRef] [PubMed]
4. Dormagen, N.; Klein, M.; Thoma, M.H.; Schwarz, M. Machine Learning Approach for Multi Particle Tracking in Complex Plasmas. In Proceedings of the 2023 30th International Conference on Mixed Design of Integrated Circuits and System (MIXDES), Cracow, Poland, 29–30 June 2023; pp. 232–237. [CrossRef]
5. Schwabe, M.; Rubin-Zuzic, M.; Räth, C.; Pustylnik, M. Image Registration with Particles, Examplified with the Complex Plasma Laboratory PK-4 on Board the International Space Station. *J. Imaging* **2019**, *5*, 39. [CrossRef] [PubMed]
6. Mohr, D.P.; Knapek, C.A.; Huber, P.; Zaehringer, E. Algorithms for Particle Detection in Complex Plasmas. *J. Imaging* **2019**, *5*, 30. [CrossRef] [PubMed]
7. Sankur, B. Survey over image thresholding techniques and quantitative performance evaluation. *J. Electron. Imaging* **2004**, *13*, 146. [CrossRef]
8. Otsu, N. A Threshold Selection Method from Gray-Level Histograms. *IEEE Trans. Syst. Man Cybern.* **1979**, *9*, 62–66. [CrossRef]
9. Allan, D.; Caswell, T.; Keim, N.; van der Wel, C. *Trackpy: Trackpy v0.3.2*; Zenodo: Geneva, Switzerland, 2016. [CrossRef]
10. Midtvedt, B.; Helgadottir, S.; Argun, A.; Pineda, J.; Midtvedt, D.; Volpe, G. Quantitative digital microscopy with deep learning. *Appl. Phys. Rev.* **2021**, *8*, 011310. [CrossRef]
11. Midtvedt, B.; Pineda, J.; Skärberg, F.; Olsén, E.; Bachimanchi, H.; Wesén, E.; Esbjörner, E.K.; Selander, E.; Höök, F.; Midtvedt, D.; et al. Single-shot self-supervised object detection in microscopy. *Nat. Commun.* **2022**, *13*, 7492. [CrossRef] [PubMed]
12. Huang, H.; Schwabe, M.; Du, C.R. Identification of the Interface in a Binary Complex Plasma Using Machine Learning. *J. Imaging* **2019**, *5*, 36. [CrossRef] [PubMed]
13. Ronneberger, O.; Fischer, P.; Brox, T. U-Net: Convolutional Networks for Biomedical Image Segmentation. In Proceedings of the MICCAI 2015, Munich, Germany, 5–9 October 2015
14. Schmidt, U.; Weigert, M.; Broaddus, C.; Myers, G. Cell Detection with Star-convex Polygons. *arXiv* **2018**, arXiv:.1806.03535. https://doi.org/10.48550/arXiv.1806.03535.
15. Himpel, M.; Melzer, A. Fast 3D particle reconstruction using a convolutional neural network: application to dusty plasmas. *Mach. Learn. Sci. Technol.* **2021**, *2*, 045019. [CrossRef]
16. Rose, A. *Vision: Human and Electronic*, 3rd ed.; Optical Physics and Engineering; Plenum Press: New York, NY, USA, 1977.
17. Desislavov, R.; Martínez-Plumed, F.; Hernández-Orallo, J. Compute and Energy Consumption Trends in Deep Learning Inference. *Sustain. Comput. Inform. Syst.* **2023**, *38*, 100857. [CrossRef]
18. Pineda, J.; Midtvedt, B.; Bachimanchi, H.; Noé, S.; Midtvedt, D.; Volpe, G.; Manzo, C. Geometric deep learning reveals the spatiotemporal fingerprint of microscopic motion. *arXiv* **2022**, arXiv:2202.06355. https://doi.org/10.48550/arXiv.2202.06355.
19. Yaroshenko, V.; Pustylnik, M. Possible Mechanisms of String Formation in Complex Plasmas at Elevated Pressures. *Molecules* **2021**, *26*, 308. [CrossRef]

Chapter 3

Publication II: Local classification of crystalline structures in complex plasmas using a PointNet

Author Contributions

Niklas Dormagen

Conceptualization (lead)
Software (lead)
Data curation (lead), Investigation (lead), Validation (lead) and Visualization (lead)
Writing – original draft and revision

Max Klein

Data curation (supporting) and Software (supporting)
Writing – review and editing (supporting)

Andreas S. Schmitz and Lukas Wimmer

Data curation (supporting) and Methodology (supporting)
Writing – review and editing (supporting)

Markus H. Thoma and Mike Schwarz

Funding acquisition (lead)
Project administration (lead)
Writing – review and editing (supporting)

IOP Publishing Mach. Learn.: Sci. Technol. 5 (2024) 045006 https://doi.org/10.1088/2632-2153/ad8062

MACHINE LEARNING
Science and Technology

OPEN ACCESS

RECEIVED
17 June 2024

REVISED
13 September 2024

ACCEPTED FOR PUBLICATION
26 September 2024

PUBLISHED
8 October 2024

PAPER

Local classification of crystalline structures in complex plasmas using a PointNet

N Dormagen[1,2,*], **M Klein**[1,2], **A S Schmitz**[1], **L Wimmer**[1], **M H Thoma**[1] **and M Schwarz**[2]

[1] I. Institute of Physics, Justus Liebig University, D 35392 Giessen, Germany
[2] NanoP, THM University of Applied Sciences, D 35390 Giessen, Germany
[*] Author to whom any correspondence should be addressed.

E-mail: niklas.dormagen@nanop.thm.de

Keywords: complex plasma, image analysis, convolutional neural networks, PointNet.

Abstract

In complex plasmas, microparticles can form ordered crystalline structures under specific conditions. Accurately identifying these structures, such as face-centered cubic, hexagonal close-packed, and body-centered cubic, is a common task in physics. Previous methods rely on detecting symmetries in the spatial arrangement of particles, often requiring extensive calculations. This study presents a novel approach by utilizing a PointNet-based deep learning algorithm, called WignerNet, to classify these structures directly from three-dimensional reconstructions of their Voronoi cells. The model was trained exclusively on artificial and labeled data, incorporating various noise levels, and subsequently tested on real experimental data. The results demonstrate that our method effectively classifies structures, reducing computational complexity and improving accuracy compared to conventional techniques. This advancement opens up new possibilities for real-time analysis of complex plasma systems in various research.

1. Introduction

Ionized gases that contain free-moving electrons and ions are known as plasmas. They exhibit a density of positive and negative charge carriers that is approximately equal, which is one of the defining characteristics of plasmas [1]. Complex plasmas are a specific type of plasma that, in addition to electrons, ions, and neutral gas atoms, contain microparticles such as dust. In low-temperature plasmas, the high mobility of electrons causes these microparticles to acquire a negative charge, thereby introducing a new, strongly coupled component to the plasma.

A particularly noteworthy phenomenon in complex plasmas is the formation of ordered structures, commonly referred to as plasma crystals. These structures emerge from the strong interactions between the negatively charged microparticles. The fundamental interaction between these microparticles is described by the Yukawa potential, which accounts for the repulsive force between the charged particles and the shielding effect of the surrounding plasma. However, the Yukawa potential alone does not fully explain the stabilization of these structures, particularly in direct current (DC) discharges. The wake potential, which arises due to the relative motion of ions past the microparticles, introduces an anisotropic and often attractive component to the interaction, further stabilizing crystalline structures (such as face-centered cubic (fcc), hexagonal close-packed (hcp), and body-centered cubic (bcc)) observed within complex plasmas [2, 3].

To study these phenomena, experiments are conducted using the PK-4 ('Plasmakristall-Experiment 4') setup, which is specifically designed for observing complex plasma behavior in a DC discharge environment. This setup involves injecting microparticles into a plasma created within a U-shaped glass tube filled with a noble gas like argon or neon. The microparticles are observed using high-resolution cameras and illuminated by a laser, allowing for detailed analysis of their arrangement and dynamics within the plasma.

Given the complexity of the structures formed in these plasmas, advanced analytical methods are required to accurately classify and understand them. Conventional methods have focused on identifying symmetries within the crystalline structures [4–7]. However, recent advancements in machine learning,

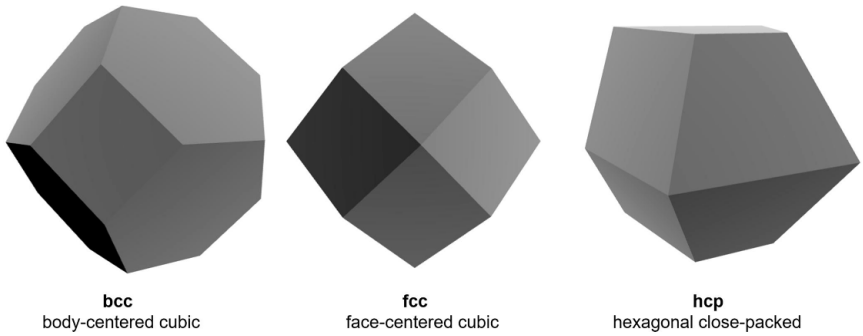

Figure 1. Three-dimensional view of the Wigner–Seitz cells of the fcc, bcc, and hcp structures.

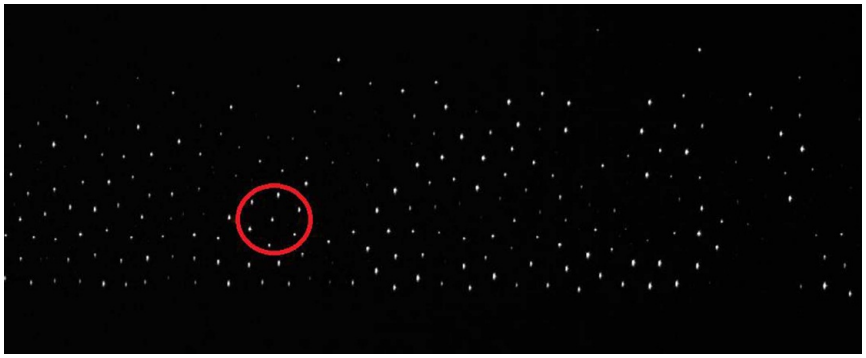

Figure 2. Experimental data generated on the engineering model (EM) of PK-4 in the JLU laboratory (for more details see chapter 4). The red circle marks an exemplary area in which potentially ordered structures can be found. In two dimensions, this can be assumed due to the hexagonal structure.

particularly in the analysis of three-dimensional point clouds, have opened new possibilities for more sophisticated and accurate analysis.

This study introduces WignerNet, a novel methodology that uses PointNet [8], a deep learning architecture developed for processing 3D point clouds. Unlike conventional methods that rely on feature vectors derived from mathematical operations, WignerNet directly utilizes the three-dimensional point cloud of the Wigner–Seitz cells, providing a more direct and potentially more accurate classification of the observed structures. The Wigner–Seitz cell represents a special primitive cell of a crystal lattice, defined by a unique construction rule (see figure 1). The following section 2 will provide a detailed explanation of the WignerNet method, discussing its development, underlying principles, and application to the analysis of complex plasma structures. By integrating this advanced machine learning approach, we aim to enhance the accuracy of our analysis of complex plasmas without the need for extensive computational operations. In section 3, we provide a detailed exposition of the MCS method and offer a comparative analysis with our proposed WignerNet approach. Subsequently, in section 4, we apply the WignerNet method to analyze experimental data from the Pk-4 experiment, specifically investigating the presence of crystalline structures. Additionally, we present a comprehensive description of the experimental setup used in this study.

2. WignerNet

It is challenging to discern the underlying structures merely by examining the two-dimensional image data (see figure 2).

To conduct an accurate analysis of potentially crystalline structures, it is essential to examine them in three-dimensional space. To obtain a three-dimensional representation of the particle cloud, a scan is conducted along the Y-axis of the PK-4 setup. The laser and camera are mounted on a motorized stage and move at a speed of 0.5 mm s^{-1} along the Y-axis, while the camera captures images at a frame rate of 60 fps. This procedure involves multiple recordings of each particle, with the frequency dependent on the camera frame rate and the speed of the motorized stage. Through the tracking of particle positions across the images, it is possible to ascertain which positions correspond to each individual particle.

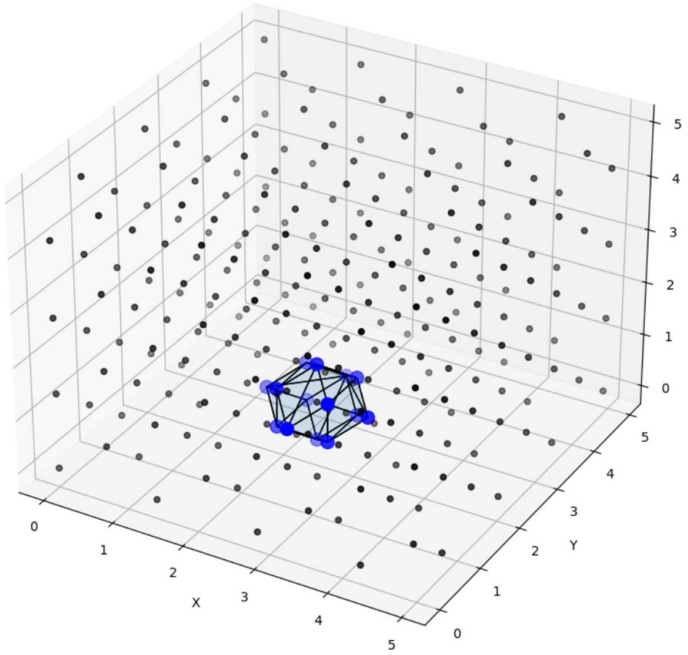

Figure 3. Constructed Wigner–Seitz cell in artificial bcc domain.

Particle localization was performed using a U-net-based method [9, 10], and the resulting position data were tracked through the image sequence using trackpy [11]. The y-positions of each particle track are determined by the current position of the motorized stage, while the x and z positions are obtained from the 2D coordinates in the images. Consequently, the three-dimensional positions are calculated by averaging the x-, y-, and z-coordinates of each unique particle track. This methodology enables the reconstruction of the positions of all dust particles as a three-dimensional point cloud.

However, several challenges arise in this process. The particles are never in a state of complete rest, which results in noisy and often challenging-to-analyze data. Therefore, the method used should be universally applicable and avoid hard-coded parameters such as cutoff radii. There are several methods available for describing crystalline structures, some of which are grounded in mathematical principles. Dietz *et al*'s work has shown robustness against noisy data by merging various techniques into a vector for classification via a multi-layer perceptron [12]. Our approach is notably influenced by their methodology.

Defining the neighborhood of each particle is essential for analyzing a particle cloud. In order to define the neighborhood, we initially utilize the corresponding Delaunay neighborhood, and subsequently employ Voronoi cells. This approach is more adaptable to local structure, which is particularly important for mixed-phase systems [12]. The structures are described according to established methodologies based on Voronoi cells, which are calculated using the SCIPY [13] implementation of QHull [14]. Given the three-dimensional nature of structural data, it is important to maintain this property during analysis. Therefore, we propose using the three-dimensional Wigner–Seitz cell for structure classification (see figure 3). Utilizing the structure of this cell should yield clear classification results.

A neural network will be utilized for the purpose of classifying the structures. In order to ensure the model's robustness, it is essential to consider the effects of rotation, translation, and scale when representing ordered structures. Accordingly, we propose a translation-, rotation-, and scale-invariant method utilizing the three-dimensional Wigner–Seitz cell. For such applications, the network architecture designated as PointNet [8], as developed by researchers at Stanford University, has already demonstrated considerable promise. Consequently, we intend to prepare the three-dimensional structure of the Wigner–Seitz cell in a manner that will facilitate its direct integration with a PointNet architecture. In order to ensure uniformity in the description of the Wigner–Seitz cells, they are represented as point clouds, each consisting of 1000 points (see figure 4). Subsequently, the aforementioned uniform point clouds can be transferred directly to the PointNet architecture, which allows for the classification of the cells according to their crystal structures, specifically whether they are fcc, bcc, or hcp.

Analogous to Dietz *et al* we choose to only identify the crystalline structure of the particle, not whether the particle is in a solid or disordered state. To achieve this, we filter the disordered particles out by using a

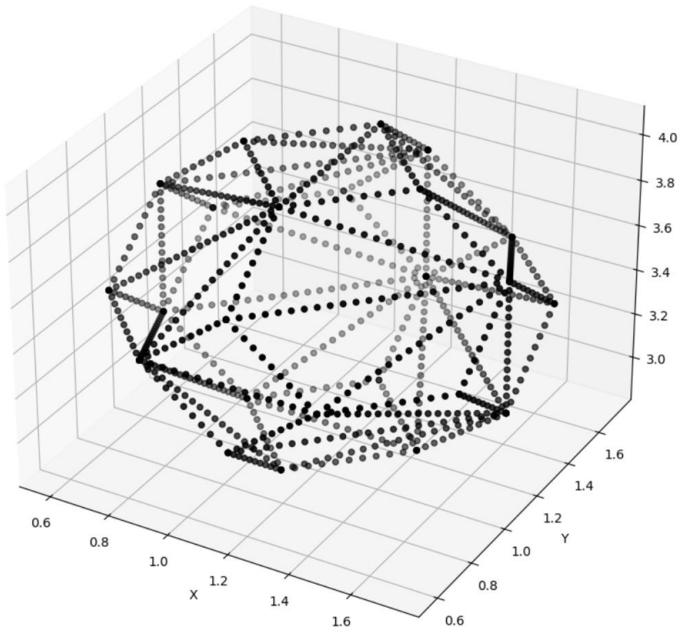

Figure 4. Point cloud of the bcc Wigner–Seitz cell used as input for the WignerNet.

modified scalar product of the bond-orientational order parameter [15, 16] defined for a Minkowski structure metric (MSM) [17]. This method is robust to uncertainties in particle positions of up to 14% of the nearest neighbor distance, e.g. due to oscillations in the scan direction [17]. For a particle i, the order parameters are calculated as follows:

$$q'_{lm} = \sum_{f \in F(i)} \frac{A(f)}{A} Y_{6m}\left(r_{ij}\right). \tag{1}$$

Here, Y_{6m} are the spherical harmonics with $l = 6$, and the sum runs over all Voronoi neighbors. The connecting vector of the two neighboring particles i and j is r_{ij}. The surface of the Voronoi cell A is defined by the sum over the corresponding facet areas $A = \sum_{f \in F(i)} A(f)$. Then, the complex vector is normalized over all possible orders m given by

$$\tilde{q}'_{6m(i)} = \frac{q'_{6m(i)}}{\left(\sum_{m=-6}^{6} |q'_{6m(i)}|^2\right)^{1/2}}. \tag{2}$$

For i the product is averaged over all neighbors j

$$S(i) = \frac{1}{N} \sum_{j=1}^{N} \sum_{m=-6}^{6} \tilde{q}'_{6m(i)} \tilde{q}'^{*}_{6m(j)}, \tag{3}$$

where $S(i)$ is the scalar product of the MSM, N is the number of neighbors and $\tilde{q}'^{*}_{6m(j)}$ is complex conjugated. If the product $S(i)$ is less than 0.55, a particle is considered solid [12]. For particles identified as being in the solid state, Wigner–Seitz point clouds are generated from the dust particle positions. These point clouds are then input into the PointNet for further analysis.

The use of PointNet in our approach offers a significant advantage with respect to direct processing of point clouds. In comparison to other methods, it eliminates the need for pre-processing steps, including those involving voxel or graph conversion. Unlike convolutional neural networks (CNNs) and graph neural networks (GNNs), PointNet can handle unstructured data in the form of point clouds, preserving the full spatial structure without any loss of information.

One of PointNet's key strengths is its permutation invariance, meaning the order of points does not affect the output, which is crucial for processing point clouds where point order can vary. PointNet captures both global features of the entire point cloud and local features of individual points through multiple

Layer (type)	Output Shape	Param #
input_points (InputLayer)	(None, 1000, 3)	0
conv1d (Conv1D)	(None, 1000, 128)	512
batch_normalization (BatchNormalization)	(None, 1000, 128)	512
conv1d_1 (Conv1D)	(None, 998, 128)	49,280
batch_normalization_1 (BatchNormalization)	(None, 998, 128)	512
max_pooling1d (MaxPooling1D)	(None, 499, 128)	0
global_max_pooling1d (GlobalMaxPooling1D)	(None, 128)	0
dense (Dense)	(None, 256)	33,024
batch_normalization_2 (BatchNormalization)	(None, 256)	1,024
dropout (Dropout)	(None, 256)	0
dense_1 (Dense)	(None, 128)	32,896
batch_normalization_3 (BatchNormalization)	(None, 128)	512
dropout_1 (Dropout)	(None, 128)	0
dense_2 (Dense)	(None, 128)	16,512
batch_normalization_4 (BatchNormalization)	(None, 128)	512
output (Dense)	(None, 3)	387

Total params: 135,683 (530.01 KB)

Trainable params: 134,147 (524.01 KB)

Non-trainable params: 1,536 (6.00 KB)

Figure 5. Architecture of the WignerNet model.

transformations and pooling layers. This enables the analysis of structural information at multiple scales. Unlike CNNs, which struggle with local information, or GNNs, which struggle to capture global relationships despite their strength in analyzing local structural details, PointNet provides a balanced solution. Additionally, PointNet is more computationally efficient and scalable compared to alternative approaches [18]. Its ability to work with raw data without extensive preprocessing simplifies both the training process and practical application, making it particularly advantageous for managing large datasets.

2.1. Neural network architecture

The network depicted in figure 5 is a architecture, designed for classifying point clouds. We implemented the network in tensorflow [19]. Convolutional layers are responsible for identifying local features in the input data. This network employs two convolutional layers with ReLU activation functions, followed by batch normalization layers to stabilize training. The max-pooling layer reduces the dimensionality of feature maps by extracting maximum values within small windows, thereby reducing computational costs and enhancing spatial invariance. The global max-pooling layer extracts global features from the feature maps and reduces dimensionality to a vector. The dense layers, comprising fully connected layers, further process extracted features and conduct classification. In this network, three dense layers with ReLU activation functions, batch normalization, and dropout for regularization are utilized. The output layer consists of three neurons with a softmax activation function, computing probabilities for each class in the classification task. This network is well-suited for point cloud classification because it employs convolutional and pooling layers to extract local and global features, followed by fully connected layers for feature combination and classification.

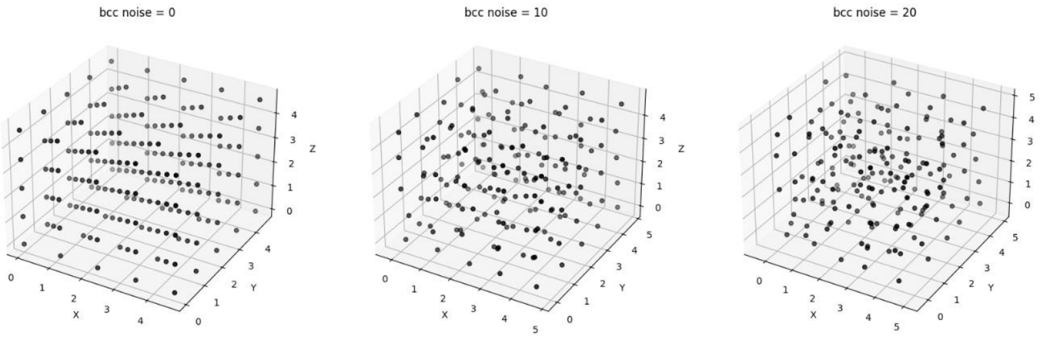

Figure 6. Excerpts of the artificial data at different noise levels.

Convolutional layers enable capturing spatial structures in point clouds, while pooling layers provide invariance to shifts and distortions. As a result, the network can not only distinguish between fcc, bcc and hcp structures, but also identify them at different noise levels.

2.2. Training WignerNet with noisy data

Given the inherent challenges and labor-intensive nature of labeling real image data, the creation of artificial data that adequately represents crystalline structures is a preferable alternative. This process should incorporate noise and drift movements of individual particles. To address noise in the artificial data, Gaussian noise is initially added to the dataset. This Gaussian-distributed shift mimics the Brownian motion of the particles. The standard deviation σ of the Gaussian noise is increased from 0.01 a to 0.2 a with a step size of 0.01 a, where a is the average distance of the nearest neighbors. Consequently, domains are generated for each structure within a specified volume for each noise level. Figure 6 illustrates exemplary excerpts of the artificial data.

The artificially generated particle positions are used to calculate the scalar product of the MSM $S(i)$ for each dust particle within a given lattice. This metric determines whether a particle is in a solid state ($S(i) < 0.55$) or in a liquid state. For particles classified as solid, Wigner–Seitz point clouds are generated based on the dust particle positions. These point clouds are then labeled according to the underlying lattice structure. Using these labeled Wigner–Seitz cell point clouds, the WignerNet is trained to recognize hcp, fcc, and bcc lattice structures.

The optimal results were achieved with approximately 6000 training and 4000 test data points. During training, the Adam optimizer with a learning rate of $\alpha = 0.0001$ was employed, and the loss was computed using categorical cross-entropy,

$$Loss\,(T_i, P_i) = -\sum_{i=1}^{C} T_i \cdot \log\,(P_i)\,, \tag{4}$$

with T_i and P_i being the truth and predicted value of each structure, C being the number of classes.

2.3. Evaluation

The trend of the individual crystal structures resulting from $S(i) < 0.55$ is shown in the figure 7. Obviously, the number of structures gradually decreases with increasing noise. At a noise level of 10%, about 64% of the hcp, ≈84% of the fcc, and ≈88% of the bcc structures are still present [12]. To test and validate the network, additional data sets are generated analogous to the training data set. To avoid overfitting the network to the training data, each dataset is generated with a random shape factor for the Gaussian noise. This ensures that the data is scale- and rotation-invariant for each noise level.

The predictions of the Wigner network show only a few misclassified particles (≈4.6%) for up to 20% noise (see figure 7). Over the entire noise range, the misclassifications do not exceed ≈4.6%.

3. Comparison to mixed crystal signature (MCS)

We will now outline the MCS analysis procedure for comparison with our own approach. They use several proven methods and generalize them in a fixed neighborhood to create such a feature vector, which they call ‘crystal signature.’ A crucial aspect of this analysis is the definition of the neighborhood. In this study, the neighborhood is determined using Delaunay triangulation [12]. First, the distances between all neighbors,

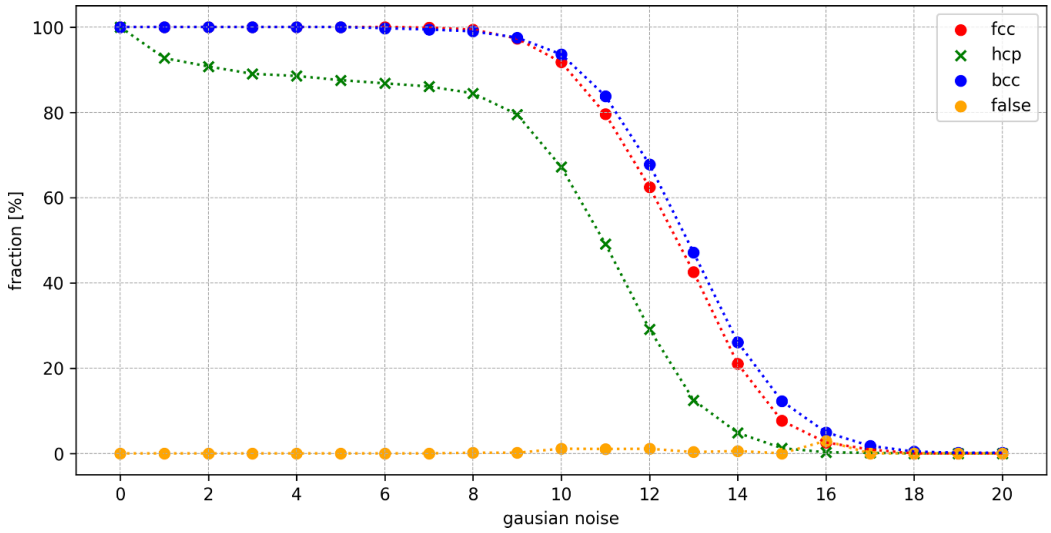

Figure 7. This figure shows the occurrence of each crystal structure and the number of false predictions made by WignerNet at each given noise level. It should be noted that the number of detected structures is normalized to 100% in the undisturbed case, as referenced in [12].

denoted as j and k, are computed. These distances are then normalized by a characteristic length d_0. This is the average distance between a particle and its six nearest neighbors. Given the variable number of neighbors, N, for each particle, and the total number of distances, $N/2(N-1)$, it is convenient to create a histogram of all d_{jk} values. This histogram is divided into a given number of equidistant bins, in this case $N_{\text{bins}} = 12$, which serves as the feature space. Furthermore, the analysis also considers the bond angles between neighboring particles [20]. These bond angles, which characterize a particle i along with a pair of its neighbors j and k, are calculated using the prescribed formula:

$$\cos\left[\theta_{jk}(i)\right] = \frac{\left(\mathbf{r}_i - \mathbf{r}_j\right)\cdot\left(\mathbf{r}_i - \mathbf{r}_k\right)}{\|\mathbf{r}_i - \mathbf{r}_j\|\|\mathbf{r}_i - \mathbf{r}_k\|} \quad (\text{for } j \neq k)\,. \tag{5}$$

Since a clear distinction between fcc and hcp is difficult, the MSM of Mickel *et al* is included in the analysis [12, 21]:

$$q_{lm}^{'} = \sum_{f\in F(i)} \frac{A(f)}{A} Y_{lm}\left(\theta_f, \phi_f\right), \tag{6}$$

$$q_l^{'} = \sqrt{\frac{4\pi}{2l+1}\sum_{m=-l}^{l} |\, q_{lm}^{'}\,|^2}. \tag{7}$$

The parameter $q_l^{'}$ is the second order rotational invariant and is calculated for $l = 4{,}6$. The calculation of the q_4 and q_6 bond-orientational order parameters provides valuable insight into the local structure and symmetry of the particles [20]. These parameters are of great importance in the differentiation of the various forms of local order. While structures of cubic symmetry exhibit a notable correlation with q_4, structures of icosahedrally symmetric nature are predominantly observed for q_6 [20]. The azimuthal angle is denoted by θ_f and the polar angle by ϕ_f. The spherical harmonics Y_{lm} are weighted by the Voronoi facet area A(f) for all facets $f \in F(i)$. The surface area of the Voronoi cell facet separating the two neighboring spheres corresponding to a given bond is given by the sum of the areas of all the facets, which is denoted by $A = \sum_{f\in F(i)} A(f)$. This quantity is then defined as the total surface area of the Voronoi cell boundary $F(i)$ of sphere i. They also compute the third-order rotational invariant $w_l^{'}$ based on the MSM:

$$w_l^{'}(i) = \sum_{\substack{m_1,m_2,m_3 \\ m_1+m_2+m_3=0}}^{l} \begin{pmatrix} l & l & l \\ m_1 & m_2 & m_3 \end{pmatrix} \times \frac{q_{lm1}^{'}(i)\, q_{lm2}^{'}(i)\, q_{lm3}^{'}(i)}{q_l^{'}(i)^3}. \tag{8}$$

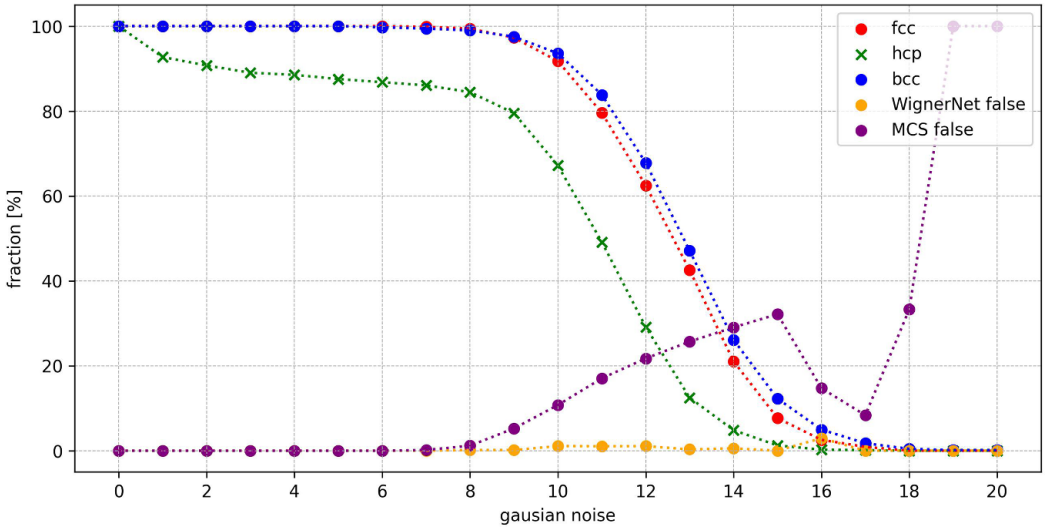

Figure 8. This figure shows the performance of both methods in the classification of hcp, fcc and bcc at a certain noise level. The misclassified structures were compared with each other.

The Wigner 3-*j* symbol is represented by the expression in large brackets. To further distinguish between fcc and hcp structures, a method based on Minkowski tensors is used, which can accurately quantify the shape of a convex surface. Differentiating the isotropic cells of fcc and hcp requires a fourth-order translational and scale-invariant tensor:

$$\left(W_1^{0,4}\right)_{\alpha\beta\gamma\delta} = \sum_f \frac{A(f)}{A} n_\alpha n_\beta n_\gamma n_\delta. \tag{9}$$

The Cartesian components of the triangulated facet normals are denoted by n_α for $\alpha = 1,2,3$. The facet normals are weighted by the facet area $A(f)$. Writing the tensor as a symmetric 6×6 matrix in Voigt notation allows them to compute the eigenvalues. The eigenvalues $(\zeta 1, \ldots, \zeta 6)$ are rotation invariant and are included in the crystal signature. Overall, the MCS consists of 31 dimensions, which allows for a reliable classification of different crystalline structures [12]. These signatures are then passed to a multi-layer perceptron for classification.

3.1. Comparison results

The results of applying each network to the same set of artificial data are illustrated in figure 8. The observed trend in the occurrence of structures across different noise levels is consistent, as both methods classify the structures as solid when $S(i) < 0.55$. The artificial dataset consists of labeled structures (in total 8691 fcc, 8502 hcp and 9149 bcc structures) generated for noise levels from 0 to 20. If the result of the method differs from the true label, it is considered to be false.

While the analysis of the Wigner network seems to deliver robust results across the entire noise range, the accuracy of the MCS method appears to be more significantly affected by noise levels, showing an 11% misclassification rate at a 10% noise level. In contrast, the Wigner network maintains a lower misclassification rate of around 3% under the same conditions. The robustness of the Wigner network to noise is particularly noteworthy. While the MCS method's error rate increases markedly with higher noise levels, the Wigner network remains largely unaffected. This indicates that the Wigner network's analysis is relatively insensitive to noise, allowing for reliable performance regardless of the prevailing noise conditions. Additionally, an examination of the correctly classified structures across the noise range shows that the Wigner network consistently recognizes all three structures more reliably than the MCS method (see figure 9).

If the corresponding confusion matrix (see figure 10) is also included in the comparison of the two methods, it becomes clear that the Wigner network classifies the structures in principle more solidly than the MCS method. The most significant deviations in the WignerNet analysis occur in the classification of the fcc structure, which is most often confused with the hcp structure. This confusion also appears to be the primary

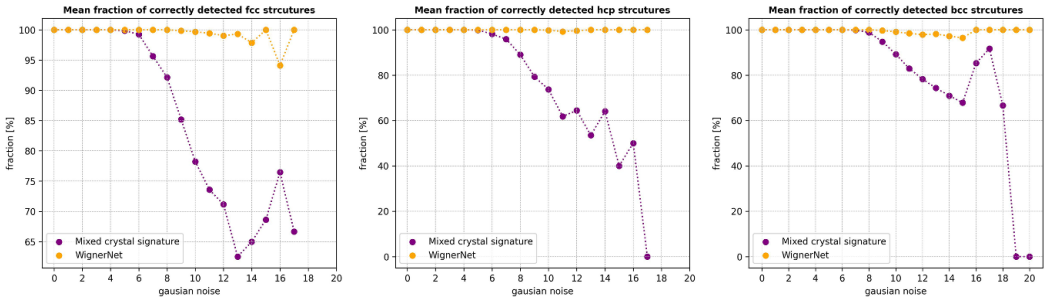

Figure 9. Mean fraction of correctly detected structures at given noise level. Starting at a noise level of 17, solid fcc and hcp structures can no longer be analyzed, with only a few bcc structures remaining solid up to a noise level of 20.

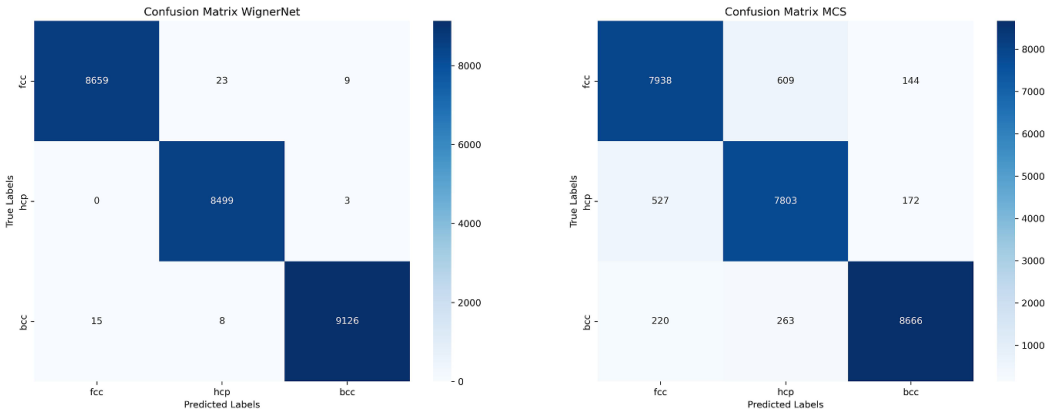

Figure 10. Comparison of confusion matrices for WignerNet and MCS. The base data set is the artificial data for a noise level of 0 to 20.

source of error in the MCS analysis. This misclassification may stem from the fact that both structures share a coordination number of 12, meaning each particle has 12 nearest neighbors, whereas the bcc structure has a coordination number of 8. As a result, the fcc and hcp structures are more likely to be confused, especially in the presence of noise.

These findings suggest that the Wigner network is a superior method for particle classification in noisy environments, providing more accurate and consistent results compared to traditional methods like MCS. The ability of the Wigner network to maintain high accuracy despite noise interference highlights its potential for robust applications in various scientific and industrial contexts where noise is an inevitable factor.

4. Analyzing experimental data

Having established WignerNets effectiveness with artificial data, we proceeded to evaluate its performance using real data from the PK-4 ('Plasmakristall-Experiment 4') setup. The Plasma and Space Physics research group of the JLU Giessen has both an engineering model (EM) of PK-4, which has been converted for use under zero gravity conditions on parabolic flights, and the science reference model (SRM) No. 1, which is identical to the flight model on the ISS.

The image data of the microparticles were recorded using the engineering model of PK-4 in the laboratory at Justus Liebig University (see figure 11). The primary difference between this model and the flight model is the use of a new xiQ camera, which offers higher resolution and an increased frames per second.

The setup is specifically designed for the study of complex plasma in a direct current (DC) discharge that occurs in an elongated, U-shaped glass tube. This tube is filled with neon at pressures between 40 and 100 Pa. The gas inlet is regulated by a flow controller at one end, while a vacuum pump at the opposite end

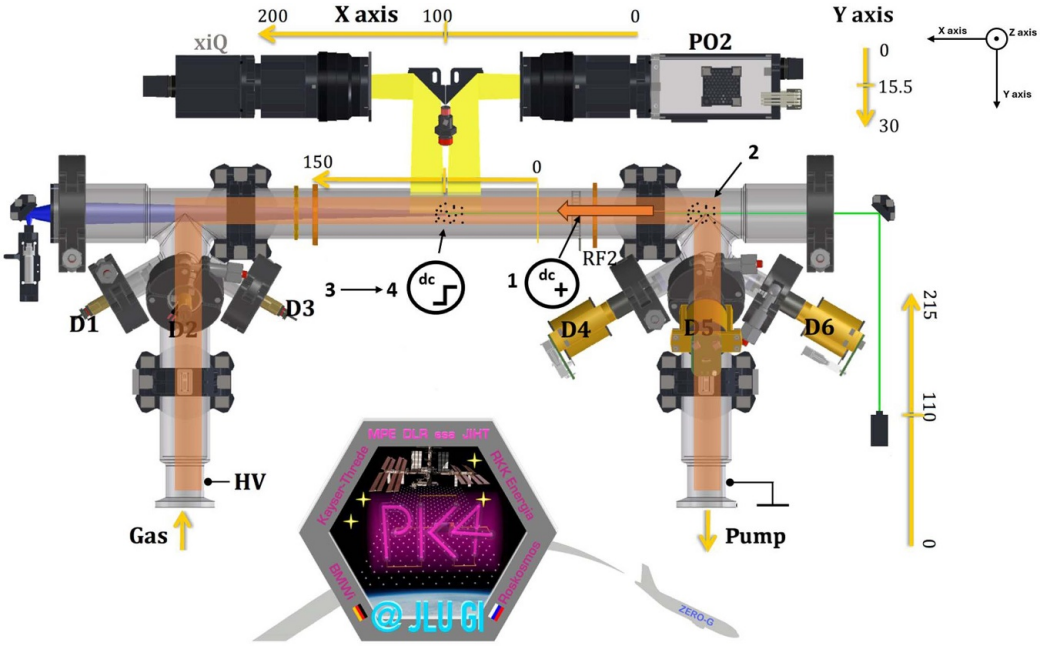

Figure 11. This is a sketch of the PK-4 experimental setup provided by the Thoma research group of the JLU Giessen. The sketch illustrates the trapping of microparticles within the field of view: 1 - ignition of the dc plasma, 2 - microparticle injection, 3 - microparticles arrival into the PO camera FoV, and 4 - microparticle trapping in the field of view through polarity-switching mode.

maintains the desired pressure level within the system [22]. Electrodes positioned at both ends of the tube generate a high-voltage electric field, which ionizes the neon gas, thereby creating a low-temperature plasma.

For the formation of complex plasma, monodisperse microparticles of melamine formaldehyde (MF), each with a diameter of 3.4 μm, are introduced into the plasma via particle injector D5 (see figure 11).

The setup is equipped with two particle observation cameras, capable of moving both longitudinally and radially within the plasma chamber, corresponding to the x and y axes, respectively (as illustrated in figure 11). These include a CCD camera (Particle Observation 2 or PO2) with a resolution of 1600×1200 pixels and a CMOS camera (xiQ) offering a higher resolution of 2048×2048 pixels. In this study, only images from the xiQ camera were utilized. The xiQ camera was chosen for its higher resolution, which is crucial for capturing detailed particle images, thereby ensuring the accuracy of the classification process. To visualize the microparticles, a "particle observation laser" (PO laser) emitting green light at a wavelength of 532 nm is employed. The laser light scatters off the microparticles and is subsequently captured by the cameras. A more detailed description of the PK-4 experiment can be found in [23].

To stop the movement of the particles within the camera's field of view, the DC field was switched at frequencies of 500 Hz and 1000 Hz (see table 1). Before scanning, the particle cloud was stopped in the field of view for 3 min to allow the particle structures to transition into the crystalline phase. Images were captured at a frame rate of 60 fps, with a scan speed of 0.5 mm s^{-1}. The plasma chamber was scanned from 10.5 mm to 18 mm along the Y-axis. The electrode current was always $I = 1$ mA.

The positions of dust particles in three-dimensional space are reconstructed from scan data using trackpy [11] (for more details see section 2). These reconstructed positions are then used to compute the scalar product of the MSM $S(i)$ for each dust particle, determining whether a particle is in a solid crystalline state ($S(i) < 0.55$) or a liquid state. For particles identified as solid, Wigner–Seitz point clouds are generated. These point clouds are subsequently fed into the WignerNet to classify their structure.

Table 2 indicates that the proportion of ordered structures in a scan is highest at a pressure of 1 mBar, while it is lowest at a pressure of 0.4 mBar. Notably, the composition of these ordered structures changes with increasing pressure. At lower pressures, bcc and hcp structures predominantly prevail, whereas with increasing pressure, the relative proportion of both fcc and hcp structures rises, while the relative proportion of bcc structures decreases. In addition, figure 12 shows that the ordered structures form distinct clusters.

Table 1. Experimental settings with a particle size of 3.4 μm. All experiments were conducted in neon.

No.	p [mBar]	Frequency [Hz]
1	0.4	500
2	0.6	500
3	0.8	500
4	1	500
5	0.4	1000
6	0.6	1000
7	0.8	1000
8	1	1000

Table 2. The number of structures detected in a particle cloud, consisting of the listed number of particles, identified using WignerNet for each experiment.

No.	Particles	fcc	hcp	bcc	Solid
1	14 639	0	8	38	0.31%
2	25 995	2	12	204	0.84%
3	13 080	433	42	155	4.82.%
4	549	220	67	387	12.27%
5	18 449	5	6	40	0.28%
6	4412	7	10	148	1.91%
7	2806	13	43	260	6.63%
8	5011	24	35	380	9.39%

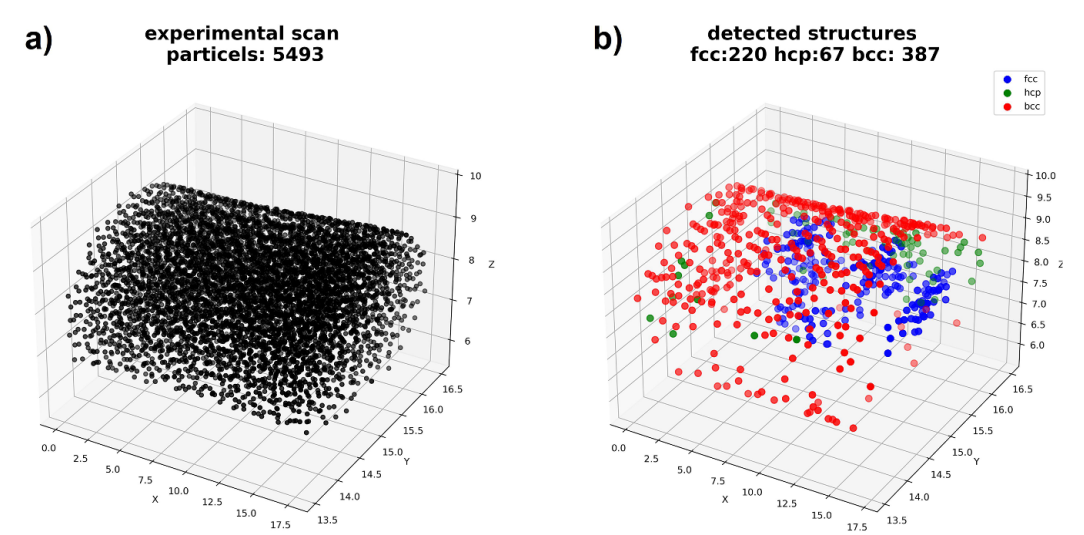

Figure 12. In this figure, the reconstructed three-dimensional positions of the particles from the fourth experimental scan (a) are compared with the analysis results obtained using WignerNet (b). Only particles that are considered solid are taken into account in the analysis (b).

The bcc structures are predominantly located at the periphery of the cloud, while the fcc structures are predominantly formed at the center of the cloud. This suggests that bcc structures are more likely to occur at higher dust densities, while fcc structures are more common at lower dust densities. The hcp structure, on the other hand, appears to be present over a wider range of dust densities. This observation should be verified in further experiments.

In addition, time-resolved studies of structural order during polarity switching experiments on PK-4 could certainly be of interest in the future. It would probably be advantageous to observe particle clouds of similar size over a longer period of time at a given pressure.

4.1. Limitation of the network

In order to evaluate the applicability of the model to real experimental data, it is important to consider its limitations, particularly in the processing and analysis of camera images. The neural network identifies two-dimensional particle positions from these images, so the quality of the input data—affected by noise,

illumination, and resolution—is critical. Once these positions are determined, they are correlated to reconstruct the three-dimensional particle positions. This reconstruction can introduce errors, but in our PK-4 experiments, the distance between particles is sufficiently large (at least ten times their diameter), which in turn minimizes the impact of these errors on the structure classification.

The initial image processing employs a U-Net to binarize images, enhancing the detection of particle positions by reducing noise interference [9]. Although some noise is inevitable, prior research has shown that varying the signal-to-noise ratio has a minimal impact on particle detection accuracy [9, 24].

Given the sensitivity of crystalline structure formation to changes in plasma conditions, we meticulously aligned the artificial training data with the actual experimental environment. As a result, the model demonstrated consistent classification performance in real experiments, confirming its reliability under varying experimental conditions.

5. Conclusion

In summary, this paper introduces a novel machine learning approach for detecting and classifying ordered particle formations in complex plasmas using a PointNet [8] architecture. This method significantly enhances the accuracy of ordered structure classification compared to previous techniques and demonstrates greater resilience to data noise. Notably, the method showed superior performance in noisy environments (at a 10% noise level), where the Wigner network maintained a misclassification rate of around 3%, compared to 11% for conventional methods like MCS. This robustness makes it particularly valuable for applications in various scientific and industrial contexts where noise is prevalent.

Additionally, the method enables a global evaluation of a particle cloud without the need for extensive calculations of additional factors. The analysis algorithm generates point clouds in the form of Wigner–Seitz cells, which are then classified using the established PointNet architecture. The use of artificially generated training data, with variations in scale, rotation, and noise levels, proved effective for robust network training. The ability to classify structures such as fcc, bcc, and hcp accurately even under varying noise conditions further highlights the method's robustness.

Moreover, this approach was applied to real experimental data from the PK-4 setup, demonstrating its practical applicability. Future analyses, particularly those utilizing advanced setups like COMPACT [25] with stereoscopic cameras, could achieve even higher precision in time-resolved three-dimensional particle positions [26]. This would allow for more detailed studies on the dynamics of ordered structures in complex plasmas, potentially refining existing theoretical models.

This advancement offers new possibilities for evaluating ordered structures and has the potential to refine previous findings in this field. For example, time-resolved studies of ordered structures at a specific pressure could be conducted, and spatial analysis of the clusters formed by these structures could yield valuable insights.

Data availability statement

All data that support the findings of this study are included within the article (and any supplementary files).

Acknowledgments

This work is supported by the German Aerospace Agency (DLR). We thank the research group around Markus H Thoma and M Kretschmer at Justus Liebig University Giessen for providing the data used in this study and the German Aerospace Society for providing powerful PCs in accordance with the funding decision, which facilitated the studies. This project was supported by the German Federal Ministry of Economic Affairs and Climate Action under Contract No. 50WK2270B.

Supported by:

on the basis of a decision
by the German Bundestag

ORCID iDs

N Dormagen https://orcid.org/0009-0001-9158-4034
M Klein https://orcid.org/0009-0009-9596-7671

References

[1] Stroth U 2018 *Plasmaphysik: Phänomene, Grundlagen und Anwendungen* 2nd edn (Springer) (https://doi.org/10.1007/978-3-662-55236-0)
[2] Ivlev A V, Thoma M H, Räth C, Joyce G and Morfill G E 2011 *Phys. Rev. Lett.* **106** 155001
[3] Matthews L S *et al* 2021 *J. Plasma Phys.* **87** 905870618
[4] Leitherer A, Ziletti A and Ghiringhelli L M 2021 *Nat. Commun.* **12** 6234
[5] Dietz C, Kretschmer M, Steinmüller B and Thoma M H 2018 *Contrib. Plasma Phys.* **58** 21–29
[6] Ziletti A, Kumar D, Scheffler M and Ghiringhelli L M 2018 *Nat. Commun.* **9** 2775
[7] Ward L, Liu R, Krishna A, Hegde V I, Agrawal A, Choudhary A and Wolverton C 2017 *Phys. Rev.* B **96** 024104
[8] Qi C R, Su H, Mo K and Guibas L J 2017 Pointnet: deep learning on point sets for 3d classification and segmentation (arXiv:1612.00593)
[9] Dormagen N, Klein M, Schmitz A S, Thoma M H and Schwarz M 2024 *J. Imaging* **10** 40
[10] Ronneberger O, Fischer P and Brox T 2015 U-net: Convolutional networks for biomedical image segmentation (arXiv:1505.04597)
[11] Allan D, Caswell T, Keim N and van der Wel C 2016 trackpy: Trackpy v0.3.2
[12] Dietz C, Kretz T and Thoma M H 2017 *Phys. Rev.* E **96** 011301
[13] Virtanen P *et al* 2020 *Nat. Methods* **17** 261–72
[14] Barber C B, Dobkin D P and Huhdanpaa H 1996 *ACM Trans. Math. Softw.* **22** 469–83
[15] Rein ten Wolde P, Ruiz-Montero M J and Frenkel D 1996 *J. Chem. Phys.* **104** 9932–47
[16] Lechner W and Dellago C 2008 *J. Chem. Phys.* **129** 114707
[17] Steinmüller B, Dietz C, Kretschmer M and Thoma M H 2017 *Phys. Plasmas* **24** 033705
[18] Aach M, Inanc E, Sarma R, Riedel M and Lintermann A 2023 *J. Big Data* **10** 96
[19] TensorFlow Developers 2024 Tensorflow
[20] Steinhardt P J, Nelson D R and Ronchetti M 1983 *Phys. Rev.* B **28** 784–805
[21] Mickel W, Kapfer S C, Schröder-Turk G E and Mecke K 2013 *J. Chem. Phys.* **138** 044501
[22] Mitic S, Klumov B A, Konopka U, Thoma M H and Morfill G E 2008 *Phys. Rev. Lett.* **101** 125002
[23] Pustylnik M Y *et al* 2016 *Rev. Sci. Instrum.* **87** 093505
[24] Klein M, Dormagen N, Dietz C, Thoma M and Schwarz M 2024 *Mach. Learn.: Sci. Technol.* **5** 025050
[25] Knapek C A, Couedel L, Dove A, Goree J, Konopka U, Melzer A, Ratynskaia S, Thoma M H and Thomas H M 2022 *Plasma Phys. Control. Fusion* **64** 124006
[26] Himpel M and Melzer A 2021 *Mach. Learn.: Sci. Technol.* **2** 045019

Chapter 4

Publication III: Time-resolved classification of plasma crystals in a direct current discharge using an advanced graph neural network

Author Contributions

Niklas Dormagen

Conceptualization (lead)
Software (lead)
Data curation (lead), Investigation (lead), Validation (lead) and Visualization (lead)
Writing – original draft and revision

Max Klein

Data curation (supporting)
Writing – review and editing (supporting)

Andreas S. Schmitz and Lukas Wimmer

Data curation (supporting) and Methodology (supporting)
Writing – review and editing (supporting)

Markus H. Thoma and Mike Schwarz

Funding acquisition (lead)
Project administration (lead)
Writing – review and editing (supporting)

IOP Publishing Mach. Learn.: Sci. Technol. 6 (2025) 045016 https://doi.org/10.1088/2632-2153/ae13d0

MACHINE LEARNING
Science and Technology

OPEN ACCESS

RECEIVED
1 July 2025

REVISED
8 October 2025

ACCEPTED FOR PUBLICATION
15 October 2025

PUBLISHED
27 October 2025

PAPER

Time-resolved classification of plasma crystals in a direct current discharge using an advanced graph neural network

N Dormagen[1,2,*], **M Klein**[1,2], **A S Schmitz**[1], **L Wimmer**[1], **M H Thoma**[1] **and M Schwarz**[2]

[1] I. Institute of Physics, Justus Liebig University, Giessen D 35392, Germany
[2] NanoP, THM University of Applied Sciences, Giessen D 35390, Germany
[*] Author to whom any correspondence should be addressed.

E-mail: niklas.dormagen@nanop.thm.de

Keywords: complex plasma, plasma crystals, Coulomb crystals, DC plasma, image analysis, convolutional neural networks, graph neural network

Abstract

The formation and classification of crystalline structures in complex plasmas is an interesting topic in plasma physics, particularly under dynamic conditions such as microgravity. While previous work has largely focused on well-ordered cubic structures, the identification of more complex symmetries remains challenging, especially in noisy experimental data. In this study, we present an SE(3)-equivariant graph neural network capable of classifying a broad range of plasma crystal symmetries, including face-centered cubic, hexagonal close-packed, body-centered cubic, face-centered orthorhombic, body-centered orthorhombic, and body-centered tetragonal. SE(3) denotes the Special Euclidean group in three dimensions, comprising all rotations and translations. SE(3) Transformers use attention-based, equivariant message passing on graphs so that learned features (scalars, vectors, higher-order tensors) respect 3D symmetry. This property is crucial for classifying crystals because orientation and translation should not change the predicted class. Our model combines equivariant message passing with Voronoi-based shape descriptors to capture both local geometric features and global symmetries. It is trained on synthetic datasets and validated against experimental data from PK-4 under laboratory and microgravity conditions. The network significantly outperforms previous approaches such as WignerNet_PointNet, particularly on non-cubic structures. Time-resolved analysis reveals how crystal formation depends sensitively on external parameters such as gas pressure and polarity-switching frequency. Under microgravity, crystalline phases appear less frequently, which we attribute to reduced particle compression and altered spatial confinement. Overall, the results highlight the effectiveness of symmetry-aware machine learning models in capturing structural complexity in physical systems. The method enables accurate classification of ordered structures and provides a powerful tool for investigating phase behavior in complex plasmas.

1. Introduction

Plasmas, which consist of freely moving electrons and ions, are ionized gases and an interesting medium for studying interactions in strongly coupled systems. When dust-sized micro-particles are introduced into these plasmas, they become negatively charged by capturing electrons and form so-called complex plasmas [1]. In such systems, the micro-particles interact through a combination of repulsive forces, described by the Yukawa potential, and attractive forces arising from ion flow-induced wake effects. These interactions can lead to the arrangement of the particles into ordered crystalline structures, commonly referred to as Coulomb or plasma crystals [2–6]. Previous studies on plasma crystals have focused primarily on the identification of known crystalline structures such as face-centered cubic (fcc), body-centered cubic (bcc) and hexagonal close-packed (hcp) [7–9]. Additionally, face-centered

orthorhombic (fco) structures have been observed by Takahashi and Totsuji [10], particularly in cylindrical DC discharge plasmas. However, other potentially relevant configurations, such as body-centered orthorhombic (bco) and body-centered tetragonal (bct), have not been explicitly investigated in these experiments. This raises the question of whether such structures might also form under certain conditions and how they could be identified within experimental data. Inspired by the observations of Takahashi and Totsuji [10] and by studies focused on the detection of various crystalline structures [11, 12], our study introduces a machine learning approach capable of identifying and classifying a wider range of crystalline structures. By extending the training data with structures such as fco, bco and bct, we aim to train an advanced neural network to classify fco, bco and bct in addition to fcc,bcc and hcp, thus extending the possibilities of structural analysis in complex plasmas. The advanced model is based on the SE(3) transformer architecture [13–16], which offers a fundamental advantage over networks used in our previous work [17], such as PointNet [18] or PointNet++ [19]. In contrast to PointNet-based methods, the SE(3) transformer works directly with graphical representations of Wigner–Seitz cells and can therefore work more efficiently and stable in the case of invariants. This is because the SE(3) transformer is fundamentally equivariant, which is particularly advantageous for structures such as bco, bct and fco, as their edge length ratios can vary considerably [13, 16].

The PK-4 facility [20], designed to study complex plasmas in cylindrical DC discharges under both terrestrial and microgravity conditions, serves as the main source of experimental data for this study. To further investigate the formation and evolution of plasma crystals, we performed experiments to observe their behavior under normal gravitational conditions in a laboratory setting. By analyzing the time-dependent evolution of these structures, we gained insight into their stability and transition dynamics. Moreover, to examine plasma crystal formation in microgravity, we conducted experiments as part of a parabolic flight campaign. The aim of these experiments was to investigate how the absence of gravitational forces affects the self-organization of dust particles into crystalline structures.

By applying the advanced neural network to synthetic and experimental data sets from PK-4 experiments, we confirm that we can detect not only known structures such as fcc, bcc and hcp, but also structures such as fco, bco and bct. With this work, we aim to extend the range of crystalline structures that can be detected in complex plasmas and gain deeper insights into the formation mechanisms of plasma crystals. This approach paves the way for further potential investigations in the context of complex plasmas.

2. Method

To accurately analyze crystalline structures, it is important to reconstruct their three-dimensional arrangement as precisely as possible. In the PK-4 setup, this is achieved by scanning the particle cloud along the Y-axis with a laser and camera system mounted on a motorized stage. The stage moves at a speed of 0.5 mm s^{-1}, while the camera captures images at 60 fps. This process ensures that each particle is captured multiple times. By linking the particle positions in sequential images, the three-dimensional coordinates of each individual particle can be reconstructed. For particle localization, we applied a U-Net-based method [17, 21], and the trajectories were tracked through the image sequence using an adapted self-organizing map [22]. The Y-coordinates of the particles were assigned based on the stage's position during the scan, while the X and Z positions were extracted from the two-dimensional image data. These coordinates can be combined to generate a three-dimensional point cloud, which serves as the basis for further structural analyses.

A major challenge in this process is the remaining motion of the particles, which introduces noise into the data and complicates the analysis. To solve this problem, the particle neighborhoods are first defined using Delaunay triangulation, followed by the calculation of Voronoi cells. This dual approach provides a robust representation of local structures and is particularly beneficial for analyzing systems with coexisting crystalline and amorphous regions [23].

The structural analysis relies on Voronoi cells, calculated using the SCIPY [24] implementation of QHull [25]. Maintaining the three-dimensional characteristic of the data is crucial for accurate classification, so we use Wigner–Seitz cells as the basis for structure identification (see figure 1). A Wigner–Seitz cell denotes the region of space that is closer to a given particle than to any other. Visually, it corresponds to the Voronoi cell of that particle within the crystal lattice. The shape of a Wigner–Seitz cell is highly characteristic of a particular crystal structure and allows for a clear distinction from other structures. This representation provides a geometric framework for a detailed analysis of the crystalline structure using a graph neural network.

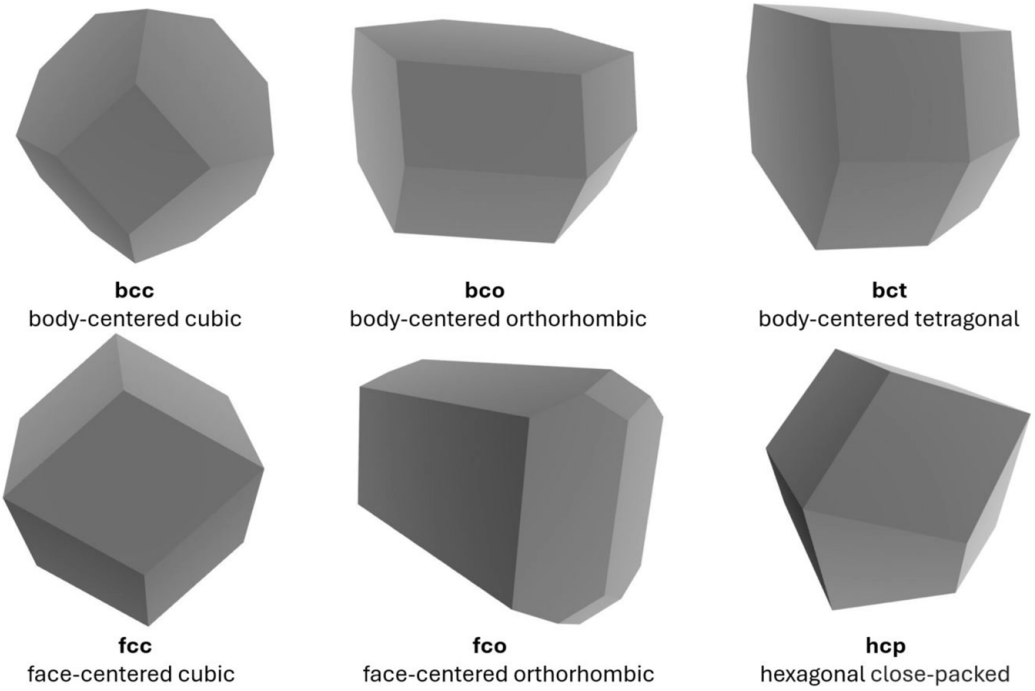

Figure 1. Three-dimensional view of the Wigner–Seitz cells of the bcc, bco, bct, fcc, fco, and hcp structures.

In this study, we improve the methodology by replacing the previous PointNet architecture [17] with the more advanced SE(3) transformer [13], which we have implemented in PyTorch [26]. In contrast to the PointNet-based approach [17], which requires point cloud representations with 1000 points per Wigner–Seitz cell, the SE(3) transformer directly processes the Voronoi graphs derived from the neighborhood determination. This significantly reduces computational effort while retaining the essential geometric information. A key advantage of the SE(3) transformer is its equivariance. This ensures that structural variations caused by differences in unit cell parameters do not affect classification performance. This is particularly important for structures such as bco, bct, and fco, where edge length ratios vary dynamically. The network operates using SE(3)-equivariant message-passing layers, which propagate and aggregate structural information efficiently while maintaining geometric consistency across transformations.

Following the approach of Dietz *et al* [8], we limit our analysis to identifying the crystalline structure of particles. To exclude disordered particles, we apply a modified scalar product of the bond-orientational order parameter [27, 28], adapted to the Minkowski structure metric (MSM) [29]. This method is robust against positional uncertainties of up to 14% of the nearest neighbor distance, effectively accounting for oscillations during the scanning process [29]. By integrating the SE(3) transformer into our analysis pipeline, we introduce a highly efficient and accurate classification network that expands the detection and classification capabilities for ordered structures in the context of complex plasmas.

2.1. Equivariant graph neural network framework

Our neural network builds on the crystal edge graph attention neural network (CEGANN) proposed by Banik *et al* [14], which was originally developed for crystal classification in atomistic simulations. In this framework, crystalline structures are represented as graphs in which the nodes correspond to particles and the edges describe their local neighborhoods. Information is exchanged between nodes through an attention-based message passing mechanism, so that each particle updates its representation based on both its own properties and those of its neighbors. The symmetry-awareness of this network is essential for the classification of experimental plasma crystal data, where orientations are arbitrary and noisy. In our adaptation of the CEGANN framework, each particle is described by a combination of scalar features, such as Voronoi cell volume and surface area, and directional features derived from the relative positions of neighboring particles. During message passing, these features are iteratively aggregated

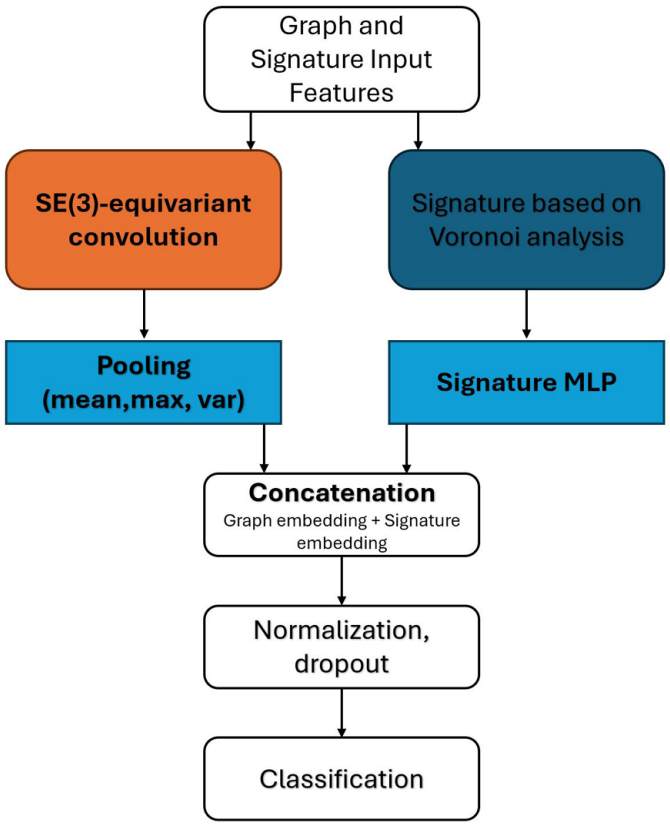

Figure 2. This is a schematic representation of the neural networks architecture.

across the graph, allowing the model to capture both local geometric details and global lattice symmetries. Intuitively, this process enables the network to learn how crystalline order emerges from the interactions between particles in their immediate environment. While this general framework provides robust symmetry-aware message passing, our model extends it with a global structural signature that captures complementary information beyond local neighborhoods.

2.2. Model architecture

While we adopt the general design principles of CEGANN [14], our model introduces an important extension in the form of a global *signature* vector (see figure 2).

This signature is derived from Voronoi-based structural descriptors, including MSMs, higher-order anisotropy measures, and coordination numbers. These descriptors are invariant under rotation and translation and thus provide complementary information to the local, equivariant message passing. By combining both perspectives, the model achieves a more robust discrimination between structurally similar phases such as fco and bco. To enrich the model with global geometric context, we integrate a signature derived from a Voronoi-based structural analysis [30]. This signature includes geometric descriptors based on the MSM and higher-order shape metrics. For each particle, a local Voronoi cell is constructed. The total surface area A of the cell is computed as the sum of its facet areas:

$$A = \sum_{f \in F(i)} A(f). \tag{1}$$

This quantity is then defined as the total surface area of the Voronoi cell boundary $F(i)$ of sphere i.

The MSM of Mickel *et al* [23, 31] is calculated as follows:

$$q'_{lm} = \sum_{f \in F(i)} \frac{A(f)}{A} Y_{lm}(\theta_f, \phi_f), \quad q'_l = \sqrt{\frac{4\pi}{2l+1} \sum_{m=-l}^{l} |q'_{lm}|^2}. \tag{2}$$

The parameter $q_l^{'}$ is the second order rotational invariant and is calculated for $l = 4, 6$. Following Steinhardt *et al* [32], we evaluate q_l for $l = 4, 6$, as these bond-orientational invariants are the most effective for distinguishing different types of local order. We also compute the third-order rotational invariant $w_l^{'}$ based on the MSM [33]:

$$w_l'(i) = \sum_{\substack{m_1,m_2,m_3 \\ m_1+m_2+m_3=0}} \begin{pmatrix} l & l & l \\ m_1 & m_2 & m_3 \end{pmatrix} \frac{q'_{lm_1}(i)\, q'_{lm_2}(i)\, q'_{lm_3}(i)}{\left(q_l'(i)\right)^3}, \tag{3}$$

where the indices m_1, m_2, m_3 are subscripts on $q_{lm'}$ and the parenthetical term is the Wigner 3j symbol. Another component of the signature is given by the six eigenvalues $\zeta_1, \ldots, \zeta_6$ of a fourth-order Minkowski tensor, which quantify the anisotropy and asymmetry of the local cell shape [34]. In addition, the coordination number N, defined as the number of nearest neighbors, is included as a further descriptor. These global descriptors are invariant under rotation and translation [34].

The architecture itself consists of several equivariant graph convolutional layers, which update particle features while preserving geometric consistency. The resulting node embeddings are pooled to obtain a graph-level representation of the structure. This representation is then concatenated with the global signature vector and processed through a multilayer perceptron with normalization, dropout, and a final softmax classifier. The architecture is implemented using PyTorch Geometric [26] with the e3nn library [35] to ensure SE(3)-equivariance. In this way, the network integrates local, symmetry-preserving interactions with global geometric context, enabling accurate classification of crystalline structures in complex plasmas even under noisy and dynamic experimental conditions. In the following, we describe the dataset generation and training strategy that enable the network to generalize to experimental conditions.

2.3. Training of the SE(3)-transformer model

To train the SE(3) transformer, we created a synthetic data set with crystalline structures, which allows a controlled variation of the noise levels and thus ensures reproducibility. The dataset covers the six crystalline symmetries fcc, hcp, bcc, fco, bco, and bct, each generated algorithmically by filling a three-dimensional volume with particles arranged according to the respective lattice geometry.

To emulate experimental conditions, Gaussian noise was added to the particle coordinates to simulate Brownian motion. The noise amplitude was varied from $0.01a$ to $0.2a$ in steps of $0.01a$, where a denotes the average nearest-neighbor distance. For anisotropic lattices (fco, bco, bct), the lattice constants a, b and c were randomly varied to increase structural diversity. Each structure was also subjected to transformations, such as scaling and rotation, to introduce geometric variability and improve the generalization of the model. For each noise level, 80 different realizations were generated for these lattice types.

We focus exclusively on identifying the crystal structure of individual particles, without explicitly distinguishing between solid and disordered states. To exclude disordered particles, as described by Dietz *et al* [30], we use a modified scalar product of BOOPs [27, 28], which can also be defined analogously for MSM [29]:

$$S(i) = \frac{1}{N} \sum_{j=1}^{N} \sum_{m=-6}^{6} \tilde{q}'_{6m}(i)\, \tilde{q}'^{*}_{6m}(j) \tag{4}$$

$$\tilde{q}'_{6m}(i) = \frac{q'_{6m}(i)}{\left(\sum_{m=-6}^{6} |q'_{6m}(i)|^2\right)^{1/2}}. \tag{5}$$

The number of neighbors is denoted by N, and the scalar product is averaged over all neighbors j. This procedure enables us to define a single threshold for each particle i to determine whether it is in the solid or the disordered phase. In our case, we classify a particle as solid if $S(i) \geqslant 0.55$, which provides the most reliable distinction. Wigner–Seitz graphs were constructed from these solid particles.

In total, the dataset comprised approximately 82,356 training samples, 16 791 validation samples, and 16 941 test samples. Due to SE(3)-equivariance, rotation augmentation is not necessary for convergence. However, we apply mild rotations during validation and testing to probe invariance beyond the training conditions. All data were converted to graph representations compatible with PyTorch Geometric.

The SE(3)-Transformer was trained using the AdamW optimizer with a weight decay of $\lambda = 10^{-3}$ to avoid overfitting. The initial learning rate was set to $\alpha_0 = 0.0005$ and reduced by a factor of 0.5 every 50 epochs:

$$\alpha_{\text{epoch}} = \alpha_0 \cdot 0.5^{\lfloor \text{epoch}/50 \rfloor}. \tag{6}$$

In addition, a ReduceLROnPlateau [26] scheduler was used to dynamically adapt the learning rate, reducing it by a factor of 0.5 if the validation loss plateaued for five consecutive epochs. To further mitigate overfitting, early stopping with a patience of 20 epochs was employed, and the model checkpoint with the lowest validation loss was kept. Training was carried out using the PyTorch [26] implementation of negative log-likelihood (NLL) loss function:

$$\mathcal{L}_{\text{NLL}} = -\sum_{i=1}^{C} y_i \log \hat{y}_i, \tag{7}$$

where y_i is the true one-hot encoded class label, $\hat{y}_i$ the predicted class probability, and C the number of lattice classes. Gradient clipping with a maximum norm of 5 was applied to avoid exploding gradients. Additionally, dropout regularization was employed before the final classification layer to enhance generalization.

2.4. Model performance

To evaluate the effectiveness of our proposed model, we conducted a systematic comparison against both graph-based methods and widely used atomic descriptors in computational materials science. For clarity, we will refer to our network consisting of CEGANN + Signature as PlasmaCrystalNet from here on out. SE(3)-equivariant networks, as implemented in `e3nn`, have proven effective for modeling atomic structures. However, a broad class of descriptors has also been successful for crystal classification. These include the Smooth Overlap of Atomic Positions (SOAPs), Atom-Centered Symmetry Functions (ACSFs) [36], and many-body tensor representations such as the Local Many-Body Tensor Representation (LMBTR) and the global MBTR [37]. Incorporating these methods into our comparison provides a comprehensive assessment of how our model performs relative to established descriptors. For this purpose, we considered the following approaches:

- SE(3)-equivariant GNN with Voronoi-based signature (`PlasmaCrystalNet`);
- `CEGANN` [14];
- `WignerNet_PointNet` [9];
- `SOAP` [38];
- `LMBTR` [38];
- `MBTR` [37, 38];
- `ACSF` [36, 38].

All descriptor-based methods were implemented using the DScribe library [38] and trained on the same dataset as the SE(3)-equivariant models. Performance was evaluated using F1 scores. The results are summarized in figure 3.

GNN models demonstrate superior performance in low-noise scenarios across the entire noise range. PlasmaCrystalNet maintains a Macro-F1 value of at least 0.9 even in the mid-noise regime, making it the most robust option overall. CEGANN also starts close to unity, but it exhibits a pronounced collapse once the noise level approaches ∼16–18. Among the descriptors, SOAP smoothly degrades and ultimately overtakes CEGANN at high noise levels. Meanwhile, LMBTR and ACSF steadily decline from approximately 0.7–0.8 toward ∼0.45. MBTR remains low and almost flat around ∼0.35 across all noise levels. WignerNet_PointNet performs well at low noise (∼0.8) but shows the strongest decay, reaching very low F1 in the highest-noise range.

PlasmaCrystalNet likely benefits from geometry-aware aggregation that keeps neighborhood information stable under small coordinate perturbations, whereas CEGANN appears to rely more on fine local features whose topology becomes unreliable at high noise, triggering the late collapse.

As shown in figure 4, there are two regimes in the F1-latency plot that are separated by nearly two orders of magnitude in runtime. Descriptor-based methods (MBTR, ACSF, LMBTR, SOAP) operate in the tens of microseconds, while PlasmaCrystalNet, CEGANN and WignerNet_PointNet cluster around ∼1 ms. Considering both F1-score and latency, PlasmaCrystalNet offers the best trade-off (F1 ≈ 0.99 at ∼1 ms); CEGANN is comparably fast yet marginally less accurate. Among methods operating in the tens of microseconds, SOAP stands out with markedly higher F1 while maintaining similar latency to LMBTR/ACSF. WignerNet_PointNet sits mid-latency but underperforms both SOAP and CEGANN/PlasmaCrystalNet. These findings demonstrate that our PlasmaCrystalNet, enriched with a global signature, is more robust and generalizes better than the baseline CEGANN and conventional

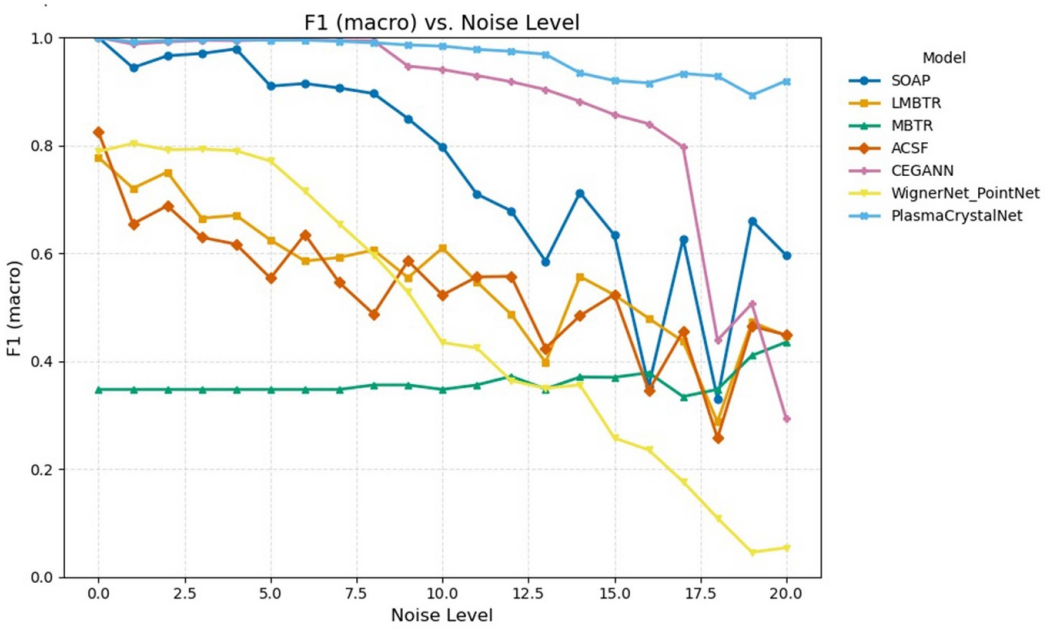

Figure 3. Macro-F1 score as a function of noise level for seven models.

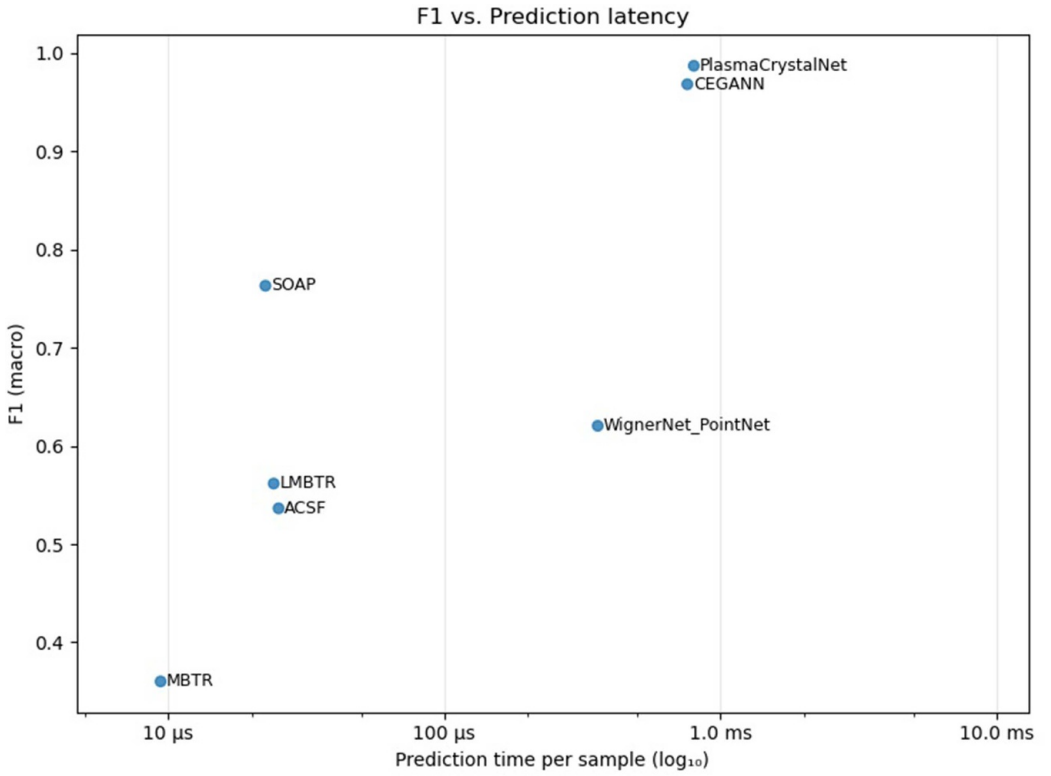

Figure 4. F1-latency trade-off for all methods. Each marker reports macro-F1 (y-axis) versus per-sample prediction time (x-axis; per Wigner–Seitz cell) on a $\log_{10}$ scale.

atomic descriptors. The model achieves accurate discrimination of structurally complex crystalline phases by combining local, symmetry-preserving message passing with invariant global shape descriptors. This extends the applicability of equivariant graph neural networks to noisy experimental plasma data, which is past the limits of other descriptors.

Table 1. Experimental settings with measurements conducted at pressures of 40, 60, 80, and 100 Pa, at frequencies of 500 Hz and 1000 Hz. Measurements were taken in 1 min intervals over a 5 min period. All experiments were conducted in neon.

No.	Pressure (Pa)	Frequency (Hz)	Measurement intervals (min)
1	40	500	0, 1, 2, 3, 4, 5
2	60	500	0, 1, 2, 3, 4, 5
3	80	500	0, 1, 2, 3, 4, 5
4	100	500	0, 1, 2, 3, 4, 5
5	40	1000	0, 1, 2, 3, 4, 5
6	60	1000	0, 1, 2, 3, 4, 5
7	80	1000	0, 1, 2, 3, 4, 5
8	100	1000	0, 1, 2, 3, 4, 5

3. Experimental setup

The experiments were carried out with the engineering model (EM) of the PK-4 system, whose design and operation have already been described in detail in [20] and in our previous work [9].

The EM is largely identical to the Science Reference Model used on the ISS and was employed both for laboratory studies and for experiments during a parabolic flight campaign. For the present study, the main difference compared to the Science Reference Model is the use of a high-resolution xiQ camera (2048×2048 pixels, up to 90 fps) instead of the CCD camera, which enabled a more precise analysis of particle structures. In addition, we performed systematic time-resolved measurements under normal gravity as well as under microgravity conditions during the 44th DLR parabolic flight campaign. The microparticles were illuminated with a 532nm laser. The images were captured at a frame rate of 60 fps and a scanning speed of 0.5 mm s^{-1}. In each experiment, the plasma chamber was scanned systematically along the Y-axis, covering a range from 10.5 mm to 18 mm. Further technical information on the gas flow, electrode configuration, and optical diagnostics can be found in [20, 39] and [9].

3.1. Laboratory experiments

In addition to microgravity experiments, extensive investigations were conducted under normal gravity conditions in the laboratory at JLU Giessen using the EM of PK-4. To analyze the temporal evolution of plasma crystals, we performed time-resolved measurements, scanning the microparticle cloud every minute over a period of five minutes under various plasma conditions. Specifically, we examined the evolution of plasma crystals at pressures ranging from 40 Pa to 100 Pa, conducting measurements at each pressure for both 500 Hz and 1000 Hz polarity-switching frequencies. The discharge current was maintained at 1 mA, and neon was used as working gas. For the formation of complex plasma, monodisperse melamine-formaldehyde (MF) microparticles with a diameter of 3.4 μm were injected into the plasma. After ignition of the discharge, particles were injected after 20 s and measurements were started once the cloud was centered in the camera field of view. Each dataset corresponds to image sections containing approximately 4000–8000 particles. Between changes of plasma parameters, a 3 min pause ensured stabilization of gas flow and wall temperature. The measurement conditions are summarized in table 1. To investigate the influence of external parameters on the formation of crystalline structures in complex plasmas, a systematic comparison was performed by varying the gas pressure (40–100 Pa) and the DC polarity-switching frequencies (500 Hz and 1000 Hz) (see table 1). The results show clear trends in the arrangement of ordered structures under different environmental conditions (see tables 2 and 3).

At constant switching frequency, lowering the neutral gas pressure reduces collisional damping and enhances the directed ion drift. This does not simply destabilize the order; rather, it redistributes it: closed-packed structures (fcc, hcp) shrink, while field-aligned anisotropic order becomes more likely. In particular, increased fractions of bct and bco (with occasional fco) can be observed at lower pressures (40–60 Pa), while at 100 Pa the fraction of close-packed fcc/hcp is highest. Orthorhombic/tetragonal phases (bco/bct/fco) are therefore favored when ion–wake anisotropy is strong; conversely, at high pressure they are suppressed and fcc/hcp dominate. The excitation frequency also has a significant influence. A comparison of 500 Hz and 1000 Hz measurements under identical pressure conditions shows that at higher polarity-switching frequency, the overall number of ordered particles is reduced and the temporal evolution of crystalline order is weaker. The difference cannot be explained by the direct response of the particles to the switching field, as the frequency is far above the characteristic dust response time. Instead, higher switching frequencies affect the ion flow and the formation of ion wakes, which provide vertical alignment and stabilize lattice order. Moreover, PK-4 discharge is known to exhibit ionization waves with a characteristic period of $\sim$50 μs [40], whose properties depend on pressure [41]. At

Table 2. Structural data for all measurements at 500 Hz. Entries denote the number of particles classified as the respective structure in that minute and condition.

Pressure (Pa)	Min	fcc	hcp	bcc	fco	bco	bct	Total
100	1	65	51	16	3	2	1	138
	2	101	65	19	3	2	2	192
	3	69	40	10	2	3	1	125
	4	58	32	8	2	2	1	103
	5	24	13	3	1	1	0	42
80	1	16	12	4	2	3	6	43
	2	78	62	23	12	21	35	231
	3	165	130	50	30	45	80	500
	4	27	21	8	5	7	13	81
	5	22	17	6	4	6	9	64
60	1	8	7	3	3	5	10	36
	2	33	27	14	13	26	46	159
	3	14	11	6	6	11	19	67
	4	0	0	0	0	0	1	1
	5	0	0	0	0	0	1	1
40	1	0	0	0	0	0	0	0
	2	1	0	0	1	1	2	5
	3	1	1	0	1	2	4	9
	4	1	1	1	1	2	5	11
	5	1	0	0	1	2	4	8

Table 3. Structural data for all measurements at 1000 Hz. Entries denote the number of particles classified as the respective structure in that minute and condition.

Pressure (Pa)	Min	fcc	hcp	bcc	fco	bco	bct	Total
100	1	6	4	1	0	0	0	11
	2	13	7	1	0	0	0	21
	3	20	11	2	0	0	0	33
	4	19	9	2	0	0	0	30
	5	3	1	0	0	0	0	4
80	1	12	9	3	0	1	2	27
	2	12	8	3	0	1	2	26
	3	10	7	2	0	1	2	22
	4	13	9	3	1	1	2	29
	5	0	0	0	0	0	0	0
60	1	20	16	7	3	6	10	62
	2	6	4	2	1	2	2	17
	3	2	1	1	0	1	1	6
	4	4	3	2	1	1	2	13
	5	8	6	2	1	2	3	22
40	1	1	1	0	0	1	2	5
	2	1	1	1	0	1	2	6
	3	2	2	1	1	2	4	12
	4	9	7	4	3	7	17	47
	5	4	3	1	1	3	7	19

higher switching frequencies, ion wakes are suppressed and the coupling to ionization waves is altered, which weakens long-range ordering and explains the reduced stability of bco and bct lattices observed at 1000 Hz. A particularly robust trend at reduced pressure is the persistence of anisotropic lattices. At reduced pressure (40–60 Pa), bct (with substantial bco) becomes the most frequent ordered state. fco can occur but is typically less frequent. In contrast, fcc/hcp require higher pressure to form and remain stable. Under less favorable conditions, namely low pressure, they either do not form at all or dissolve quickly after formation. Regardless of the external parameters, most experiments show a moderate increase in the number of ordered structures during the first minutes, which typically reaches a

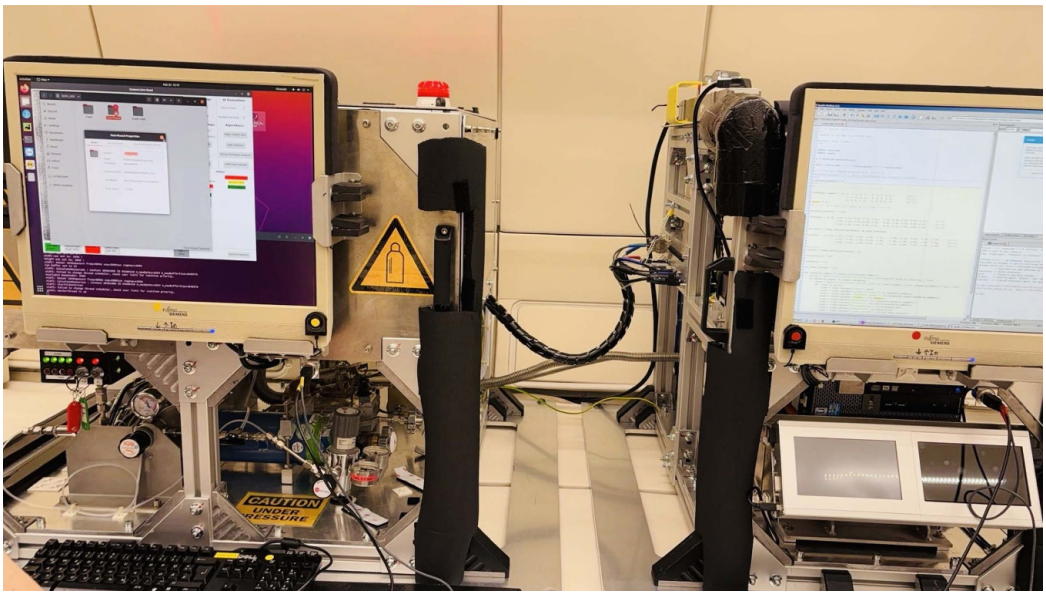

Figure 5. The engineering model (EM) of PK-4 installed on board the parabolic flight aircraft.

maximum after two to three minutes. Under optimal conditions, i.e. at high pressure and low polarity-switching frequency, this growth continues steadily, while under less favorable conditions the number of ordered structures stagnates or decreases again after the initial increase. A possible explanation for this temporal behavior can be found in the intrinsic plasma dynamics of the PK-4 discharge. As shown by Hartmann *et al* [40], the plasma column is not stationary but dominated by fast ionization waves and associated striations. These generate strong spatio-temporal fluctuations of electric fields and particle densities, resulting in residual drifts and variations in the kinetic temperature of the microparticles. Consequently, even when ordered phases form initially, they can dissolve again after a few minutes as the cloud experiences periodic perturbations from the background plasma. In addition, Mitic *et al* [42] demonstrated that the long-term structural evolution in PK-4 is strongly influenced by a gradual redistribution of microparticles within the cloud. This implies that the observed time dependence of crystalline order reflects not only collisional damping and external control parameters, but also the combined effects of the oscillatory plasma dynamics and the slow rearrangement of particles within the discharge. The observed structural behavior also reflects the overall dynamics of the cloud. At lower pressures, the particles retain higher drift velocities and exhibit an increased kinetic temperature, both of which hinder the formation of ordered structures. At higher pressure and lower polarity-switching frequency, the cloud approaches a quasi-equilibrium state with reduced drift and lower kinetic temperature, which promotes long-range order. These correlations suggest that the balance between collisional damping, ion-wake stabilization, and residual drift plays a central role in determining the crystalline order in laboratory plasmas.

3.2. Microgravity experiments on parabolic flights

As part of the 44th DLR parabolic flight campaign, a series of experiments were carried out under microgravity conditions with the support of Novespace [43] (see figure 5). Each flight consisted of 31 parabolas, providing approximately 22 s of microgravity per parabola. Due to the limited duration of each phase, the procedures were highly automated to ensure reliable operation and efficient data collection.

The main objective was to investigate the behavior of microparticle clouds in microgravity. The experiments were carried out in neon at pressures of 50, 60 and 70 Pa with a switching frequency of 500 Hz, ensuring consistency with the laboratory studies. The discharge current was kept constant at 1 mA. Monodisperse MF microparticles with a diameter of 3.4 μm were injected into the plasma. Due to time constraints, only one scan per parabola could be performed. Before each scan, the particles were confined within the camera's field of view and stabilized for 3 s, during which an algorithm dynamically

Table 4. Structural data for all measurements under microgravity. Entries denote the number of particles classified as the respective structure.

Pressure (Pa)	Experiment	fcc	hcp	bcc	fco	bco	bct	Total
70	1	0	0	0	1	2	1	4
	2	0	0	0	2	4	1	7
	3	1	0	2	2	7	3	15
	4	0	0	0	0	0	0	0
60	1	0	0	0	0	2	0	2
	2	0	0	0	0	0	0	0
	3	0	0	0	0	0	0	0
	4	0	0	0	1	2	0	3
50	1	0	0	0	0	0	0	0
	2	0	0	0	0	0	0	0
	3	0	0	0	0	0	0	0
	4	0	0	0	0	0	0	0

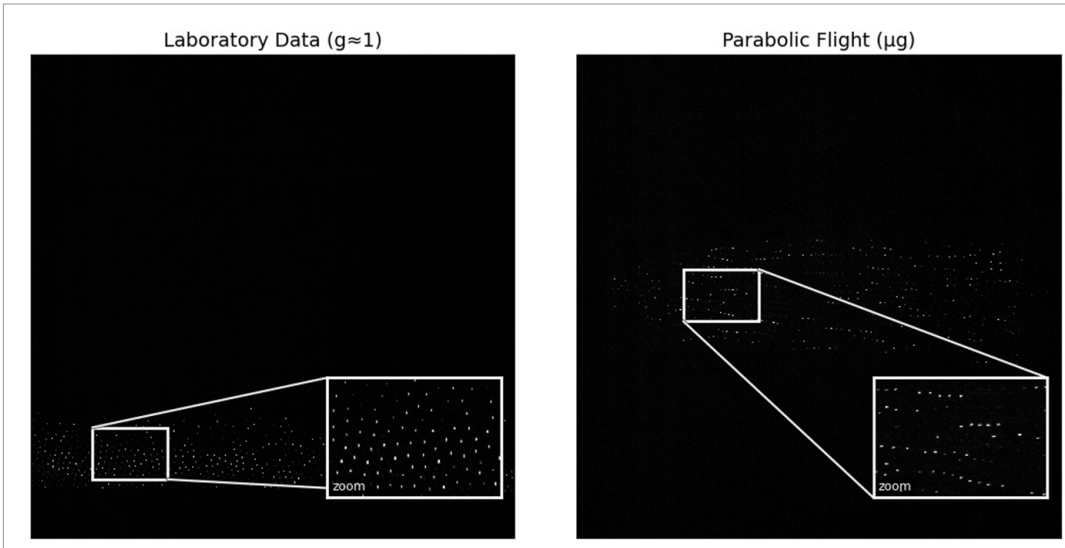

Figure 6. Representative images comparing normal gravity (left) and microgravity (right). Under microgravity, the particle cloud is no longer pressed into the plasma sheath but instead occupies the central region of the discharge tube.

adjusted the duty cycle of polarity switching to minimize residual drift. A particle cloud typically contained 2000–4000 particles. The lower particle count compared to laboratory experiments is likely due to the dispensers used. After each parabola, the system was flushed to remove the remaining particles and allow for a fresh injection in the next microgravity phase. In this way, the measurements were directly comparable to those obtained under normal gravity.

Crystalline structures were only rarely observed (see table 4). Across all parabolas, we detected **17** *bco*, **6** *fco*, **5** *bct*, **2** *bcc*, and **1** *fcc* structures. Despite the limited availability of data, our findings consistently indicate that field-aligned anisotropic phases (*bco*, *bct*, *fco*) occur more often than close-packed phases (*fcc*, *hcp*). At 70 Pa, an increase in neutral damping leads to the formation of anisotropic clusters, while at lower pressures, no ordered structures were detected. Due to the overall low crystallization rate, it is not possible to draw definitive conclusions on phase stability. In contrast, linear chain-like arrangements aligned with the discharge axis were observed frequently, were remarkably stable, and recurred across multiple parabolas. This behavior is consistent with Takahashi and Totsuji [10], who reported that under microgravity crystalline order (*fco*) dissolves shortly after onset and is replaced by one-dimensional chains stabilized by wakefield interactions and anisotropic coupling.

Another difference from laboratory conditions is the spatial distribution of particles (see figure 6). In microgravity, the cloud is found in the center of the tube instead of being compressed into the lower sheath; the reduced particle density lowers the effective coupling parameter Γ and thus the propensity to

crystallize—consistent with laboratory observations where increased pressure and compression promote crystal formation [44]. Consequently, extended crystalline domains are favored in the laboratory but are strongly suppressed in microgravity.

Overall, ordered phases were less stable under microgravity than under laboratory conditions, while string-like structures dominated. Notably, our graph neural network enables the identification of these short-lived crystalline states even in such dynamic, non-stationary environments.

Increasing the number of injected particles is a plausible way to enhance the probability of crystallization because higher density strengthens interparticle interactions and promotes compression.

4. Conclusion

We presented `PlasmaCrystalNet`, a graph neural network that combines SE(3)-equivariant message passing with a global, Voronoi-based signature, enabling reliable classification of six crystalline phases in complex plasmas with millisecond latency per Wigner–Seitz cell. Across a comprehensive benchmark, the model maintains high macro-F1 at low to mid noise and outperforms descriptor-based methods and a PointNet method while remaining computationally efficient for real-time analysis. Time-resolved laboratory measurements show that the phase transition to crystalline order is maximized at high pressure and a moderate polarity switching frequency. At reduced pressure, *bct*/*bco* phases become more prevalent, consistent with stronger ion-wake anisotropy. Under microgravity, string-like arrangements dominate and crystal structures appear only sporadically, reflecting reduced compression. Together, these results provide a reliable method for recognizing structures in PK-4 and demonstrate how discharge control parameters influence the formation of ordered structures.

It should be noted that this study uses 2D camera projections and minute-by-minute scans, which may not fully capture transient rearrangements. Furthermore, statistics on parabolic flights are limited, and the labels for rare classes are subject to greater uncertainty. Finally, the evaluation is limited to neon and a current of 1 mA. Further studies should be conducted with other gases and currents.

Enlarged datasets that cover additional noble gases, discharge currents, and microgravity campaigns will enable phase occurrence maps and tests of string—crystal transition theories. Higher-resolution and stereoscopic imaging, as in the COMPACT setup [45], should allow tracking structural dynamics with improved precision [46, 47].

Computational resources for training

All neural models were trained on an in-house cluster equipped with 2× NVIDIA RTX 3080 (CUDA-enabled) and 60 GB RAM. Unless stated otherwise, experiments were executed on a single GPU; the second GPU was used to accelerate hyper-parameter sweeps and repeated runs. The reported results are reproducible on a single RTX 3080 without architectural changes. Importantly, the full training pipeline also runs on an embedded NVIDIA Jetson AGX Orin. On this platform, training remains feasible by using smaller micro-batch sizes; no modifications to the network architecture or loss functions are required. As expected for embedded hardware, training time increases, but convergence behavior and final accuracy are unaffected.

Data availability statement

The code is available on GitHub via https://github.com/plasmalyzer/PlasmaCrystalNet. All data that support the findings of this study are included within the article (and any supplementary files).

Acknowledgment

This work is supported by the German Aerospace Agency (DLR). We thank the research group around Markus H Thoma and M Kretschmer at Justus Liebig University Giessen for providing the data used in this study and the German Aerospace Society for providing powerful PCs in accordance with the funding decision, which facilitated the studies. This Project was supported by the

German Federal Ministry of Economic Affairs and Climate Action under Contract No. 50WK2270B.

Supported by:

on the basis of a decision
by the German Bundestag

Author contributions

N Dormagen 0009-0001-9158-4034
Conceptualization (lead), Data curation (lead), Investigation (lead), Software (lead), Validation (lead), Visualization (lead), Writing – original draft (lead)

M Klein 0009-0009-9596-7671
Data curation (supporting), Writing – review & editing (supporting)

A S Schmitz
Data curation (supporting), Writing – review & editing (supporting)

L Wimmer 0009-0008-8970-8203
Methodology (supporting), Writing – review & editing (supporting)

M H Thoma
Funding acquisition (lead), Project administration (lead), Writing – review & editing (supporting)

M Schwarz
Funding acquisition (lead), Project administration (lead), Writing – review & editing (supporting)

References

[1] Morfill G E and Ivlev A V 2009 *Rev. Mod. Phys.* **81** 1353–404
[2] Thomas H, Morfill G E, Demmel V, Goree J, Feuerbacher B and Möhlmann D 1994 *Phys. Rev. Lett.* **73** 652–5
[3] Melzer A, Trottenberg T and Piel A 1994 *Phys. Lett. A* **191** 301–8
[4] Pieper J B, Goree J and Quinn R A 1996 *Phys. Rev. E* **54** 5636–40
[5] Zuzic M, Ivlev A V, Goree J, Morfill G E, Thomas H M, Rothermel H, Konopka U, Sütterlin R and Goldbeck D D 2000 *Phys. Rev. Lett.* **85** 4064–7
[6] Molotkov V I, Thomas H M, Lipaev A M, Naumkin V N, Ivlev A V and Khrapak S A 2015 *Int. J. Microgravity Sci. Appl.* **32** 320302
[7] Chu J H and Lin I 1994 *Phys. Rev. Lett.* **72** 4009–12
[8] Dietz C, Bergert R, Steinmüller B, Kretschmer M, Mitic S and Thoma M H 2018 *Phys. Rev. E* **97** 043203
[9] Dormagen N, Klein M, Schmitz A S, Wimmer L, Thoma M H and Schwarz M 2024 *Mach. Learn.: Sci. Technol.* **5** 045006
[10] Takahashi K and Totsuji H 2019 *IEEE Trans. Plasma Sci.* **47** 4213–8
[11] Leitherer A, Ziletti A and Ghiringhelli L M 2021 *Nat. Commun.* **12** 6234
[12] Zuo Y, Qin M, Chen C, Ye W, Li X, Luo J and Ong S P 2021 *Mater. Today* **51** 126–35
[13] Fuchs F B, Worrall D E, Fischer V and Welling M 2020 SE(3)-transformers: 3D roto-translation equivariant attention networks *Preprint* (arXiv:2006.10503)
[14] Banik S, Dhabal D, Chan H, Manna S, Cherukara M, Molinero V and Sankaranarayanan S K R S 2023 *npj Comput. Mater.* **9** 23
[15] Yan K, Fu C, Qian X, Qian X and Ji S 2024 Complete and efficient graph transformers for crystal material property prediction *preprint* (arXiv:2403.11857)
[16] Lee S-H, Li J, Olevano V and Sklénard B 2024 *Phys. Rev. Mater.* **8** 033802
[17] Dormagen N, Klein M, Schmitz A S, Thoma M H and Schwarz M 2024 *J. Imaging* **10** 40
[18] Qi C R, Su H, Mo K and Guibas L J 2017 *Pointnet: Deep Learning on Point Sets for 3D Classification and Segmentation* (available at: https://arxiv.org/abs/1612.00593)
[19] Qi C R, Yi L, Su H and Guibas L J 2017 CoRR *Preprint* (arXiv:1706.02413)
[20] Pustylnik M Y *et al* 2016 *Rev. Sci. Instrum.* **87** 093505
[21] Ronneberger O, Fischer P and Brox T 2015 U-NET: convolutional networks for biomedical image segmentation *Preprint* (arXiv:1505.04597)
[22] Klein M, Dormagen N, Wimmer L, Thoma M H and Schwarz M 2025 *Mach. Learn. Knowl. Extr.* **7** 37
[23] Dietz C, Kretz T and Thoma M H 2017 *Phys. Rev. E* **96** 011301
[24] Virtanen P Contributors 2020 *Nat. Methods* **17** 261–72

[25] Barber C B, Dobkin D P and Huhdanpaa H 1996 *ACM Trans. Math. Softw.* **22** 469–83
[26] Paszke A *et al* 2019 Pytorch: an imperative style, high-performance deep learning library *Preprint* (arXiv:1912.01703)
[27] Rein ten Wolde P, Ruiz-Montero M J and Frenkel D 1996 *J. Chem. Phys.* **104** 9932–47
[28] Lechner W and Dellago C 2008 *J. Chem. Phys.* **129** 114707
[29] Steinmüller B, Dietz C, Kretschmer M and Thoma M H 2017 *Phys. Plasmas* **24**
[30] Dietz C, Kretschmer M, Steinmüller B and Thoma M H 2018 *Contrib. Plasma Phys.* **58** 21–29
[31] Mickel W, Kapfer S C, Schröder-Turk G E and Mecke K 2013 *J. Chem. Phys.* **138** 044501
[32] Steinhardt P J, Nelson D R and Ronchetti M 1983 *Phys. Rev. B* **28** 784–805
[33] Winczewski S, Dziedzic J and Rybicki J 2016 *Comput. Phys. Commun.* **198** 128–38
[34] Kapfer S C, Mickel W, Mecke K and Schröder-Turk G E 2012 *Phys. Rev. E* **85** 030301
[35] Geiger M and Smidt T 2022 e3nn: Euclidean neural networks *Preprint* (arXiv:2207.09453)
[36] Behler J 2011 The Journal of Chemical Physics **134** 074106 *Preprint* (available at: https://pubs.aip.org/aip/jcp/article-pdf/doi/10.1063/1.3553717/15435271/074106_1_online.pdf)
[37] Huo H and Rupp M 2022 *Mach. Learn.: Sci. Technol.* **3** 045017
[38] Laakso J, Himanen L, Homm H, Morooka E V, Jäger M O, Todorović M and Rinke P 2023 *J. Chem. Phys.* **158** 234802
[39] Mitic S, Klumov B A, Konopka U, Thoma M H and Morfill G E 2008 *Phys. Rev. Lett.* **101** 125002
[40] Hartmann P, Rosenberg M, Juhasz Z, Matthews L S, Sanford D L, Vermillion K, Carmona-Reyes J and Hyde T W 2020 *Plasma Sources Sci. Technol.* **29** 115014
[41] Mendoza A, Jiménez Martí D, Matthews L S, Rodríguez Saenz B, Hartmann P, Kostadinova E, Rosenberg M and Hyde T W 2025 *Phys. Plasmas* **32** 023705
[42] Mitic S *et al* 2021 *Phys. Rev. E* **103** 063212
[43] Air Zero G (collaboration partner for experimental investigations) 2025 Air zero g – parabolic flight provider (available at: www.airzerog.com/)
[44] Steinmüller B, Dietz C, Kretschmer M and Thoma M H 2017 Physics of Plasmas **24** 033705 *Preprint* (available at: https://pubs.aip.org/aip/pop/article-pdf/doi/10.1063/1.4977902/15942743/033705_1_online.pdf)
[45] Knapek C A, Couedel L, Dove A, Goree J, Konopka U, Melzer A, Ratynskaia S, Thoma M H and Thomas H M 2022 *Plasma Phys. Control. Fusion* **64** 124006
[46] Himpel M and Melzer A 2021 *Mach. Learn.: Sci. Technol.* **2** 045019
[47] Melzer A, Knapek C, Maier D, Mohr D and Schütt S 2025 *Phys. Rev. E* **111** 045214

Chapter 5

Conclusion and Outlook

This cumulative dissertation presents the systematic development of a data-driven analysis framework for the investigation of complex plasmas in the PK-4 experiment. The three underlying publications represent a coherent methodological advance, ranging from the precise detection of individual particles to the classification of ideal crystal structures and the robust analysis of anisotropic phases. Together, they establish an automated, objective, and physically consistent framework for the characterization of strongly coupled plasmas.
In the first part of this work, a U-Net based method for particle detection was developed that enables the reliable identification of microparticles even in highly noisy or overlapping image regions. By reconstructing the particle cloud along the scan axis, a volumetric representation was obtained that allows for precise determination of three dimensional positions and thus provides a robust basis for further structural analyses.
Building on this, in the second step a neural network for classifying local crystal structures from three dimensional particle positions was developed. For this purpose, the PointNet [53] model was used in the form of WignerNet, such that Wigner-Seitz cells are represented by $1,000$ uniformly distributed support points and analyzed directly as point clouds. The method proved to be highly robust to experimental noise and outperformed established structural descriptors such as the MCS algorithm [28]. This enabled a data-driven and experimentally validated classification of ideal local crystal phases in complex plasmas.
In the third step, this approach was extended to more complex anisotropic crystal phases. To this end, the PlasmaCrystalNet model was developed. It employs a symmetry-consistent SE(3)-inspired architecture, namely CEGANN [72], which preserves rotational and translational invariance. By combining local, invariant graph features with global Voronoi based descriptors that are invariant under rotations and translations, orthorhombic and tetragonal phases (*fco*, *bco*, *bct*) could be reliably distinguished. The architecture showed a high degree of robustness with respect to measurement noise, wake induced distortions, and structural anisotropy and achieved F1 scores above 0.9 even at $15\,\%$ positional uncertainty.

Together, this dissertation demonstrates that the integration of modern deep learning networks into experimental plasma physics enables largely automated, reliable, and physically consistent analysis of strongly coupled plasmas. The methods developed here provide new insights into the stability and dynamics of crystalline structures, the role of external parameters such as gas pressure, frequency, and electric field geometry, and the formation of anisotropic phases under microgravity conditions. Methodologically, this work represents a significant step toward ML models that do not simply respect physical symmetries and invariances but explicitly incorporate them into their internal representations.

The methods developed in this work open up a wide range of perspectives for future research in experimental and theoretical plasma physics. A particularly natural next step is to integrate the models presented here directly into the data processing pipelines of upcoming experiments. With efficient adjustments, the developed algorithms could be adapted to the hardware of the PK-4 successor experiment COMPACT [44] with only moderate modifications. In addition, the stereoscopic imaging system of the COMPACT setup [75, 76] enables substantially higher spatial resolution and therefore more precise structural analysis of three dimensional plasma structures. The new experimental platform thus offers the possibility of applying the methods developed here with significantly increased structural accuracy. Moreover, largely autonomous real time diagnostics become a realistic prospect. Such capabilities would make it possible to adaptively control ongoing experiments by continuously adjusting discharge parameters to the observed structural changes. This opens up new experimental strategies in which machine learning is used not only for post-processing but also for adaptive control of complex plasma systems.

Another promising approach for future research is the practical application of the methods developed here. The integration of all analysis tools and model components into a large language model (LLM) appears particularly promising. Such a combination would greatly simplify the operation of the algorithms and make interaction with complex analysis more intuitive. At the same time, an LLM could serve as an intelligent interface that automatically selects suitable models, suggests parameters, preprocesses data, or interprets results. A system like this would be especially valuable for use on board the ISS. An LLM-based assistance system could support astronauts in real time in the evaluation of experimental data without requiring detailed expertise in modeling or data analysis. This would significantly improve both the efficiency and reliability of the analyses. In the long term, such a system could contribute to the autonomous diagnosis, monitoring, and interpretation of complex plasma phenomena, thereby further optimizing the scientific use of limited resources in space.

Finally, it is important to highlight that the concepts developed here go far beyond plasma physics. The combination of geometric invariances, local graph based analysis, and global structural descriptors can be transferred to many other strongly coupled particle systems such as granular materials or atomic clusters. The precise characterization of local and global order also plays a central role in these systems, meaning that the methods presented in this work enable a wide range of future applications.
Overall, this dissertation therefore represents not only a completed methodological contribution, but also a conceptual framework for future developments. The combination of modern artificial intelligence and physical modeling opens up novel ways to understand and experimentally control complex many-particle systems and marks a substantial step toward autonomous and data-driven experimental methodologies in laboratory and microgravity environments.

Bibliography

[1] Mohr P J, Newell D B, Taylor B N and Tiesinga E 2025 *Rev. Mod. Phys.* **97**(2) 025002 DOI 10.1103/RevModPhys.97.025002

[2] Stroth U 2018 *Plasmaphysik: Phänomene, Grundlagen und Anwendungen* 2nd ed (Berlin, Heidelberg: Springer Berlin Heidelberg) ISBN 978-3-662-55236-0

[3] Shukla P K and Mamun A A 2002 *Plasma Physics and Controlled Fusion* **44** 395 DOI 10.1088/0741-3335/44/3/701

[4] Ichimaru S 1982 *Rev. Mod. Phys.* **54**(4) 1017–1059 DOI 10.1103/RevModPhys.54.1017

[5] Fortov V, Ivlev A, Khrapak S, Khrapak A and Morfill G 2005 *Physics Reports* **421** 1–103 ISSN 0370-1573 DOI 10.1016/j.physrep.2005.08.007

[6] Thomas H M and Morfill G E 1996 *Nature* **379** 806–809 DOI 10.1038/379806a0

[7] Ishihara O 2007 *Journal of Physics D: Applied Physics* **40** R121 DOI 10.1088/0022-3727/40/8/R01

[8] Nitter T and Havnes O 1992 *Earth, Moon, and Planets* **56** 7–34 DOI 10.1007/BF00054597

[9] Northrop T G 1992 *Physica Scripta* **45** 475 DOI 10.1088/0031-8949/45/5/011

[10] Goertz C K 1989 *Reviews of Geophysics* **27** 271–292 10.1029/RG027i002p00271

[11] Morfill G and Grün E 1979 *Planetary and Space Science* **27** 1283–1292 ISSN 0032-0633 DOI 10.1016/0032-0633(79)90106-5

[12] Rubin-Zuzic M, Morfill G E, Ivlev A V, Pompl R, Klumov B A, Bunk W, Thomas H M, Rothermel H, Havnes O and Fouquét A 2006 *Nature Physics* **2** 181–185 DOI 10.1038/nphys242

[13] Knapek C A, Ivlev A V, Klumov B A, Morfill G E and Samsonov D 2007 *Phys. Rev. Lett.* **98**(1) 015001 DOI 10.1103/PhysRevLett.98.015001

[14] Knapek C A, Samsonov D, Zhdanov S, Konopka U and Morfill G E 2007 *Phys. Rev. Lett.* **98**(1) 015004 DOI 10.1103/PhysRevLett.98.015004

[15] Nosenko V, Zhdanov S and Morfill G 2007 *Phys. Rev. Lett.* **99**(2) 025002 DOI 10.1103/PhysRevLett.99.025002

[16] Dietz C, Bergert R, Steinmüller B, Kretschmer M, Mitic S and Thoma M H 2018 *Phys. Rev. E* **97**(4) 043203 DOI 10.1103/PhysRevE.97.043203

[17] Klein M, Dormagen N, Thoma M H and Schwarz M 2026 *Machine Learning: Science and Technology* **7** 015032 DOI 10.1088/2632-2153/ae3cf9

[18] Wimmer L, Schmitz A S, Kretschmer M and Thoma M H 2024 *Physics of Plasmas* **31** 043702 ISSN 1070-664X DOI 10.1063/5.0190499

[19] Wimmer L, Beppler S, Dormagen N, Klein M, Kretschmer M, Lipaev A M, Schwarz M, Usachev A D, Petrov O F, Zeller T A, Zobnin A V and Thoma M H 2025 *New Journal of Physics* **27** 114301 DOI 10.1088/1367-2630/ae140b

[20] Thomas H, Morfill G E, Demmel V, Goree J, Feuerbacher B and Möhlmann D 1994 *Phys. Rev. Lett.* **73**(5) 652–655 DOI 10.1103/PhysRevLett.73.652

[21] Pustylnik M Y, Fink M A, Nosenko V, Antonova T, Hagl T, Thomas H M, Zobnin A V, Lipaev A M, Usachev A D, Molotkov V I, Petrov O F, Fortov V E, Rau C, Deysenroth C, Albrecht S, Kretschmer M, Thoma M H, Morfill G E, Seurig R, Stettner A, Alyamovskaya V A, Orr A, Kufner E, Lavrenko E G, Padalka G I, Serova E O, Samokutyayev A M and Christoforetti S 2016 *Review of Scientific Instruments* **87** 093505 ISSN 0034-6748 DOI 10.1063/1.4962696

[22] Nefedov A P, Morfill G E, Fortov V E, Thomas H M, Rothermel H, Hagl T, Ivlev A V, Zuzic M, Klumov B A, Lipaev A M, Molotkov V I, Petrov O F, Gidzenko Y P, Krikalev S K, Shepherd W, Ivanov A I, Roth M, Binnenbruck H, Goree J A and Semenov Y P 2003 *New Journal of Physics* **5** 33 DOI 10.1088/1367-2630/5/1/333

[23] Thomas H M, Morfill G E, Fortov V E, Ivlev A V, Molotkov V I, Lipaev A M, Hagl T, Rothermel H, Khrapak S A, Suetterlin R K, Rubin-Zuzic M, Petrov O F, Tokarev V I and Krikalev S K 2008 *New Journal of Physics* **10** 033036 DOI 10.1088/1367-2630/10/3/033036

[24] Cottrino S, Gaudisson T, Douillard T, Blanchard N, Meille S, Gremillard L, Mercury M and Le Floch S 2025 *Journal of the European Ceramic Society* **45** 117579 ISSN 0955-2219 DOI 10.1016/j.jeurceramsoc.2025.117579

[25] Nagata M, Horikawa N, Kawabata M and Ameyama K 2019 *MATERIALS TRANSACTIONS* **60** 1914–1920 DOI 10.2320/matertrans.MT-M2019145

[26] Klindworth M, Arp O and Piel A 2006 *Journal of Physics D: Applied Physics* **39** 1095 DOI 10.1088/0022-3727/39/6/015

[27] Melzer A 2019 *Physics of Dusty Plasmas: An Introduction* (*Lecture Notes in Physics* vol 962) (Springer Cham) ISBN 978-3-030-20259-0 DOI 10.1007/978-3-030-20260-6

[28] Dietz C, Kretz T and Thoma M H 2017 *Phys. Rev. E* **96**(1) 011301 DOI 10.1103/PhysRevE.96.011301

[29] Ivlev A V, Bartnick J, Heinen M, Du C R, Nosenko V and Löwen H 2015 *Phys. Rev. X* **5**(1) 011035 DOI 10.1103/PhysRevX.5.011035

[30] Ivlev A V, Morfill G E, Thomas H M, Räth C, Joyce G, Huber P, Kompaneets R, Fortov V E, Lipaev A M, Molotkov V I, Reiter T, Turin M and Vinogradov P 2008 *Phys. Rev. Lett.* **100**(9) 095003 DOI 10.1103/PhysRevLett.100.095003

[31] Ivlev A V, Thoma M H, Räth C, Joyce G and Morfill G E 2011 *Phys. Rev. Lett.* **106**(15) 155001 DOI 10.1103/PhysRevLett.106.155001

[32] Takahashi K and Totsuji H 2019 *IEEE Transactions on Plasma Science* **47** 4213–4218 DOI 10.1109/TPS.2019.2924260

[33] Yasuaki Hayashi Y H and Kunihide Tachibana K T 1994 *Japanese Journal of Applied Physics* **33** L804 DOI 10.1143/JJAP.33.L804

[34] Zuzic M, Ivlev A V, Goree J, Morfill G E, Thomas H M, Rothermel H, Konopka U, Sütterlin R and Goldbeck D D 2000 *Phys. Rev. Lett.* **85**(19) 4064–4067 DOI 10.1103/PhysRevLett.85.4064

[35] Steinhardt P J, Nelson D R and Ronchetti M 1983 *Physical Review B* **28** 784–805 ISSN 0163-1829 DOI 10.1103/PhysRevB.28.784

[36] Melzer A, Schella A, Miksch T, Schablinkski J, Block D, Piel A, Thomsen H, Kählert H and Bonitz M 2012 *Contributions to Plasma Physics* **52** 795–803 DOI 10.1002/ctpp.201200028

[37] Honeycutt J D and Andersen H C 1987 *The Journal of Physical Chemistry* **91** 4950–4963 DOI 10.1021/j100303a014

[38] Mickel W, Kapfer S C, Schröder-Turk G E and Mecke K 2013 *The Journal of chemical physics* **138** 044501 DOI 10.1063/1.4774084

[39] Deutsches Zentrum für Luft- und Raumfahrt (DLR) Fallturm Bremen – Forschungsplattform für Schwerelosigkeit `https://www.dlr.de/de/ar/themen-missionen/weltraumforschung/forschung-unter-weltraumbedingungen/forschungsplattformen/fallturm-bremen` zugriff am 27. November 2025

[40] Air Zero G 2025 Nocespace– parabolic flight provider and collaboration partner for experimental investigations https://www.airzerog.com/

[41] Siegl M, Kargl F, Scheuerpflug F, Drescher J, Neumann C, Balter M, Kolbe M, Sperl M, Yu P and Meyer A 2013 *MORABA / DLR* Online available: `https://moraba.de/wp-content/uploads/2020/11/MAPHEUS_Siegl.pdf`

[42] Deutsches Zentrum für Luft- und Raumfahrt (DLR) 2024 42. dlr-parabelflug `https://www.dlr.de/de/ar/themen-missionen/weltraumforschung/forschung-unter-weltraumbedingungen/forschungsplattformen/parabelflug/parabelflug-42` zugriff am 25. November 2025

[43] Deutsches Zentrum für Luft- und Raumfahrt (DLR) 2025 44. dlr-parabelflug `https://www.dlr.de/de/ar/themen-missionen/weltraumforschung/forschung-unter-weltraumbedingungen/forschungsplattformen/parabelflug/parabelflug-44` zugriff am 25. November 2025

[44] Knapek C A, Couedel L, Dove A, Goree J, Konopka U, Melzer A, Ratynskaia S, Thoma M H and Thomas H M 2022 *Plasma Physics and Controlled Fusion* **64** 124006 DOI 10.1088/1361-6587/ac9ff0

[45] Cortes C and Vapnik V 1995 *Machine Learning* **20** 273–297 DOI 10.1007/BF00994018

[46] Frochte J 2020 *Maschinelles Lernen: Grundlagen und Algorithmen in Python* 3rd ed (München: Carl Hanser Verlag) ISBN 978-3-446-46144-4

[47] Mehta P, Bukov M, Wang C H, Day A G, Richardson C, Fisher C K and Schwab D J 2019 *Physics Reports* **810** 1–124 ISSN 0370-1573 DOI 10.1016/j.physrep.2019.03.001

[48] Tang Y, Kurths J, Lin W, Ott E and Kocarev L 2020 *Chaos: An Interdisciplinary Journal of Nonlinear Science* **30** 063151 DOI 10.1063/5.0016505

[49] Carleo G, Cirac I, Cranmer K, Daudet L, Schuld M, Tishby N, Vogt-Maranto L and Zdeborová L 2019 *Rev. Mod. Phys.* **91**(4) 045002 DOI 10.1103/RevModPhys.91.045002

[50] Glorot X, Bordes A and Bengio Y 2011 Deep sparse rectifier neural networks *Proceedings of the Fourteenth International Conference on Artificial Intelligence and Statistics* vol 15 (PMLR) pp 315–323 https://proceedings.mlr.press/v15/glorot11a.html

[51] Bridle J S 1990 Probabilistic interpretation of feedforward classification network outputs, with relationships to statistical pattern recognition *Neurocomputing* ed Soulié F F and Hérault J (Springer Berlin Heidelberg) pp 227–236 DOI 10.1007/978-3-642-76153-9 28

[52] Murtagh F 1991 *Neurocomputing* **2** 183–197 DOI 10.1016/0925-2312(91)90023-5

[53] Qi C R, Su H, Mo K and Guibas L J 2017 Pointnet: Deep learning on point sets for 3d classification and segmentation DOI 10.48550/arXiv.1612.00593

[54] Bronstein M M, Bruna J, Cohen T and Veličković P 2021 Geometric deep learning: Grids, groups, graphs, geodesics, and gauges DOI 10.48550/arXiv.2104.13478

[55] Rumelhart D E, Hinton G E and Williams R J 1986 *Nature* **323** 533–536 DOI 10.1038/323533a0

[56] Cybenko G 1989 *Mathematics of Control, Signals and Systems* **2** 303–314 DOI 10.1007/BF02551274

[57] Hornik K, Stinchcombe M and White H 1989 *Neural Networks* **2** 359–366 ISSN 0893-6080 DOI 10.1016/0893-6080(89)90020-8

[58] Zhao X, Wang L, Zhang Y, Han X, Deveci M and Parmar M 2024 *Artificial Intelligence Review* **57** 99 ISSN 1573-7462 DOI 10.1007/s10462-024-10721-6

[59] Zeiler M D and Fergus R 2013 Visualizing and understanding convolutional networks DOI 10.48550/arXiv.1311.2901

[60] Ronneberger O, Fischer P and Brox T 2015 U-net: Convolutional networks for biomedical image segmentation https://arxiv.org/pdf/1505.04597v1

[61] Dormagen N, Klein M, Schmitz A S, Thoma M H and Schwarz M 2024 *Journal of Imaging* **10** ISSN 2313-433X DOI 10.3390/jimaging10020040

[62] Allan D, Caswell T, Keim N and van der Wel C 2016 trackpy: Trackpy v0.3.2 DOI 10.5281/zenodo.60550

[63] Klein M, Dormagen N, Dietz C, Thoma M and Schwarz M 2024 *Machine Learning: Science and Technology* DOI 10.1088/2632-2153/ad4d3e

[64] Klein M, Dormagen N, Schmitz A S, Thoma M H and Schwarz M 2023 Machine learning approach for particle matching, tracing and velocimetry with self-organizing map: Application to complex plasmas *2023 International Conference on Machine Learning and Applications (ICMLA)* (IEEE) pp 839–844 ISBN 979-8-3503-4534-6 DOI 10.1109/ICMLA58977.2023.00123

[65] Klein M, Dormagen N, Wimmer L, Thoma M H and Schwarz M 2025 *Machine Learning and Knowledge Extraction* **7** ISSN 2504-4990 DOI 10.3390/make7020037

[66] Dormagen N, Klein M, Schmitz A S, Wimmer L, Thoma M H and Schwarz M 2024 *Machine Learning: Science and Technology* **5** 045006 DOI 10.1088/2632-2153/ad8062

[67] Fuchs F B, Worrall D E, Fischer V and Welling M 2020 Se(3)-transformers: 3d roto-translation equivariant attention networks https://arxiv.org/abs/2006.10503

[68] Geiger M and Smidt T 2022 e3nn: Euclidean neural networks https://arxiv.org/abs/2207.09453

[69] Batzner S, Musaelian A, Sun L, Geiger M, Mailoa J P, Kornbluth M, Molinari N, Smidt T E and Kozinsky B 2022 *Nature Communications* **13** 2453 DOI 10.1038/s41467-022-29939-5

[70] Thomas N, Smidt T, Kearnes S, Yang L, Li L, Kohlhoff K and Riley P 2018 Tensor field networks: Rotation- and translation-equivariant neural networks for 3d point clouds https://arxiv.org/abs/1802.08219

[71] Dormagen N, Klein M, Schmitz A S, Wimmer L, Thoma M H and Schwarz M 2025 *Machine Learning: Science and Technology* **6** 045016 DOI 10.1088/2632-2153/ae13d0

[72] Banik S, Dhabal D, Chan H, Manna S, Cherukara M, Molinero V and Sankaranarayanan S K R S 2023 *npj Computational Materials* **9** 23 DOI 10.1038/s41524-023-00975-z

[73] Winczewski S, Dziedzic J and Rybicki J 2016 *Computer Physics Communications* **198** 128–138 ISSN 0010-4655 DOI 10.1016/j.cpc.2015.09.009

[74] Kapfer S C, Mickel W, Mecke K and Schröder-Turk G E 2012 *Phys. Rev. E* **85**(3) 030301 DOI 10.1103/PhysRevE.85.030301

[75] Himpel M and Melzer A 2021 *Machine Learning: Science and Technology* **2** 045019 DOI 10.1088/2632-2153/ac1fc8

[76] Melzer A, Knapek C, Maier D, Mohr D and Schütt S 2025 *Phys. Rev. E* **111**(4) 045214 DOI 10.1103/PhysRevE.111.045214

Publications During the Ph.D.

This section enumerates all scientific publications resulting from research conducted during the Ph.D. period. The list includes both first-author and co-authored works, presented in chronological order.

1. Dormagen N, Klein M, Schmitz A S, Thoma M H and Schwarz M *Machine Learning Approach for Multi Particle Tracking in Complex Plasmas*. Conference: 2023 30th International Conference on Mixed Design of Integrated Circuits and System (MIXDES) DOI: 10.23919/MIXDES58562.2023.10203212

2. Klein M, Dormagen N, Schmitz A S, Thoma M and Schwarz M *Machine Learning Approach for Particle Matching, Tracing and Velocimetry with Self-Organizing Map: Application to Complex Plasmas*. Conference: 2023 International Conference on Machine Learning and Applications (ICMLA) DOI: 10.1109/ICMLA58977.2023.00123

3. Dormagen N, Klein M, Schmitz A S, Thoma M H and Schwarz M *Multi-Particle Tracking in Complex Plasmas Using a Simplified and Compact U-Net*. January 2024 Journal of Imaging (J. Imaging) 10(2):40 DOI: 10.3390/jimaging10020040

4. Klein M, Dormagen N, Dietz C, Thoma M and Schwarz M *Enhancing particle string detection in electrorheological plasmas using asymmetrical kernel convolutional networks*. Machine Learning: Science and Technology 5(2), 025050, 2024 DOI:10.1088/2632-2153/ad4d3e

5. Schwarz, M., Dormagen, N., Klein, M., Pappert, S., Schmitz, A. S., Thoma, M. H. *AI Algorithms for Plasma Particle Tracking*. Conference: 2024 31st International Conference on Mixed Design of Integrated Circuits and System (MIXDES) DOI: 10.23919/MIXDES62605.2024.10614053

6. Dormagen N, Klein M, Schmitz A S, Wimmer L, Thoma M H and Schwarz M *Local classification of crystalline structures in complex plasmas using a PointNet*. Machine Learning: Science and Technology, 5(4), 045006, 2024. DOI:10.1088/2632-2153/ad8062

7. Wimmer, L., Dormagen, N., Klein, M., Kretschmer, M., Lipaev, A. M., Schwarz, M., Usachev, A. D., Petrov, O. F., Zobnin, A. V., Thoma, M. H. *Impact of particle charge and electrorheology-effects on dust-acoustic waves in low pressure complex plasma under microgravity*. New Journal of Physics, 27(3), 033001, 2025. DOI: 10.1088/1367-2630/adb876

8. Klein, M., Dormagen, N., Wimmer, L., Thoma, M. H., Schwarz, M. *Advancing Particle Tracking: Self-Organizing Map Hyperparameter Study and Long Short-Term Memory-Based Outlier Detection*. Machine Learning and Knowledge Extraction, 7(2), Article 37, 2025. DOI: 10.3390/make7020037

9. Dormagen, N., Klein, M., Schmitz, A. S., Wimmer, L., Thoma, M. H., Schwarz, M. *Time-resolved classification of plasma crystals in a direct current discharge using an advanced graph neural network*. Machine Learning: Science and Technology 6(4), 045016, 2025. DOI:10.1088/2632-2153/ae13d0

10. Wimmer L, Beppler S, Dormagen N, Klein M, Kretschmer M, Lipaev A M, Schwarz M, Usachev A D, Petrov O F, Zeller T A, Zobnin A V and Thoma M H *Investigation of charge and ion drag force dynamics in complex plasma experiments with neon and argon under microgravity*. New Journal of Physics, 27(11), 114301, 2025. DOI: 10.1088/1367-2630/ae140b

11. Klein, M., Dormagen, N., Thoma, M. H., Schwarz, M. *Particle-resolved turbulence detection in complex plasmas using LSTM neural network*. Machine Learning: Science and Technology 7(1), 015032, 2026. DOI: 10.1088/2632-2153/ae3cf9

Declaration of Authorship

I declare that I have completed this dissertation single-handedly without the unauthorized help of a second party and only with the assistance acknowledged therein. I have appropriately acknowledged and cited all text passages that are derived verbatim from or are based on the content of published work of others, and all information relating to verbal communications. I consent to the use of an anti-plagiarism software to check my thesis. I have abided by the principles of good scientific conduct laid down in the charter of the Justus Liebig University Giessen „Satzung der Justus-Liebig-Universität Gießen zur Sicherung guter wissenschaftlicher Praxis“ in carrying out the investigations described in the dissertation.

Information on the use of artificial intelligence (AI)-based tools such as ChatGPT or SchulKI by OpenAI or Gemini by Google in the preparation of this dissertation (please tick as appropriate):

- ☐ I did not use any AI tool in the preparation of this text.
- ☑ I used an AI tool in the following areas (multiple selections possible):
  - ☐ Generating ideas and stimulating creativity
  - ☐ Understanding concepts, researching facts and definitions
  - ☑ Optimising text written by myself
  - ☐ Generating entire text passages based on my instructions

The following AI tools were used, and the respective parts of my text benefited from them as follows:

- DeepL was used for translation and linguistic revision of self-written text passages
- The Overleaf AI Assist tool was used to improve phrasing and stylistic clarity of self-authored content

Date: _____ Signature: _____

Acknowledgements

First and foremost, I would like to express my sincere gratitude to my supervisors, Prof. Dr. Markus H. Thoma and Prof. Dr. Mike Schwarz, for their continuous support, trust, and the many opportunities for scientific exchange. They provided me with the freedom and time necessary to fully concentrate on my research, and their expertise in physics and artificial intelligence was invaluable throughout both the research and writing phases of this thesis. Their guidance formed the foundation on which this work was made possible.
I also gratefully acknowledge the German Aerospace Center (DLR) for funding this work under Grant No. 50WK2270B. The provision of computational resources, including workstations and NVIDIA Jetson boards, was essential for the successful completion of this project. I would like to thank Marco Künkeler in particular for his support in setting up and commissioning the hardware systems used in this work.
Furthermore, I would like to thank Lukas Wimmer, Andreas Schmitz, Thomas Nimmerfroh, and Dr. Michael Kretschmer for their support during the experimental work and the parabolic flight campaigns.
A very special thank you goes to my colleague and close friend Max Klein. He supported this work not only through numerous scientific discussions and idea development, but also through his substantial contributions to the planning and execution of the parabolic flight campaigns. On a personal level, his companionship made this phase of my academic career particularly memorable. Without his involvement, the outcome of this work would certainly not have been as successful nor as meaningful.
I would also like to express my sincere gratitude to my family, whose continuous support throughout my entire academic journey made this work possible in the first place. Their encouragement and trust provided the foundation for my educational and scientific development.
Finally, I would like to thank my partner Tamara, who was my most important personal companion throughout my entire doctoral journey. Her unwavering support, understanding, and encouragement were invaluable and contributed greatly to the successful completion of this work.